

AD-A280 368



AEGSR-TR 94 0352

Approved for public release;
distribution unlimited.

**INTERACTION EFFECTS OF CRACKS, FLAWS AND
DAMAGE IN CERAMIC**

(1)

Howard L. Schreyer
Ming L. Wang

Departments of Mechanical and Civil Engineering
The University of New Mexico
Albuquerque, New Mexico 87131

May 4, 1994

Final Report

DTIC
ELECTE
JUN 15 1994
S F D

Prepared For:

Air Force Office of Scientific Research
Bolling Air Force Base, DC 20332-6448

College of Engineering
The University of New Mexico
Albuquerque, NM 87131

1026
256050 94-18482



94 6 14 146

UNCLASSIFIED

SECURITY CLASSIFICATION OF THIS PAGE

REPORT DOCUMENTATION PAGE

1a. REPORT SECURITY CLASSIFICATION unclassified	1b. RESTRICTIVE MARKINGS		
2a. SECURITY CLASSIFICATION AUTHORITY	3. DISTRIBUTION/AVAILABILITY OF REPORT Approved for public release; unlimited distribution unlimited.		
2b. DECLASSIFICATION/DOWNGRADING SCHEDULE			
4. PERFORMING ORGANIZATION REPORT NUMBER(S)	5. MONITORING ORGANIZATION REPORT NUMBER(S) AFOSR-94 0352 AFOSR-91-0419		
6a. NAME OF PERFORMING ORGANIZATION College of Engineering University of New Mexico	6b. OFFICE SYMBOL (if applicable)	7a. NAME OF MONITORING ORGANIZATION AFOSR Dr. Walter F. Jones	
6c. ADDRESS (City, State and ZIP Code) Dept. of Civil Engineering The University of New Mexico Albuquerque, NM 87131	7b. ADDRESS (City, State and ZIP Code) AFOSR/NA Building 410 Bolling AFB, D.C. 20332-6448		
8a. NAME OF FUNDING/SPONSORING ORGANIZATION AFOSR	8b. OFFICE SYMBOL (if applicable) NA	9. PROCUREMENT INSTRUMENT IDENTIFICATION NUMBER AFOSR-91-0419	
9c. ADDRESS (City, State and ZIP Code) AFOSR/NA Building 410 Bolling AFB, D.C. 20332-6448	10. SOURCE OF FUNDING NOS. 61102F 2302 25		
11. TITLE (Include Security Classification) Interaction Effects of Cracks, Flaws and Damage in Ceramic	11. PROGRAM ELEMENT NO. 12. PROJECT NO. 13. TASK NO. 14. WORK UNIT NO.		
12. PERSONAL AUTHOR(S) Howard L. Schreyer and Ming L. Wang			
13a. TYPE OF REPORT FINAL	13b. TIME COVERED FROM 09/92 TO 03/94	14. DATE OF REPORT (Yr., Mo., Day) May 4, 1994	15. PAGE COUNT 100
16. SUPPLEMENTARY NOTATION			

17. COSATI CODES	18. SUBJECT TERMS (Continue on reverse if necessary and identify by block number) GRAIN BOUNDARIES, MICROSTRUCTURES		
FIELD	GROUP	SUB. GR.	

19. ABSTRACT (Continue on reverse if necessary and identify by block number)

It is generally recognized that the nature of grain boundaries and microstructures affects the properties and behavior of ceramics. One of the objectives of this research is to study the fracture process of the ceramic in real time and to measure the strain field in the vicinity of the crack including the bridging zones. A fast-scanning electron microscope (FSEM) for dynamic microscopy applications was used to capture the fracture events in the ceramic. This equipment captures images at high speed. The SEM chamber was also modified to accomodate an in-situ tension-compression loading device to fracture ceramics. The fracture mode was predominantly intergranular. No indication of a microcrack-cloud zone was observed in the FSEM results. Grain bridging was observed along the entire crack interface and over the entire propagation distance. (continued on back)

20. DISTRIBUTION/AVAILABILITY OF ABSTRACT UNCLASSIFIED/UNLIMITED <input checked="" type="checkbox"/> SAME AS RPT. <input type="checkbox"/> DTIC USERS <input type="checkbox"/>	21. ABSTRACT SECURITY CLASSIFICATION Unclassified		
22a. NAME OF RESPONSIBLE INDIVIDUAL Dr. WALTER JONES	22b. TELEPHONE NUMBER (including area code) 202 767-0471	22c. OFFICE SYMBOL AFOSR/NA	

19. (cont'd)

A detailed understanding of ceramics requires constitutive models for grains and grain boundaries and a method for predicting the response of ceramic specimens to experimental loads. Voronoi diagrams are used to construct realistic grain topologies, and continuum damage relations are used to represent the behavior of grain boundaries. A robust solution algorithm is used to obtain solutions that include softening or failure. These results show the evolution of microcracks, crack branching, crack bridging, and the ultimate development of microcracks. Although the computational domain only contains a small number of grains, the results indicate that such simulations are feasible and that extension of the analysis to three dimensions is a logical step.

Accesion For	
NTIS CRA&I	<input checked="" type="checkbox"/>
DTIC TAB	<input type="checkbox"/>
Unannounced	<input type="checkbox"/>
Justification	<input type="checkbox"/>
By _____	
Distribution /	
Availability Copies	
Dist	Avail and/or Special
A-1	

**Final Report
on
Interaction Effects of Cracks, Flaws and Damage in Ceramic**

by
Howard L. Schreyer
Department of Mechanical Engineering
and
Ming L. Wang
Department of Civil Engineering
The University of New Mexico

May, 4, 1994

TABLE OF CONTENTS	-----	Page 1
1. INTRODUCTION	-----	Page 2
2. RESEARCH OBJECTIVE	-----	Page 2
3. SUMMARY OF RESEARCH	-----	Page 4
3.1 Experimental		
3.2 Theoretical		
4. DETAILS OF RESEARCH	-----	Page 5
4.1 Ceramic Properties (alumina)		
4.2 Microstructural Study		
4.3 Real Time Fracture Study of Ceramics		
4.4 Numerical Simulation of Microfracture		
4.5 Summary and Conclusions		
5. PROPOSED EXTENSION	-----	Page 19
6. REFERENCES	-----	Page 21
7. LIST OF FIGURES	-----	Page 24
APPENDIX 1. The processing and properties of alumina	-----	Page 63
APPENDIX 2. Dynamic relaxation	-----	Page 64
APPENDIX 3. Tension-compression loading stage	-----	Page 68
APPENDIX 4. Fast-Scanning Electron Microscope capabilities	-----	Page 77
APPENDIX 5. Direct Application of Constraints to Symmetric Algebraic Systems	-----	Page 82

1. INTRODUCTION

For quasi-brittle materials a significant amount of research has been conducted under the assumption that a process zone develops ahead of a crack tip. Here, a crack process zone is defined to be a zone of distributed microcracks developing prior to a macrocrack in a region both above and below the plane of the macrocrack. The very existence of such a zone has been the subject of major inquiry [Mindess, 1990]. Experimental evidence [Wang, Schreyer and Rutland, 1990; van Mier, 1990] indicates that such a zone is extremely hard to identify or is nonexistent. A theoretical investigation [Horii and Nirmalendran, 1990] shows that even if a zone of microcracks develops prior to the formation of a macrocrack, the influence of the zone is a relatively insignificant part of the response of the structure. Load-deflection curves obtained in the laboratory and post-limit sectioning of samples indicate that there is a significant amount of activity prior to the formation of a macrocrack but not in the form of a crack process zone. Instead, microcracks open prior to the macrocrack with the result that certain elements such as inclusions in ceramics maintain contact longer than the surrounding matrix. This is called the crack bridging effect or "wake" effect which is interpreted as shielding the crack tip from applied stress [Reichl and Steinbrech, 1988]. Furthermore, aggregates or inclusions cause the resulting crack surface to be strongly nonplanar or "tortuous," also called crack deflection [Faber and Evans, 1983]. The development of crack bridging [Kobayashi and Shochey, 1987; Li, 1990], tortuosity and a nonlinear crack front formed by the presence of inclusions causes a specimen to appear less brittle than an identical geometrical specimen composed of the parent matrix material. Such materials are called quasi-brittle because classical linear elastic fracture mechanics cannot be applied without modifications to account for the apparent ductility which is developed prior to failure.

The most straightforward experimental examples involve Mode I cracks as developed, for example, in tension or three-point and four-point bending tests. In addition to the apparent ductility displayed prior to the peak load, a softening branch is exhibited in the post-peak regime of the load-deflection curve if the specimen is small enough. This softening is another manifestation of apparent ductility. Under certain combinations of material and geometrical properties, cracks will propagate in a continuous but slow rate under displacement control [Maji et al., 1990]. This suggests that the crack driving "force" is just sufficient to overcome the crack "resistance" and that the process is not necessarily unstable as is commonly claimed. Suppose that cracks may grow at a rate governed by an inherent material property and the crack driving force. Then if a specimen is loaded dynamically, the average stress could significantly exceed the static stress necessary to cause failure, and any number of pre-existing flaws could serve to initiate cracks. However, most dynamic loads are impulsive in nature so the growth of these cracks is soon arrested because of the lack of a driving force. The result is the potential existence of a region of microcracks. Therefore, for dynamic situations, the evolution of a macrocrack must be understood when considering a microcrack process zone. For quasi-static processes, which are the subject of this research, there is little experimental evidence that displays a crack process zone in the form of a region of distributed microcracks prior to the macrocrack. The subject is one of considerable controversy.

2. RESEARCH OBJECTIVE

Existing experimental results indicate that crack branching occurs, and existing cracks sustain a significant amount of load carrying capacity. This feature has been

demonstrated in an alumina ceramic: "Active grain bridges were observed along the entire crack trace and over the entire propagation distance. No indication of a microcrack-cloud zone was observed, ... "[Rodel, 1990]. To capture the feature of support along the entire crack trace, the damage crack concept is proposed in this research in which the traction on the crack face is related to the discontinuity in displacement through a crack modulus. Damage, and hence the modulus, also vary with the discontinuity in displacement across the crack. The model used in this project yielded a problem somewhat analogous to a spring foundation but with a nonlinear spring. From conventional damage concepts, the stiffness coefficients were related to the amount of ligament area still intact in comparison to the total area of the crack. As the crack evolved, the stiffness of the complete specimen was correlated with the degree of damage in the crack. There was no assumption that distributed microcracks exist with this approach. The predictions of stiffness for the specimen, or a part of the specimen, and the strength of the specimen were correlated with experimental data in the literature to provide an initial indication of the magnitude of the crack stiffness.

Numerical solutions were obtained for the case of a compact tension specimen. The interface was modeled as a damage crack with a small amount of initial damage. The change in response of the specimen due to the crack propagation provided an indirect measure of the original strength of the bond. Problems involving softening and localization are notoriously difficult to solve because the tangent stiffness matrix becomes singular at the peak load, and multiple solution paths exist for displacement beyond those at peak load. Existing numerical algorithms were attempted, but even the simplest situation of a two-dimensional mode for uniaxial tension required an inordinate amount of computer time. One of the more important achievements of this research was the development of a robust and efficient algorithm for solving problems involving softening and localization.

The issue of crack branching was addressed by introducing inclusions to cause multiple interruptions. The reason why a microcrack ceases to grow in preference to an alternative path was addressed numerically by investigating alternative arrangements of inclusions. Specifically, angular shape inclusions were considered and an attempt was made to show how inclusions can rotate to cause bridging by interrupting the crack paths.

The following are objectives of the numerical phase of this study:

1. By an indirect process of comparing experimental data on tensile failure with predictions based on a spectrum of grain boundary material parameters, we will be able to determine the mechanical properties of the grain boundary itself.
2. We will be able to show how crack branching occurs. These results will be important for constructing nonlocal continuum models for representing the ceramic.
3. We will be able to demonstrate that a microstructural analysis can be performed so that the effects of additional features such as porosity and anisotropy can be incorporated.
4. The basis will be established for looking at toughening mechanisms provided by fibers and particles in a systematic manner rather than by empirical methods currently in use [Pezzotti et al. 1990a, 1990b].
5. The ultimate advantage of the numerical approach will be the capability for identifying quantitatively those individual features that will have the greatest potential for enhancing strength and ductility.

It would be useful for analysis if a ceramic could be modeled as a continuum, process zone mechanism varying from one ceramic to the other, as exhibited, for example, by toughening in which fracture resistance systematically increases with crack extension. Such features appear if mechanisms such as phase transformations, grain bridging and whisker reinforcements are present [Evans, 1990]. These features can be captured in a

continuum model only if softening and nonlocal aspects are included. The nonlocal part of a constitutive equation controls the size of the predicted process zone and maintains the mathematical well-posedness of the governing equilibrium equation, i.e., the original elliptic nature of the equation remains elliptic as a crack process zone is established.

The compact-tension tests of alumina ceramic were performed on large specimens using the Instron Testing Machine, and on a much smaller scale inside the chamber of a Scanning Electron Microscope (SEM). The small in-situ tests involving the SEM provided the phenomenon of microfracturing both for scientific understanding and for practical application. In this case, the special loading stage, which can be mounted in the SEM chamber, was designed, including the closed-loop feedback to the loading device.

In summary, the objectives of the experimental phase were:

- (i) to determine the mechanics of bridging
- (ii) to provide a real-time description of macrocrack interaction with microcracks
- (iii) to provide those measurements useful for verifying the theoretical approach such as cracking-opening displacements, loads, displacements at the point of application of the load, crack lengths and locations of cracks
- (iv) to continue the development of the in-situ testing device to include a displacement closed-loop control feature.

3. SUMMARY OF RESEARCH

3.1 Experimental

It is generally recognized that the nature of grain boundaries and microstructures affects the properties and behavior of ceramics. It is important to understand the ceramic processing characteristics which affect the nature of grain boundaries. Different processing techniques have been attempted to produce the desired microstructure of alumina in the laboratory (See progress report, Nov. 1, 1992). Because the size of a ceramic sample cannot be augmented to perform mechanical tests, and because the ceramic is not fully dense, an alumina bar measuring 30 mm X 30 mm X 250 mm was obtained from the Coors Technical Ceramics Co. The relative density of the alumina is 99.5%. (see Appendix 1 for the processing and properties of alumina).

Ceramic compact tension tests were conducted on an Instron. Since the stiffness difference between the load frame of Instron and the compact tension specimen is large, A reasonable load-deflection curve could not be obtained. The Scanning Electron Microscope (SEM) is widely used as an analytical tool in the field of failure and fracture analysis, primarily because of its combination of good field depth and high resolution. For the studying of the microfracture process of the ceramic, the closed-loop control in-situ loading stage, which can be mounted inside the SEM chamber, was designed to perform a real time fracture test.

Compared with most metallic materials, the mechanical properties of engineering ceramics are much more sensitive to factors such as size, shape and surface finish. When tests are conducted, machining of some of the surface is required to remove surface flaws. Ceramic materials are difficult and expensive to machine due to their high hardness and brittle nature. The tool must have a higher hardness than the ceramic being machined, and must be of a configuration that removes surface stock without overstressing the component. For these reasons, several special machines were purchased to prepare the specimen.

Examination of fracture surfaces with SEM can provide useful information on such aspects as local fracture mechanisms and fracture propagation direction. After the test, the fracture surface is examined by the SEM. Since ceramic samples lack sufficient conductivity for analysis in SEM, to produce a conductive layer, carbon, gold, or aluminum is evaporated onto the specimen surface. Fractographies show the fracture of alumina is intergranular. Intergranular fracture is usually the most easily recognizable mode of fracture, but determining the cause may be quite difficult.

3.2 Theoretical

Inclusions in ceramics provide a toughening effect by rotating and impeding crack openings through what is called "crack bridging." A major objective of this research is to investigate in detail the mechanisms that occur in crack bridging; however, a study of micrographs available in the literature indicate that the same phenomenon appears with grains, only at a smaller scale. In particular, crack branching occurs around grains with one of these microcracks, ultimately evolving to a macrocrack, with large grains appearing as "inclusions" which rotate as rigid bodies. Based on this observation, the theoretical phase involved an investigation of fundamental properties of grain boundaries. Such an analysis can be closely guided by in-situ testing in a scanning electron microscope (SEM), and theoretical results can provide insight into how the mechanical properties of ceramics can be improved.

Continuous damage mechanics is concerned only with the description of progressive weakening of solids due to the development of microcracks and microvoids; therefore, continuum damage mechanics is the most appropriate approach for analyzing the nonlinear behavior of quasi-brittle materials. Based on microstructural analysis, it was proposed to numerically model in two dimensions a small region composed of a set of grains and grain boundaries, as shown in Fig. 1. Each grain was modeled as an elastic material while the grain boundary was considered to be a thin region of elastic damaging material. An initial assumption was that each grain is scalar isotropic but at a later stage, a two-parameter isotropic model was introduced.

In our finite element codes, dynamic relaxation (DR), an explicit incremental iterative method, was used to obtain preliminary numerical results. The DR method is based on the fact that the static solution is the steady state part of the transient response for a temporal-step load [Underwood, 1983]. This method is especially attractive for problems with highly nonlinear geometric and material behaviors, which include limit points and regions of very soft stiffness characteristics, like the issue in our research. Crack nucleation and propagation along the grain boundary are shown in the numerical results. The effects of microcracks, voids and inclusions are also observed.

Numerical investigations are difficult because of the ill-conditioning inherent in the large difference between the characteristic dimension of the grain and the thickness of the grain boundary. One way to reduce the condition number is to model each grain with finite elements of dimension similar to the thickness of the grain boundary. The result would be an inordinate number of elements that could not be handled by the work stations available for this research. Another approach is to invoke constraints to remove the largest eigenvalues which, in turn, would reduce the condition number and allow for a possible numerical solution for a sufficiently large domain so that meaningful results could be obtained [Hueck and Schreyer, 1992]. A method for efficiently incorporating constraints resulted in a paper submitted for publication [Schreyer and Parsons, 1994].

4. DETAILS OF RESEARCH

4.1 Ceramic Properties (Alumina)

Ceramic materials include oxides, carbides, sulfides, and intermetallic compounds, which are joined either by covalent or ionic bonds. Ceramic moduli are generally much larger than those of metals, reflecting greater stiffness of bonds. And since ceramics are largely composed of light atoms (oxygen, carbon, aluminum) and their structures are frequently not closely-packed, their densities are low. Most ceramics are crystalline, but unlike metals, they do not have closely-packed planes on which dislocation motion can occur. Therefore, ceramic materials tend to be very brittle compared to metals. Typical ceramics have very high melting temperatures (like alumina, 2050°C), which explains their good creep properties. Also, many these materials have superior wear resistance, and have been used for bearings and machine tools. Most ceramics, however, are too brittle for critical loading-bearing applications. Consequently, a vast amount of research has been devoted to improving the toughness of ceramics.

Most traditional ceramics are monolithic (single phase) and have very low fracture toughness. Our research was concentrated on monolithic ceramics, in particular aluminum oxide (i.e. alumina), which is widely used in industry.

4.2 Microstructural study (alumina)

Ceramics are formed by the application of a powder to high temperatures perhaps with the assistance of pressure and additives. The particles sinter together into a microstructure consisting of individual crystals or polycrystals, i.e., grains (made up of millions of small crystals [Ashby, 1986]) separated by grain boundaries and residual porosity (see Fig. 2). Each grain is more or less a perfect crystal. The grain boundary is obviously complicated, and can be considered as a thin region of atomic disarray where the density of atoms is slightly less than normal. Impurity and second phases are located at grain boundaries [Davidge, 1979]. The structure of the grain boundary in alumina was studied by Carter, et al. (1980) using electron diffraction and weak-beam (or dark field) imaging techniques in a Transmission Electron Microscope (TEM). The diffraction patterns and images show that the structure of the grain boundaries is periodic and the thickness of the grain boundaries is about 6-9 nm, which consists of dislocation arrays and facets.

4.3 Real-Time Fracture Study of Ceramics

In order to perform the real-time fracture study of ceramic materials, a closed-loop control system for the in-situ loading stage of the Scanning Electron Microscope (SEM) is needed. For simplicity, the loading stage was designed outside the SEM chamber to test its ability and will be mounted inside the SEM chamber in the future.

Closed-Loop Control Loading Stage

Fig. 3 (a) shows the tension-compression (T-C) stage which can be mounted to the SEM position stage. A single sliding brass block moves in a machined aluminum body assembly. To implement rotation of the lead-screw, a worm and ring gear(40:1 ratio) set-up is utilized. This set-up greatly reduces reverse rotation and provides a smooth application of lead-screw torque. A square shaft slides in a keyed slot running through the worm gear, and a 90 degree bevel gear system with another square free-sliding shaft

connects through a Delrin™ U-joint to a vacuum rotational-feed-through shaft. This shaft can be rotated by the geared stepper motor for precise feed-back control.

The closed loop design must have several properties, including, but not limited to, accurate load or displacement increments. Therefore, the objective is to create an integrated environment between all of the hardware elements necessary to perform tests. See Fig. 3 (b) for a schematic representation of the operating environment.

To give an overview of operating principles, knowledge of the involved components and hardware is needed including:

- 1: Scanning Electron Microscope
- 2: Loading stage capable of tension and compression testing
- 3: Step Motor and Controller from American Precision Industry
- 4: Galil Motion Control Card
- 5: Crack Opening Displacement (COD) gage from MTS
- 6: 1000 lb. Load Cell from Sensotech
- 7: 2-channel DC amplifier from Ectron
- 8: Microsoft's Virtual Basic

The Galil Motion Control card is the interface between the computer program to close the control loop and the step motor controller, which controls the motor, and puts load and displacement on the specimen. The card also receives two transducer signals from the loading stage. The COD gage returns the displacement between loading platforms and the load cell returns the approximate load on the specimen (see Fig. 3). The actual closed-loop program in the Galil card language has been completed. Microsoft's Virtual Basic is being used to create a driver program which is more visual and convenient. A detail discussion on the development of tension-compression loading stage is addressed in Appendix 3.

Compact Tension Specimen Preparation

Because sample preparation plays an important role in the ceramic test [Rice, 1993], the steps of sample preparation include the following:

1. The alumina bar was cut into small pieces by the diamond saw, and then the Isomet Low Speed Saw (made by Buehler Ltd.) was used to section the small piece into 1-4 mm thickness samples 30 mm X 30 mm, sectioned by using a low concentration diamond wafering blade.
2. The Ecomet Grinder and Polisher was used to grind and polish the surface. The diamond spot disc and diamond lapping film from 40 micron, 15 micron, 6 micron, 3 micron to 0.5 micron were used to obtain the shiny surface.
3. The holes on the specimen were drilled by an Ultrasonic Disc Cutter (made by Gatan Inc.). The disc cutter vibrates a tubular tool at a frequency of about 26 Kz against the sample. The tool is immersed in a drop of water-based hard grit (usually SiC 320 grit powder) slurry placed on the specimen. This causes particles in the slurry to impact the sample under the vibrating tool and erode away a circular impression.
4. Notches were sawed by an Isomet Low Speed Diamond Saw with a thin diamond wafering blade. Usually the chevron notch is cut.

5. After machining the specimens, the specimens were heated to 600 °C for 2 hours by a Thermolyne temperature-controlled furnace to release the residual stress caused by the machining. The heating and cooling rate was 2°C/min.

6. Aluminum was evaporated on the specimen surface by a Denton Vacuum DV-515 to produce a thin conductive layer.

Experimental Results

Grain boundaries in ceramic polycrystals frequently constitute planes of reduced fracture resistance; consequently, crack propagation often occurs along grain boundaries. Although grain boundary or intergranular fracture does not necessarily give rise to material weaker than materials that fail by transgranular fracture, the preferential failure along grain boundaries can, in some cases, enhance toughness. To provide insight into the toughness-determining mechanisms, both fracture paths and fracture surface were examined during load application.

Fig. 4 and Fig. 11 show the area around the notch tip before and after the specimen was broken, respectively. Load was applied carefully by constantly detecting the notch tip at high magnification. A crack started to propagate from the notch tip (see Fig. 5) after a certain load. It can barely be seen in low magnification. The profiles of the crack while holding the applied load are shown in Fig. 6 (a), (b), (c), (d), (e). The micrographs show that the crack started to propagate from the notch tip to 1100 μm in length. The width of the crack was 1-2 μm . It demonstrated significant crack deflection with the tortuosity of the crack path (Fig. 7 (a) and (b)).

Specific examples of SEM observations in alumina are shown in Fig. 8 (a) and (b). Fig. 8 (a) shows a bridging site in the crack wake some 950 μm behind the crack tip (also shown in Fig. 5 (a)); Fig. 8 (b) shows another bridging site in the crack wake some 1000 μm behind the crack tip (also shown in Fig. 5 (a)). Other bridging sites were also observed along the profile of the crack.

The fracture mode was predominantly intergranular, and it also was observed on the fracture surface (Fig. 9). No indication of a microcrack-cloud zone (also known as frontal-zone microcracking) was observed by SEM (see Fig. 10).

Summary of experimental results:

1. Crack-deflection processes operate when a crack interacts with microstructurally related features (e.g., weak interfaces or residual stress fields) that reduce deviation from planarity. As the crack deflects out of the plane normal to the applied stress, the stress intensity at the tip diminishes, reducing the crack driving force and improving the fracture toughness. K. T. Faber and Anthony G. Evans found intergranular crack-deflection toughening in silicon carbide [Faber, 1983].
2. Frontal-zone microcracking was not found around the fracture tip.
3. Since no energy was dispersed in front of the crack tip, crack interface grain bridging in the wake of the crack might be another cause of fracture toughening [Rodel, 1992].
4. The failure mode was predominantly intergranular.

4.4 Numerical Simulation of Microfracture

Based on the microstructural study of ceramic, it was proposed to numerically model in two dimensions a small specimen composed of a set of grains and grain boundaries, as shown in Fig. 1. Each grain can be roughly pictured as a homogeneous, anisotropic material with a multifaceted surface consisting of several planes. When a ceramic is loaded statically in tension, micrographs show that a dominant response mechanism is the appearance of cracks along grain boundaries while the individual grains remain intact. Therefore the mechanical features of the grain boundary itself must have a significant impact on the mechanical behavior of the ceramic. It is surprising that (to our knowledge) no attempt has been made to characterize the mechanical features of the grain boundary itself since it is the grain boundary that appears to provide the dominant characteristics of the mechanical behavior of ceramics. It is generally recognized that the nature of grain boundaries and microstructure affect the properties and behavior of ceramics. It is equally important to understand ceramic processing characteristics which affect the nature of the grain boundaries. In general, the mechanical properties of ceramics depend on the strength at grain boundaries, intergranular fracture due to weak grain boundaries and transgranular fracture due to strong grain boundaries.

Grain boundaries are considered as thin regions of elastic damaging material. An initial assumption is that each grain is isotropic. The grain boundary is supposed to be restricted to mode I behavior in the direction perpendicular to the face of the grain. This response is accomplished by utilizing a continuum model with a high shear modulus to preclude grain boundary sliding, a continually increasing modulus for compressive deformation, and a decreasing stiffness modulus as a damage model to simulate the mode I response for a tensile stress normal to the face of the grain.

Continuum Damage Mechanics

The nonlinear behavior of brittle materials is more accurately represented as the evolution of distributed microcracks rather than plastic deformation; therefore, continuum damage mechanics is the most appropriate approach. A phenomenological model [Yazdani and Schreyer, 1988] has been developed based on perceived modes of crack evolution. The value of this work is in its establishment of a firm thermodynamical foundation for the approach, and when combined with plasticity [Yazdani and Schreyer, 1990], the model provides excellent qualitative and quantitative results for a variety of load paths. Some theoretical implications of the use of continuum damage mechanics have been explored [Schreyer and Wang, 1990] as a precursor to the incorporation of essential aspects of microstructural approaches [Ju, 1990; Krajcinovic, et al., 1990] in a sufficiently simple manner to retain the feasibility of performing numerical simulations.

Conventional damage consists of the creation of voids and microcracks which consequently reduce the mechanical properties of a material, such as bulk modulus and shear modulus. Although damage is an anisotropic phenomenon, the initial approach will be to assume isotropy and consider the part of the damage reflected through the bulk modulus. A preliminary theory consistent with thermodynamics suggests that volumetric strain is a suitable measure of damage.

If the thermal effects are ignored, the internal energy, U , is assumed to be a function of the total strain tensor, ϵ , the "internal" variable consisting of the permanent strain tensor, ϵ^P , and the fourth-order elasticity tensor, E . With the assumption of linear elasticity, U is taken to be

$$U = \frac{1}{2} (e - e^P) : E : (e - e^P)$$

the application of the first and second (Clausius-Duhem inequality) laws of thermodynamics leads to the constitutive relation for stress, s ,

$$s = \frac{\partial U}{\partial e} = E : (e - e^P)$$

and the dissipation inequality

$$- \frac{\partial U}{\partial E} : \dot{E} - \frac{\partial U}{\partial e^P} : \dot{e}^P \geq 0 \text{ or } s : \dot{e}^P - \frac{1}{2} (e - e^P) : \dot{E} : (e - e^P) \geq 0$$

Suppose the damage process is parameterized through the use of a parameter, ω , which is monotonically increasing ($\omega \geq 0$). The evolution equations for damage can be given as follows:

$$\dot{E} = - \omega R(E, e, e^P) \quad \dot{e}^P = \omega m(E, e, e^P)$$

in which the dependence of the response functions, R and m , is shown. Since $\omega \geq 0$, the dissipation inequality becomes

$$D = \frac{1}{2} (e - e^P) : R : (e - e^P) + s : m \geq 0$$

which is satisfied if R is positive definite (conventional definition of damage) and if m forms an acute angle with s .

Suppose a damage function, f , is defined such that damage occurs when the state falls on the damage surface, $f = 0$, and for which the dissipation inequality is satisfied automatically. The inequality is met if

$$f = D - g^2(E, e, e^P)$$

Then when $f < 0$ damage is not occurring, and $f > 0$ is not a physical state.

Let I and i denote the fourth order and second order identity tensors, respectively. Define the spherical and deviatoric projections to be

$$P^{SP} = \frac{1}{3} i \otimes i$$

$$P^D = I - P^{SP}$$

$$\text{Then } P^{SP} : P^{SP} = P^{SP}$$

$$P^D : P^D = P^D \quad P^{SP} : P^D = 0$$

$$s^D = P^D : s$$

$$e^D = P^D : e$$

$$s^{SP} = P^{SP}; s = -Pi$$

$$e^{SP} = P^{SP}; e = \frac{1}{3} e_V i$$

in which $P = -(i:s)/3$ is the mean pressure, $e_V = e_V:i$ is the volumetric strain, and s^d and e^d denote the stress and strain deviators, respectively. With the use of the projection operators, the isotropic elasticity tensor is $E = 3KP^{SP} + 2GP^d$ in which K is the bulk modulus and G is the shear modulus. Both parameters may change with damage.

For the initial numerical investigation performed for this study we chose g to be a constant, and R to be the initial isotropic elastic tensor E_0 , and m to be the spherical part of the stress tensor (tensile). The result is a simple scalar isotropic damage model in which the bulk and shear moduli decay simultaneously with ω which is directly related to the volumetric strain (positive). A slightly more general model was then introduced in which R is an isotropic tensor not proportional to E_0 . The result is a two parameter isotropic damage model in which the bulk and shear moduli deteriorate at different rates with an increase in volumetric strain.

Damage Model

For the 3-D problem, the material stiffness matrix $[E]$ is 6 by 6. In the most general case of anisotropy, $[E]$ contains 21 independent coefficients. All coefficients change as the damage parameter ω changes. That is why continuum damage mechanics is so complicated even for the 2-D problem. In the engineering sense, many situations can be simplified or idealized. For an orthotropic material, the material displays extreme values of stiffness in mutually perpendicular directions, and $[E]$ contains 9 independent coefficients; for an isotropic material, the material behavior is the same in all directions, and material properties are commonly expressed as two independent coefficients, E and μ , or K and G .

In the 2-D problem, two different situations should be considered: the plane strain and the plane stress problem. For the plane strain isotropic problem, $[E]$ can be expressed as

$$[E] = \frac{E}{(1+\mu)(1-2\mu)} \begin{bmatrix} 1-\mu & \mu & 0 \\ \mu & 1-\mu & 0 \\ 0 & 0 & \frac{1-2\mu}{2} \end{bmatrix} = \begin{bmatrix} \frac{3(1-\mu)K}{(1+\mu)} & \frac{3\mu K}{(1+\mu)} & 0 \\ \frac{3\mu K}{(1+\mu)} & \frac{3(1-\mu)K}{(1+\mu)} & 0 \\ 0 & 0 & G \end{bmatrix}$$

and the volumetric strain is

$$e_V = \epsilon_{xx} + \epsilon_{yy}$$

For plane stress,

$$[E] = \frac{E}{1-\mu^2} \begin{bmatrix} 1 & \mu & 0 \\ \mu & 1 & 0 \\ 0 & 0 & \frac{1-\mu}{2} \end{bmatrix} = \begin{bmatrix} \frac{3(1-2\mu)K}{1-\mu^2} & \frac{3\mu(1-2\mu)K}{1-\mu^2} & 0 \\ \frac{3\mu(1-2\mu)K}{1-\mu^2} & \frac{3(1-2\mu)K}{1-\mu^2} & 0 \\ 0 & 0 & G \end{bmatrix}$$

and the volumetric strain is

$$\begin{aligned} \epsilon_v &= \epsilon_{xx} + \epsilon_{yy} + \epsilon_{zz} \\ &= \frac{1-2\mu}{1-\mu} (\epsilon_{xx} + \epsilon_{yy}) \end{aligned}$$

where E and μ are Young's modulus and Poisson's ratio, respectively, and K and G are bulk modulus and the shear modulus, respectively.

It is assumed that the damaging regions are confined to the grain boundaries, and the grains are elastic. For simplicity, the grains are assumed to be isotropic elastic, and the proportional scalar isotropic damage was used in the grain boundaries, i.e., the bulk K^{GB} and shear modulus G^{GB} of the grain boundaries decreased when their volumetric strains reach a certain volume. The superscript GB denotes the grain boundary. A damage parameter ω is introduced:

$$K^{GB} = (1 - \omega) K_0^{GB}$$

$$G^{GB} = (1 - \omega) G_0^{GB}$$

If $\omega = 0$, no damage has occurred; if $\omega = 1$, complete damage has occurred. K_0^{GB} and G_0^{GB} are initial values of K^{GB} and G^{GB} , respectively. K^{GB} (and G^{GB}) reduces from K_0^{GB} (and G_0^{GB}) to 0 as ω goes from 0 to 1.

The evolution of the damage parameter ω under tension is proposed to be (Fig. 12)

$$\begin{aligned} \omega &= \omega(\epsilon_0, \epsilon_v, k) \\ &= \begin{cases} 0 & \epsilon_v < \epsilon_0 \\ 1 - \exp \left(- \left(\frac{\epsilon_v - \epsilon_0}{\epsilon_0} \right) k \right) & \epsilon_v \geq \epsilon_0 \end{cases} \end{aligned}$$

where ϵ_v is volumetric strain, and ϵ_0 and k are parameters which can be determined from experimental data.

The Young's modulus E^{GB} is

$$E^{GB} = \frac{9K^{GB} G^{GB}}{3K^{GB} + G^{GB}}$$

$$= (1 - \omega) E_0^{GB}$$

and the Poisson's ratio μ is a constant:

$$\mu^{GB} = \frac{3K^{GB} - 2G^{GB}}{2(3K^{GB} + G^{GB})}$$

$$= \mu_0^{GB}$$

Dynamic Relaxation

Nonlinear structural analyses include materially nonlinear problems such as nonlinear constitutive equations with small deformations, geometrically nonlinear problems normally associated with buckling or a combination of both types of nonlinearities [Chen, and Schreyer, 1990]. The nonlinear analysis in the finite element method can be expressed as

$$[K] \{U\} = \{F\}$$

where $[K]$ is the structure stiffness matrix,
 $\{U\}$ is the vector of nodal degree of freedom, and
 $\{F\}$ is the vector of nodal loads.

$[K]$ and $\{F\}$ are regarded as dependent on $\{U\}$. The schemes for nonlinear problems are based on step-by-step load incrementation and an iteration procedure to correct the linearization.

In our finite element code, dynamic relaxation (DR) is used as an explicit incremental method for solving static problems. The DR method is based on the fact that the static solution is the steady state part of the transient response for a temporal-step load. This method is especially attractive for problems with highly nonlinear geometric and material behaviors, which includes limit points and regions of very soft stiffness. Use of the dynamic relaxation method makes the software simple. Since the method is explicit, it is unnecessary to form a global stiffness matrix; therefore, much less computer storage is needed than with implicit procedures such as Newton-type methods [Underwood, 1983, Gerstle, and Xie, 1992]. See Appendix 1 for the DR algorithm.

CoMeT

The whole modeling process was accomplished by coupling the nonlinear dynamic relaxation analysis program with the program CoMeT (Computational Mechanics Toolkit), and an interactive graphical shell for integrated computational mechanics. For each iteration, the new damage values of K and G were calculated in terms of the current volume strain in each Gaussian point and compared with the former damage. After one step was finished, a data-base file was output that could be processed by CoMeT.

Mesh

Based on crystal structure and micrographs of the alumina, the shape of each grain was hypothesized as hexagonal and modeled with six three-node triangular elements; the uniform grain boundaries are distributed between the grains, which was represent with a small three-node triangular element and a four-node quadratic element (Fig. 1). For simplicity, a small mesh with a grain size of 10 mm was generated, and the thickness of the grain boundaries was 0.5 mm (Fig. 1). The aspect ratio of the grain boundary element was 10:1. An element performs best if its shape is compact and regular. According to Cook [1989], an element tends to stiffen and lose accuracy as its aspect ratio increases, although specific details are not given. Here, we show that good results are achieved even with a large aspect ratio.

Numerical Results

To illustrate the proposed damage model, two sample problems were considered; one was a small problem with 19 elements, another was a large problem with 161 elements. The model problems consist of a specimen in which the displacement on one boundary is applied uniformly in the y direction under the assumption of plane stress. One boundary was traction free and the other two boundaries had fixed displacement in the x and y directions, respectively. In the grain regime, the material is assumed to be isotropic as defined through Young's modulus, E^G , and Poisson's ratio, μ^G . Material parameters, which are considered to be representative of alumina ceramic, were chosen as follows: $E^G = 372$ GPa, and $\mu^G = 0.22$. Equivalently, bulk modulus $K^G = 228$ GPa, shear modulus $G^G = 152$ GPa, were used for the grain. The initial material properties of grain boundaries affect the computational results.

Small Mesh Model Problem

The finite element mesh and the boundary conditions used in the analysis are shown in Fig. 13. First, the initial material properties of grain boundaries used in the numerical analysis were assumed as the same values as that for the grains, i.e., $K_0^{GB} = K^G = 228$ GPa, $G_0^{GB} = G^G = 152$ GPa; equivalently, $E_0^{GB} = 372$ GPa, and $\mu_0^{GB} = 0.22$. The undeformed mesh is shown in Fig. 13. The deformed meshes at the 20th step and 30th step are shown in Fig. 14(a) and 14(b). The larger deformation that occurred in the shadow elements showed that the microcrack started to nucleate and propagate along the grain boundaries.

Fig. 14 (a) shows the crack nucleating at the central grain boundary (marked), and crack propagation along the grain boundaries is shown in Fig. 14 (b). The displacement and the total corresponding nodal force curve is illustrated in Fig. 14 (c). The nonlinear behaviors (hardening and softening) of ceramics under uniaxial tension can be seen. The filled circles indicate the loading steps.

Large Mesh Sample Problem

The large mesh sample problem includes 12 grains and the number of elements is 161. The mesh is shown in Fig. 15 (a). The features of the proposed model are shown below:

1. Microcrack nucleation:

The undeformed mesh with 161 elements is shown in Fig. 15 (a). With $E_o^{GB} = E^G$, the deformed mesh at the 23rd step is shown in Fig. 15 (b). It can be seen (Fig. 15 (b)) that the grain boundaries (in shadow) show a larger deformation than the other elements, i.e., the microcracks have been created on the grain boundaries. Fig. 15 (c) gives the displacement and corresponding total nodal force curve for the condition of $E_o^{GB} = E^G$.

2. Crack propagation:

As the displacement is continuously applied, the deformed mesh shows that the microcracks connect together and propagate. Fig. 16 (a), (b), (c) and (d) show results at the 25th, 26th, 27th and 29th load steps. From the deformed mesh, crack nucleation and propagation along the grain boundary can be seen clearly.

3. Microcrack and void effects:

The program could also simulate elements as microcracks and voids when the initial mechanical properties of grain boundaries, like E_o^{GB} , were given as very small. One element was simulated as a microcrack as shown in Fig. 17 (a) (marked elements). The deformed mesh is shown in Fig. 17 (b) and (c). Compared with Fig. 15 (b), Fig. 17 (b) shows that the crack starts to propagate from the weakened element (marked element), i.e., the crack propagates from the microcracks. Fig. 17 (c) shows the difference between the force vs. displacement curves with and without existing microcracks. The existing microcrack reduced the strength of the ceramic and exhibited more brittle material properties than the ceramic without microcracks.

4. Inclusion effect:

Fig. 16 (d) shows that the main crack propagates along the grain boundaries in the upper part of the specimen. The inclusion was introduced in the marked element, i.e., a larger value of stiffness was used in the marked element (Fig. 18(a)). From the deformed mesh, the position of the main crack was changed due to the introduced inclusion element, as can be seen in Fig. 18 (b) and (c). Compared with Fig. 16, the inclusion deterred the crack nucleation and propagation which would otherwise run through it before. Fig. 18 (d) shows the difference between the force vs. displacement curves with and without an inclusion. The strength of the ceramic was enhanced by introducing an inclusion, but ductility was decreased.

5. Effects of mechanical properties of the grain boundary on macro-behavior:

In the above computations, the initial mechanical property of the grain boundary was assumed to be the same as the grain. Generally, the grain boundary is weaker than the grain for intergranular fracture. Fig. 19 gives the displacement and corresponding total nodal force curve for the case of $E_o^{GB} = E^G$ and $E_o^{GB} = 0.75 E^G$. Mechanical properties of the grain boundary have a significant effect on the macroscopic behaviors. The weaker the grain boundaries, the less the strength and ductility of ceramic. The failure mode is the same as that shown in Fig. 16.

Voronoi diagram

One of the major obstacles in numerical modeling of ceramic is the geometrical complexity in grain microstructure. Since many properties of ceramics are determined by their grain microstructure, prediction and control of microstructural characteristics are important. So far, a number of computer simulations have been made for microstructures [Anderson, et al, 1984, 1989, Wejchert, 1986].

One of the methods for simulating the grain geometry and topography is the model known as the Voronoi diagram. Given a number of points in the plane, the Voronoi diagram divides the plane according to the nearest-neighbor rule: Each point is associated with the region of the plane closest to it; (Fig. 20 (a)) [Aurenhammer, 1991].

A program for generating the Voronoi diagram written in C language is available in the public domain. The program was run and displayed by Silicon Graphic (which is in the Department of Computer Science at UNM). The output file, which included the coordinates of the vertices of polygons and line connections was transferred to the Sun Station, then the Voronoi diagram was redisplayed by CoMeT as shown in Fig. 20 (b).

For finite element modeling, a thin layer between grains was generated as a grain boundary. The grain was meshed with 3-node triangular elements, and the grain boundary was meshed with 4-node quadratic elements and 3-node triangular elements (Fig. 21).

Scalar isotropic damage mechanics

For simplicity, isotropic damage mechanics was used first. As we mentioned before, the microcracks started to nucleate at the grain boundaries, and then propagated along the grain boundary, i.e., an intergranular fracture as shown in Fig. 22 (a), (b), (c), and (d). The grain's rotation can be observed in the deformed mesh.

Two-parameter isotropic damage mechanics

The grain boundary is restricted to mode I behavior, perpendicular to the face of the grain. This response is accomplished by utilizing a continuum model with a higher shear modulus to preclude grain-boundary sliding, a continually increasing modulus for compressive deformation, and a decreasing stiffness modulus as a damage model to simulate the mode I response for a tensile stress normal to the face of the grain.

The material stiffness matrix $[E]$ can be expressed as

$$[E] = \begin{bmatrix} \frac{3(1-\mu)K}{(1+\mu)} & \frac{3\mu K}{(1+\mu)} & 0 \\ \frac{3\mu K}{(1+\mu)} & \frac{3(1-\mu)K}{(1+\mu)} & 0 \\ 0 & 0 & G \end{bmatrix} \quad (\text{for plane strain})$$

and

$$[E] = \begin{bmatrix} \frac{3(1-2\mu)K}{1-\mu^2} & \frac{3\mu(1-2\mu)K}{1-\mu^2} & 0 \\ \frac{3\mu(1-2\mu)K}{1-\mu^2} & \frac{3(1-2\mu)K}{1-\mu^2} & 0 \\ 0 & 0 & G \end{bmatrix} \quad (\text{for plane stress})$$

where K and G are the bulk modulus and shear modulus, respectively in general cases. The material stiffness matrix [E] changes as K and G change, and Poisson's ratio μ remains constant for alumina: $\mu = 0.22 - 0.23$.

Two damage parameters ω_1 and ω_2 were introduced:

$$K^{GB} = (1 - \omega_1) K_0^{GB}$$

$$G^{GB} = (1 - \omega_2) G_0^{GB}$$

and $\omega_1 > \omega_2$ (see Fig. 23).

Using the two-parameter isotropic damage model, the computational results are shown in Fig. 24 (a), (b), (c), and (d). The microcracks started to nucleate at the grain boundaries, and propagated along the grain boundary until finally a macrocrack was formed.

Fig. 25 shows the difference of the load and displacement curves between the two types of damage modes. The grain boundaries with a higher shear modulus prevented the rotation of grains, but the strength and ductility of ceramics were reduced.

Summary of numerical investigation:

1. Based on the continuum damage mechanical model, microcrack nucleation, crack propagation, microcrack and void effect, and inclusion effect were simulated numerically by a small specimen composed of a set of grains and grain boundaries in two dimensions.
2. The grain size can be randomly generated by the Voronoi Diagram, so that the computational mesh can be more realistic. The tortuosity of the crack path and crack bridging were observed by the numerical results.
3. Because of the computational limitation of the work station, the size of mesh cannot be generated large enough to compare the actual size of specimens, but many fracture mechanisms can still be observed in numerical investigations.

4.5 Summary and Conclusion

Experimental

It is generally recognized that the nature of grain boundaries and microstructures affect the properties and behavior of ceramics. It is important to understand ceramic processing characteristics which affect the nature of the grain boundaries. Different processing techniques have been explored to produce the desired microstructures for ceramics. Several processing techniques have been explored to produce the desired microstructure of alumina. It was found that Two-Stage sintering and MgO-doped Al_2O_3

can be combined to produce a high performance alumina. The result is better alumina with an improved, more uniform and homogenous microstructure.

Examination of microstructures has indicated that mechanical properties depend on the population and location of pores and grain size distribution. The fracture resistance of ceramics can be affected by microstructural variables such as porosity and grain size distribution. Larger grain-size ceramics are usually more prone to microfracture. Porosity located at grain boundaries degrades the fracture resistance in proportion to the volume concentration of voids; however, voids within grains can enhance toughness during transgranular fracture.

An image analyzer and an image editor (NIH IMAGE 1.41) were used for quantifying the grain size distribution from micrographs. The micrographs were redrawn by using a transparent material so that the grains and grain boundaries could be clearly identified. The image was obtained by scanning the redrawn micrographs into a computer. A digital readout displayed the area for each grain from the images. Using a ruler, the multiplying factor was obtained by converting the picture-point units to units of square micrometers. From this area, the diameter(μm) of the equiarea circle was computed. The diameter is used as the grain size measure.

In each micrograph, different magnifications were used. Using the statistical program as developed through this research, we obtained the final result of the frequency grain size distribution for each specimen using different sintering processes. The grain size distributions are given in Fig. 26. The numbers of grains for each grain size distribution were 100, 250, 124, 166, 222, and 215 corresponding to sintering processes #1 through #6, respectively. The frequency grain size distribution shifts toward the coarse end of the size spectrum as a function of sintering time and temperature. Similar conclusions can also be made for void size distribution where average void size shifted to larger void size as a function of sintering time and temperature as shown in Figure 27. It is known that, during sintering, very high temperatures and long periods of time lead to exaggerated grain growth. The grain size distribution can be approximately fitted to a Lognormal Distribution.

The X-ray diffraction method was used to determine the shape and size of alumina's unit cell. The data demonstrate that the alumina has a hexagonal crystalline structure. In addition to the X-ray diffraction scan, the Back-Reflection Laue method was used in qualitative texture analysis to determine the distribution of grain orientation in the sintered alumina. Crystal sizes of more than 10 μm were found to be present and the alumina crystals were randomly oriented.

One of the objectives of this research is to study the fracture process of the ceramic in real time and to measure the strain field in the vicinity of the crack including the bridging zones. A fast-scanning electron microscope(FSEM) for dynamic microscopy applications was used to capture the fracture events in the ceramic. This equipment is particularly suitable for microstructural studies for dynamically loaded materials, as it captures images at a high speed. The SEM chamber was also modified to accommodate an in-situ tension-compression loading device to fracture ceramics. Several problems have arise including the inadequacy of force to achieve ceramic fracturing and excessive noise that was produced by step motor instrumentation. Many improvements have been made such as application of an adequate force driven by a microstepper motor and closed-loop control capability by using filtering techniques.

Numerical

Continuous damage mechanics is an appropriate approach for analyzing the nonlinear behavior of quasi-brittle materials. It was proposed to numerically model in two dimensions a small region composed of a set of grains and grain boundaries. Each grain was modeled as an elastic material while the grain boundary was considered to be a thin region of elastic damaging material. The randomly distributed grain geometry was simulated by a computer program which produced the Voronoi diagram. Both scalar and two-parameter isotropic damage models were used in the computation.

Microcrack nucleation, crack propagation, microcrack and void effect, and inclusion effect were simulated numerically on a small specimen composed of a set of grains and grain boundaries in two dimensions. The tortuosity of the crack path and crack bridging were observed through the numerical results.

Numerical examples have also demonstrated the following observations: Microcracks always started to nucleate on the grain boundary first if the grain boundary was weaker than the grain. If a microcrack already existed, then the crack started to propagate from the microcrack along the grain boundary. The existing microcracks weakened the ceramic and exhibited a more brittle failure mode as shown in Fig. 17(d). When an inclusion existed in the grain boundary, it deterred the crack propagation through it, and the crack initiated from the other weaker site. Inclusions enhanced the strength of ceramic, but reduced its ductility (Fig. 18(d)). Mechanical properties of the grain boundary have a great effect on macroscopic behaviors. The strength and ductility of brittle ceramic decreased as the strength of the grain boundary decreased.

5. Proposed Extension

Experimental

Most traditional ceramics are monolithic (single phase), such as alumina, and have very low fracture toughness. Because they do not yield to loading pressure, monolithic ceramics behave as ideally brittle materials, and a propagating crack needs only to overcome the surface energy of the material. The new generation of ceramics, however, includes multiphase materials and ceramic composites that have vastly improved toughness. The micromechanisms that lead to improved fracture resistance in modern ceramics include microcrack toughening, transformation toughening, ductile phase toughening, fiber toughening, and whisker toughening. Modern ceramics also display much larger ductility than monolithic ceramics.

Ceramic composites are considered an enabling technology for advanced aircraft and space propulsion engines and space power systems. Catastrophic fracture remains an issue. Our efforts are toward the in-depth understanding of the toughening mechanism under both static and dynamic loading of ceramic composites.

In particular, our unique experimental capabilities include a Fast Scanning Electron Microscope (FSEM), for which Dr. Wang, the co-principal investigator, received a patent in October, 1993. Specification and capabilities of the FSEM is described in Appendix 4. Through this research we have also developed an in-situ dynamic closed-loop controlled tension-compression loading device. This allows one to observe in real-time the fracture and toughening mechanisms of reinforced ceramic-matrix composites materials subjected to static, cyclic dynamic loading.

Future research will include the study of toughening mechanisms of compact tension specimens of alumina and SiC-whisker-reinforced alumina using FSEM and an in-

situ loading device inside the FSEM chamber. Measurements will include load, fracture opening displacement, crack extension, crack-growth rate for cyclic loading, number of cycles to failure and stress intensity factor. Microstructure observation will include real-time fracture propagation micrographs in a video set-up. From the micrographs one should be able to distinguish the fracture mode (intergranular or transgranular) and toughening mechanisms due to static and cyclic fatigue loading.

Theoretical

A detailed understanding of ceramics requires constitutive models for grains and grain boundaries, and numerical simulations of the failure of grain boundaries; the resultant evolution of microcracks can be seen as crack branching and the ultimate development of a macrocrack. This research has provided a good initial analysis which shows that a combination of continuum damage as a means for simulating material failure, the use of Voronoi diagrams to construct realistic grain topologies, and a robust solution algorithm for computations beyond the peak force can begin to show essential aspects of the failure process.

Verification of the constitutive equation used for the grain boundary, and even the grains, remains a difficult problem. Since the behavior is highly inhomogenous, and because of the small size of a typical grain, it is hard to imagine that direct correlation with experimental behavior will ever be possible. A much more realistic approach is to postulate reasonable constitutive equations for grains and grain boundaries, and then determine the response of a specimen subjected to boundary conditions analogous to those applied experimentally. Comparisons of predicted load-displacement curves and failure modes with experimental data can then provide a means for an indirect verification of constitutive equations.

If quantitative predictions are to made, a significant enhancement to the computational approach is required. For example, three-dimensional simulations must be performed on specimens containing a significantly larger number of grains if the effects of artificial constraints imposed by boundary conditions is not to dominate the solution. Even with powerful computers, three-dimensional simulations must be limited in scope if solutions are to be obtained at reasonable cost. Every effort must be made to reduce the complexity of the problem if such simulations are to be feasible.

Since the current finite element study involving grain boundaries in ceramics is meant to be only a first step to show that the approach is plausible, no attempt was made to incorporate features which might be required for larger two-dimensional and three-dimensional simulations. An important procedure would be to constrain out modes that are not essential for the problem at hand, but that can cause ill conditioning or excessively small steps for dynamic relaxation. For example, it is highly unlikely that bending modes in the four-node quadrilateral element are important for the grain boundary. Furthermore, one might want to study the extreme case of rigid grains (modeled through the use of constraints) so that the grain boundary response associated with a larger number of grains could be analyzed, especially in three dimensions.

In light of its importance, it is surprising that efficient algorithms for the routine incorporation of constraints in linear algebraic equations is not a subject widely studied. As part of this project a step was taken to show that multiple constraints could be invoked directly without a major modification to the governing matrix, and both static and dynamic examples were given for one-dimensional problems [Schreyer and Parsons, 1994]. The results are given in Appendix 5.

It is proposed that this approach be extended to two and three dimensions for application to the study of grains and grain boundaries. Another natural application would be to the study of fibers in ceramics where the fibers could be initially modeled as inextensible constraints. Fiber breakage could then be simulated as a release of the

constraint. There are other potential uses for such an algorithm in connection with constitutive equations in which constraints of zero values for certain components of stress after material failure could be imposed.

In summary, rapid advances in the use of a fast-scanning electron microscope are providing unique experimental data. If these results are to be utilized to their greatest extent, numerical simulations are necessary to provide information at the level of grains and grain boundaries. Three-dimensional simulations are the only realistic approach, but this will require innovative numerical procedures to obtain solutions. The efficient use of constraints in conjunction with constitutive equations based on continuum damage mechanics will be an important aspect of such a study.

6. References

Anderson, M. P., Srolovitz, D. J., Grest, G. S., and Sahni, P. S., 1984, "Computer simulation of grain growth-I. Kinetic," *Acta metall.* Vol. 32, No. 5, pp. 783-791.

Anderson, M. P., Srolovitz, D. J., Grest, G. S., 1989, "Computer simulation of normal grain growth in three dimensions," *Phil. Mag. B*, Vol. 59, No. 3, pp. 293-329.

Ashby, M. F., Jones, D. R. H., 1986, Engineering Materials 2: An Introduction to Microstructure, Processing and Design, Pergamon Press.

Aurenhammer, F, 1991, "Voronoi Diagrams - A Survey of a Fundamental Geometric Data Structure," *ACM Computing Surveys*, Vol. 23, No. 3.

Chen, Z., and Schreyer, H. L., 1990, "A Numerical Solution Scheme for Softening Problems Involving Total Strain Control," *Computer & Structure*, Vol. 37, No. 6, pp. 1043-50.

Carter, C. B., Kohlstedt, D. L. and Sass, S. L., 1980, "Electron Diffraction and Microscopy Studies of the Structure of Grain Boundaries in A_2O_3 ," *J. Am. Ceram. Soc.*, 63, [11-12], pp. 623-27.

Cook, R. D., Malkus, D. S., and Plesha, M. E., 1989, Concepts and Applications of Finite Element Analysis, 3rd edition, John Wiley & Sons, New York.

Davidge, R. W., 1979, Mechanical Behavior of Ceramics, Cambridge University Press, Cambridge.

Evans, A. G., 1990, "Perspective on the Development of High-Toughness Ceramics," *J. Am. Ceram. Soc.*, 73(2), pp. 187-206.

Faber, K. T., and Evans, E. G., 1983, "Crack Deflection Process - I. Theory," *Acta Metall.*, Vol. 31, No. 4, pp. 565-575.

Gerspiller, W. H. and Xie, Ming, 1992, "FEM Modeling of Frictitious Crack Propagation in Concrete," *J. Engrg. Mech.*, Vol. 118, No. 2.

Horii, H., and Nirmalendran, S., 1990, "Roles of microcracking and bridging in fracture of quasi-brittle materials," *Proceedings of the symposium on Micromechanics of Failure of Quasi-Brittle Materials*, Edited by S. P. Shah, S. E. Swartz and M. L. Wang, Elsevier Applied Science, London, Held at Albuquerque, NM, 6-8 June 1990, pp. 569-578.

Hueck, U., and Schreyer, H. L., 1992, "The Use of Orthogonal Projections to Handle Constraints with Applications to Incompressive Four-Node Quadrilateral Elements," *International Journal for Numerical Methods in Engineering*, Vol. 35, pp. 1633-1661.

Mindess, S., 1990, "The fracture process zone in concrete," *Proceedings of NATO Advanced Research Workshop, NSF Center for Science and Technology of Advanced Cement-Based Materials, Toughening Mechanisms in Quasi-Brittle Materials*, Edited by S. Shah, Northwestern University, Evanston, IL, pp. 335-350.

Preparata, F. P. & Shamos, M. I., 1985, *Computational Geometry: An Introduction*, Springer-Verlag, New York Inc.

Rice, Roy W., 1993, "Correlation of Machining-Grain-Size Effects on Tensile Strength with Tensile Strength-Grain-Size Behavior," *J. Am. Ceram. Soc.*, 76 [4] 1068-70.

Rodel, J., Kelly, J. F., and Lawn, B. R., 1990, "In-Situ Measurements of Bridged Crack Interfaces in Scanning Electron Microscope," *J. Am. Ceram. Soc.* 73 [11], pp. 3313-18.

Schreyer, H. L., and Wang, M. L., 1990, "Elementary constitutive relations for quasi-brittle materials based on continuum damage mechanics," *Proceedings of the symposium on Micromechanics of Failure of Quasi-Brittle Materials*, Edited by S. P. Shah, S. E. Swartz and M. L. Wang, Elsevier Applied Science, London, Held at Albuquerque, NM, 6-8 June 1990, 95-104.

Schreyer, H. L. and Parsons, D., 1994, "Direct Application of Constraints to Symmetric Algebraic System," Submitted for publication.

Shah, S. P., and Maji, A., 1989, "Experimental observation of cracking and damage," *Cracking and damage: strain localization and size effect, Proceedings of the France-us Workshop on strain localization and size effect due to cracking and damage*, held at Laboratoire de Mechanique et Technologie, Cachan, France, 6-9 Sept. 1988, Edited by J. Mazars and Z. P. Bazant, 15-29.

Schockey, D. A., 1990, "Damage under dynamic conditions due to flier plates," *Presentation at Workshop on Continuum Damage Mechanics*, Sandia National Laboratories, Livermore, CA, 11-13 June.

Suaris, W., Ouyang, C. and Fernando, V. M., 1990, "Damage model for cyclic loading of concrete," *Journal of Engineering Mechanics*, Vol.116, No. 5, pp. 1020-1035.

Underwood, P., 1983, "Dynamic Relaxation," *Computational Methods in Mechanics for Transient Analysis*, T. Belytschko, and T. J. R. Hughes, eds., North-Holland Publishing, Amsterdam, The Netherlands, pp. 245-65.

Van Mier, J. G. M., 1990, "Fracture process zone in concrete: a three dimensional growth process," *Fracture Behavior and Design of Materials and Structures, 8th Biannual European Conference on Fracture*, Torino, Italy, Oct. 1-5, pp. 567.

Wang, M. L., Schreyer, H. L., and Rutland, C. A., 1990, "Internal deformation measurements using real time X-rays," *Experimental Techniques*, Volume 16, No. 4, pp. 43-47.

Wang, M. L., 1992, "Fracture Study Using Fast Scanning Electron Microscope (FSEM)," *Experimental Techniques*, Volume 16, No. 1 pp. 29-36.

Wejchert, J. Weaire, D. and Kermode, J. P., 1986, "Monte Carlo simulation of the evolution of a two-dimensional snap froth," *Phil. Mag. B*, Vol. 53, No. 1, pp. 15-24.

Yazdani, S., and Schreyer, H. L., 1992, "An Anisotropic Damage Model with Dilatation for concrete," *Mechanics of Materials*. Vol. 7, pp. 231-244.

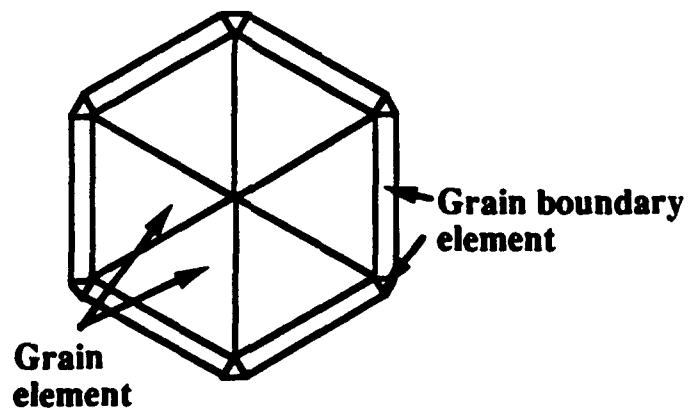
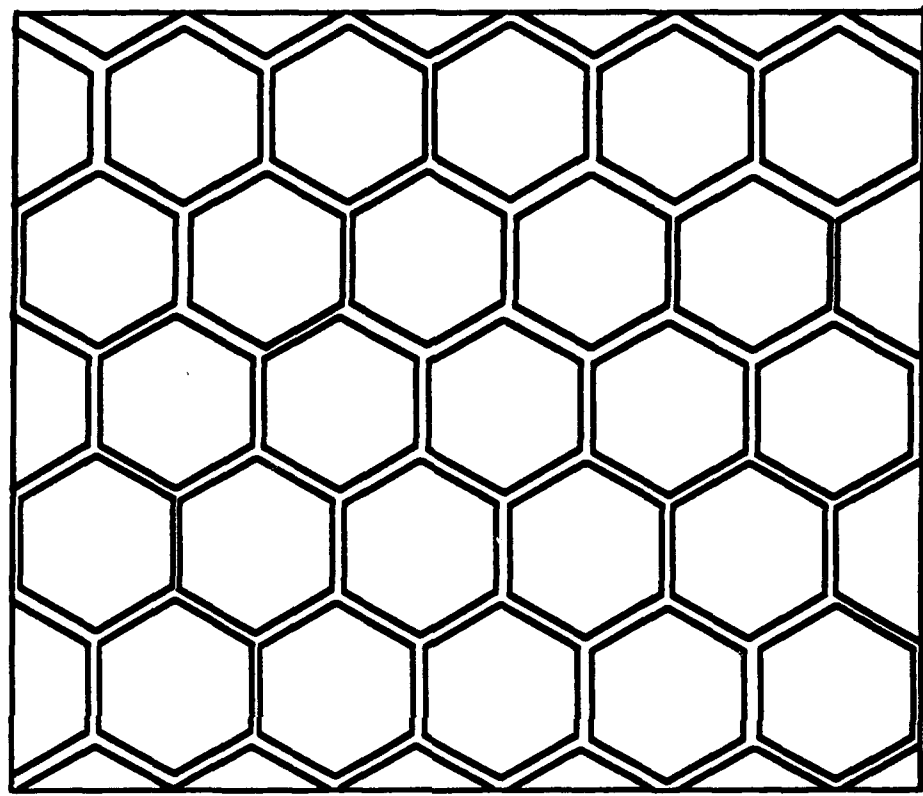


Figure 1. The idealized mesh of the alumina; the zooming of a grain (6 triangle elements) and grain boundary (6 triangle elements and 6 quadratic elements).

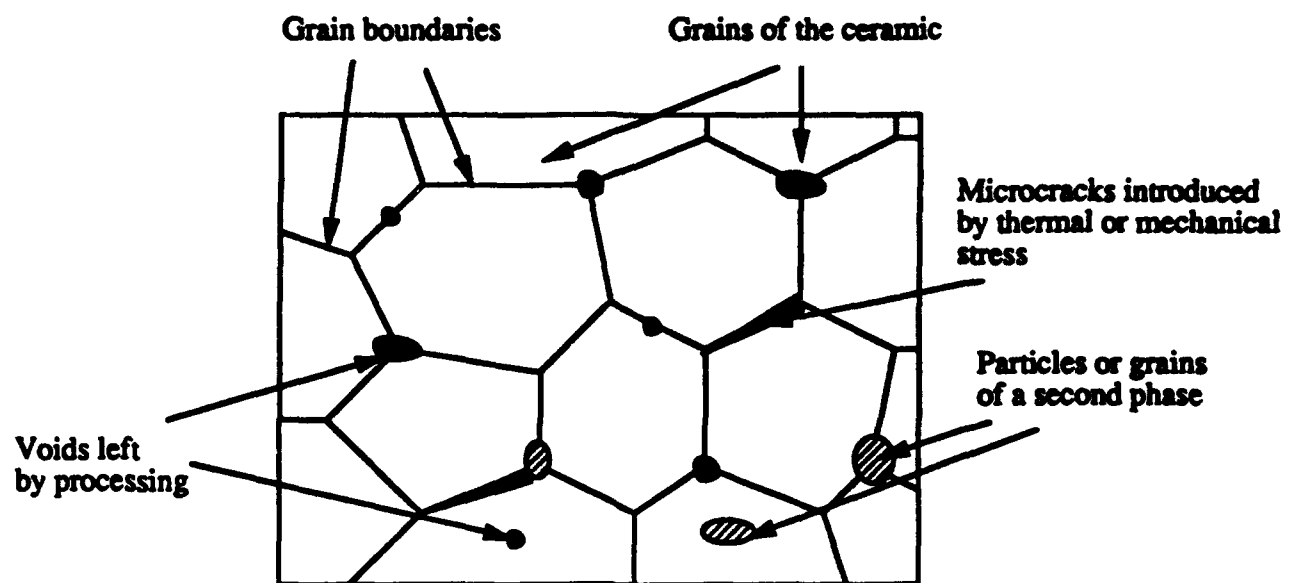
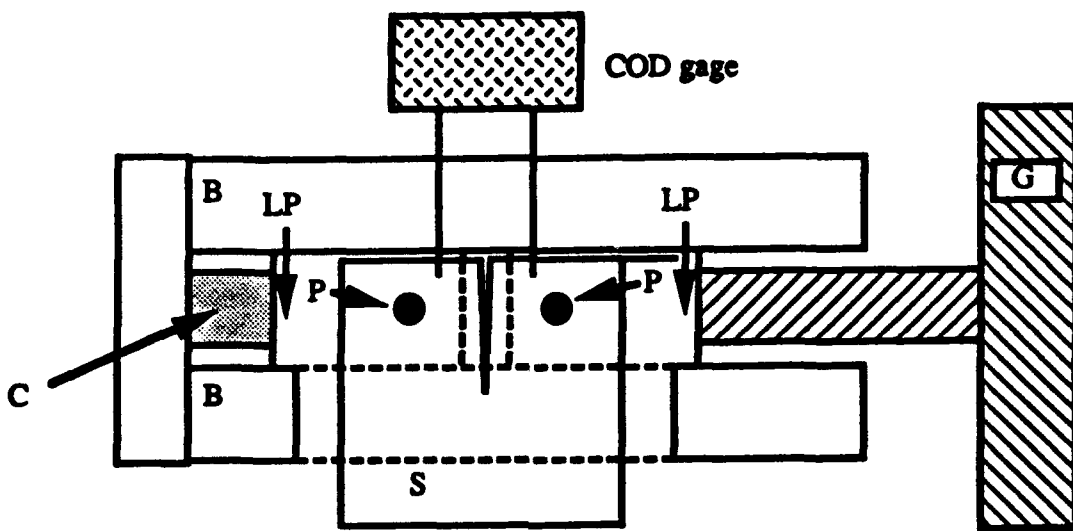


Figure 2 (a) Schematic of the microstructure of the ceramic.



Figure 2 (b) Micrograph of Alumina after polished and thermally etched.



S ---- Specimen
 G ---- Worm Gear
 P ---- Loading pins
 C ---- Load cell
 LP --- Loading platforms
 B ---- Base of loading stage

Figure 3 (a) Schematic of the loading stage

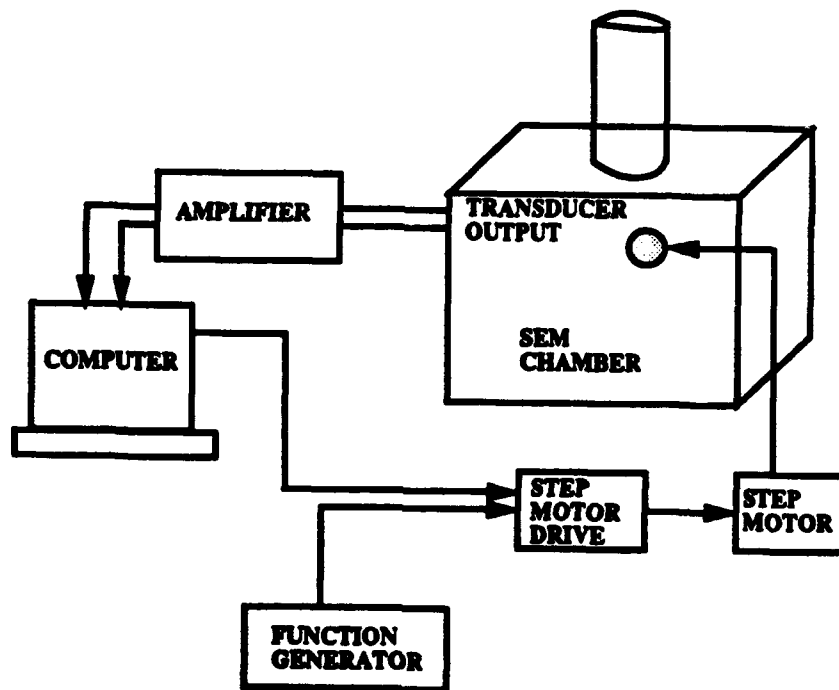


Figure 3 (b) Schematic illustration of close-loop control of loading device.

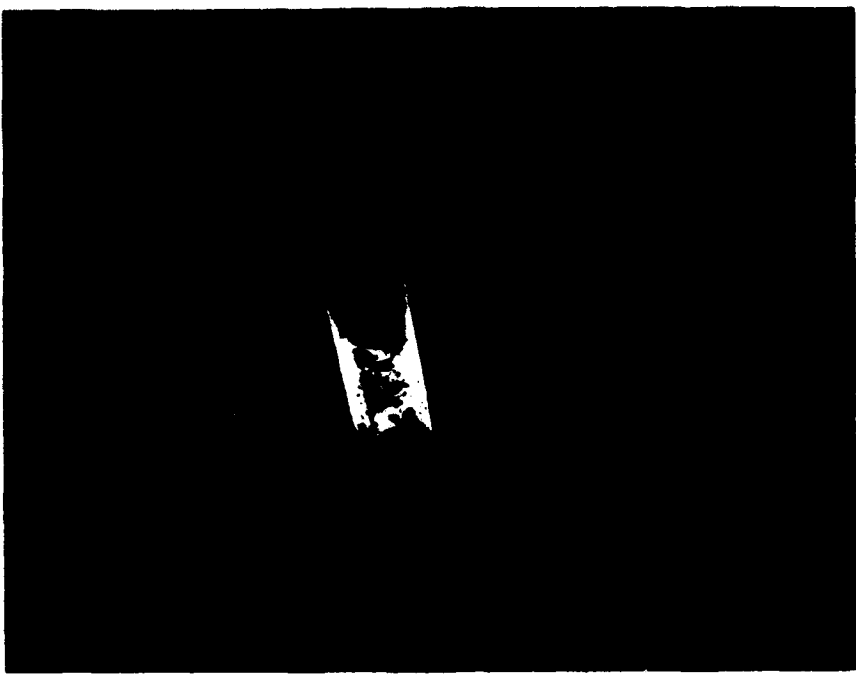


Figure 4 Micrograph of the notch tip before loading

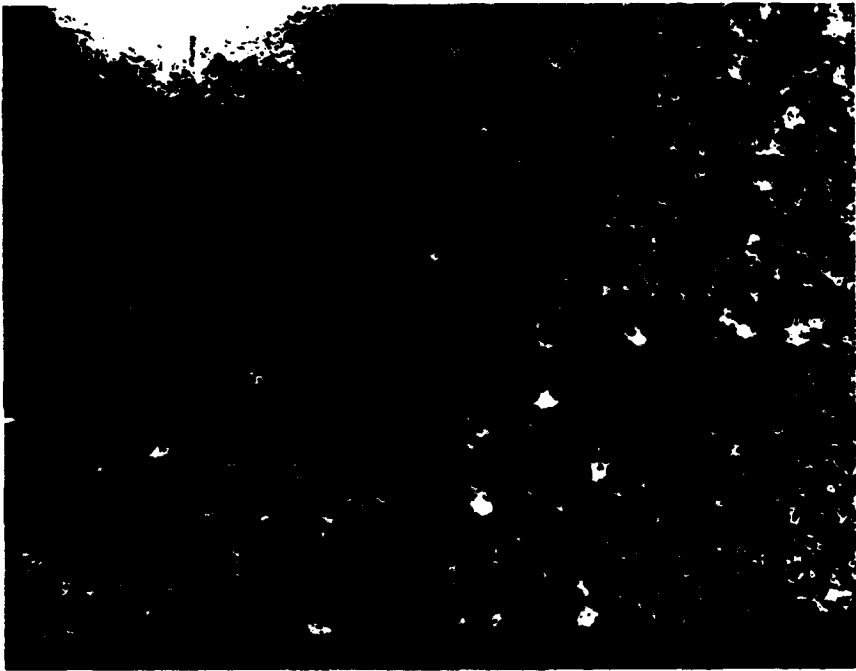


Figure 5 A crack propagated from the notch tip (upper white arch).



Figure 6 (a) The profile of the crack (crack propagated from upper part).



Figure 6 (b) The profile of the crack (crack propagated from upper part).



Figure 6 (c) The profile of the crack (crack propagated from upper part).



Figure 6 (d) The profile of the crack (crack propagated from upper part).



Figure 6 (e) The profile of the crack (crack propagated from upper part).

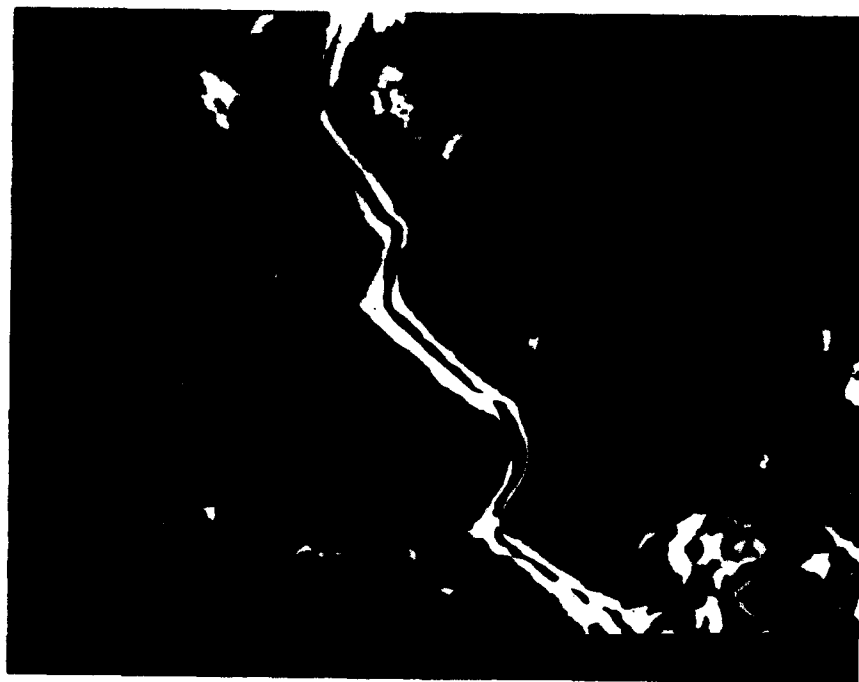


Figure 7 (a) The tortuosity of the crack in the wake of the crack.

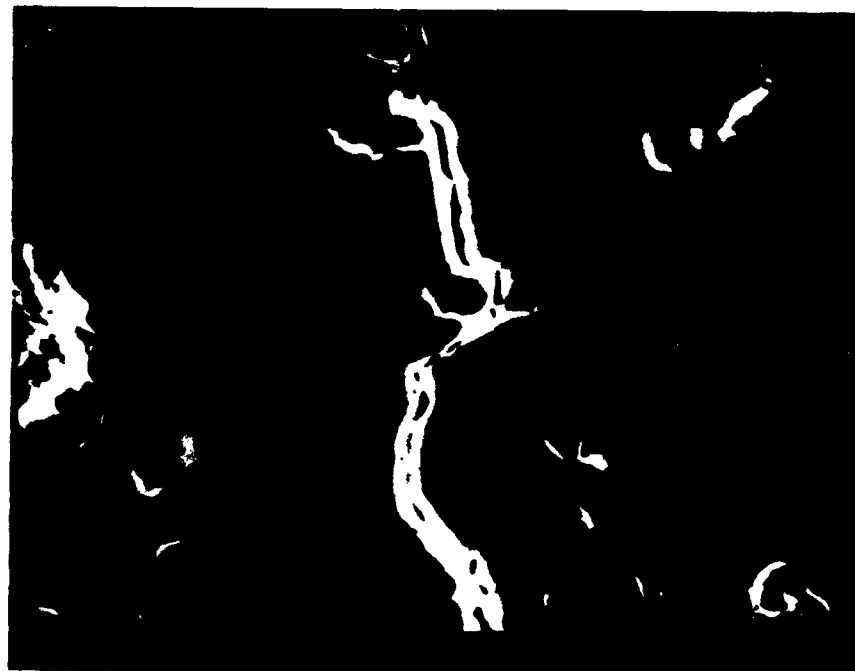


Figure 7 (b) The tortuosity of the crack in the wake of the crack.



Figure 8 (a) The grain-bridging site 950 mm behind the crack tip.



Figure 8 (b) The grain-bridging site 1000 mm behind the crack tip.

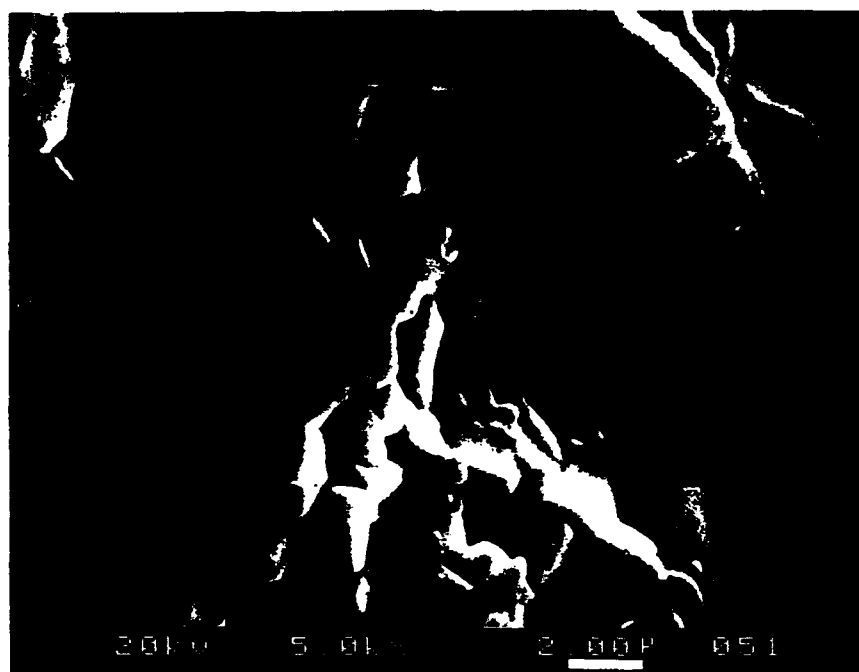


Figure 9 Micrograph of the fracture surface of Alumina



Figure 10 The crack tip at higher magnification.

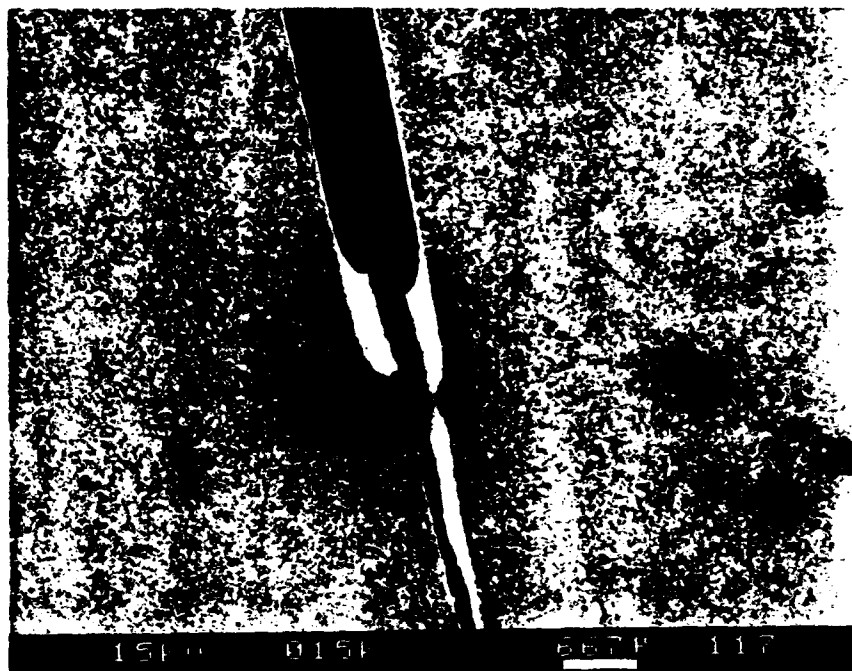


Figure 11 Micrograph of the notch tip after crack propagation.

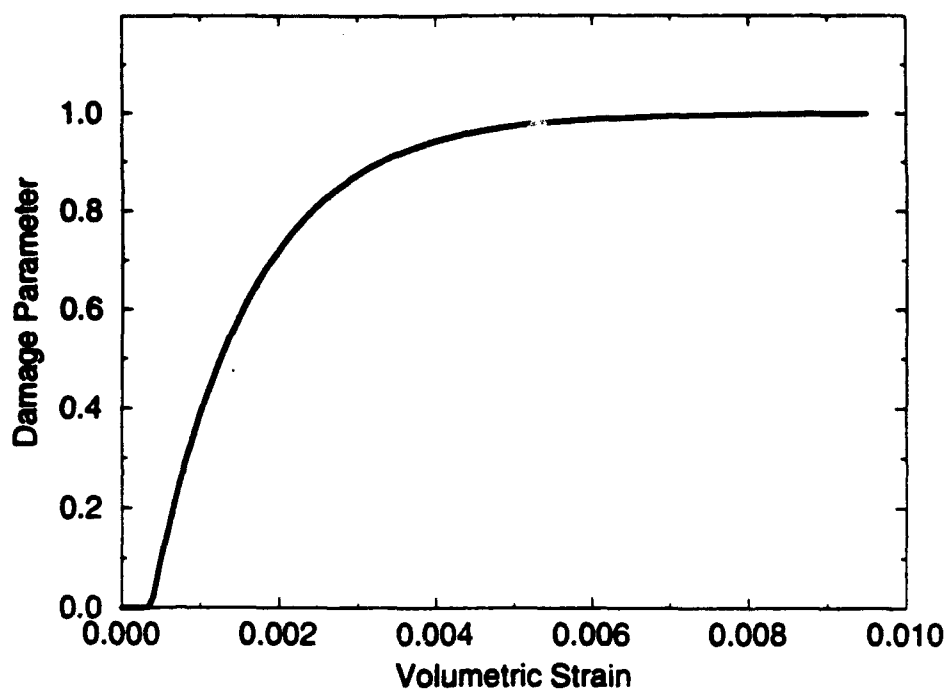


Figure 12 (a) The proposed evolution of damage parameter ω under tension.

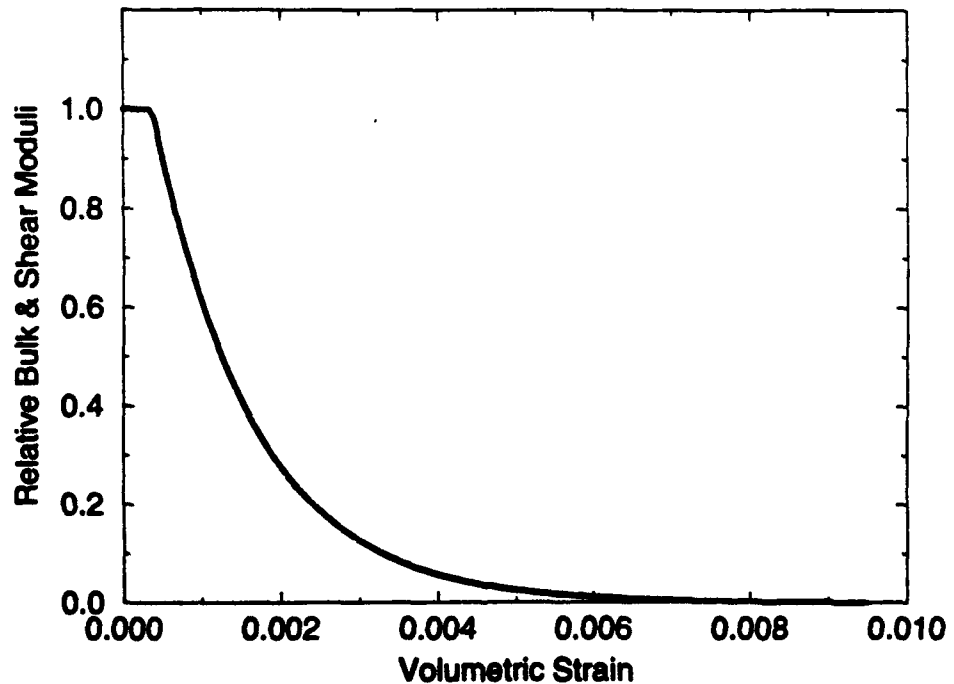


Figure 12 (b) The relative bulk and shear moduli decrease as volumetric strain increases

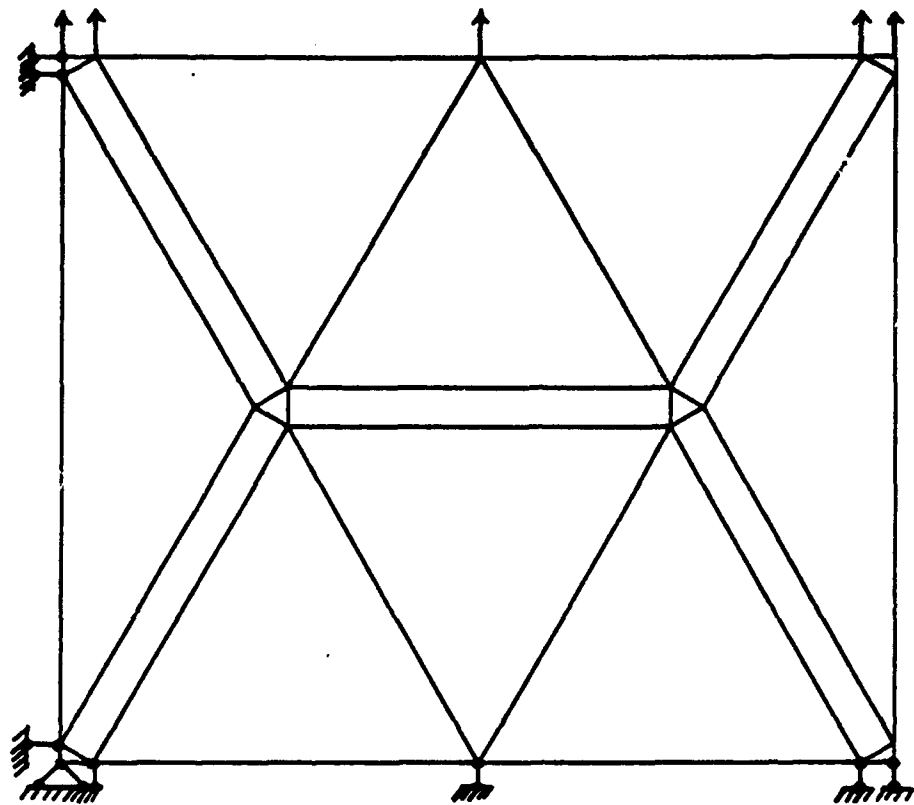


Figure 13 The finite element mesh and the boundary conditions

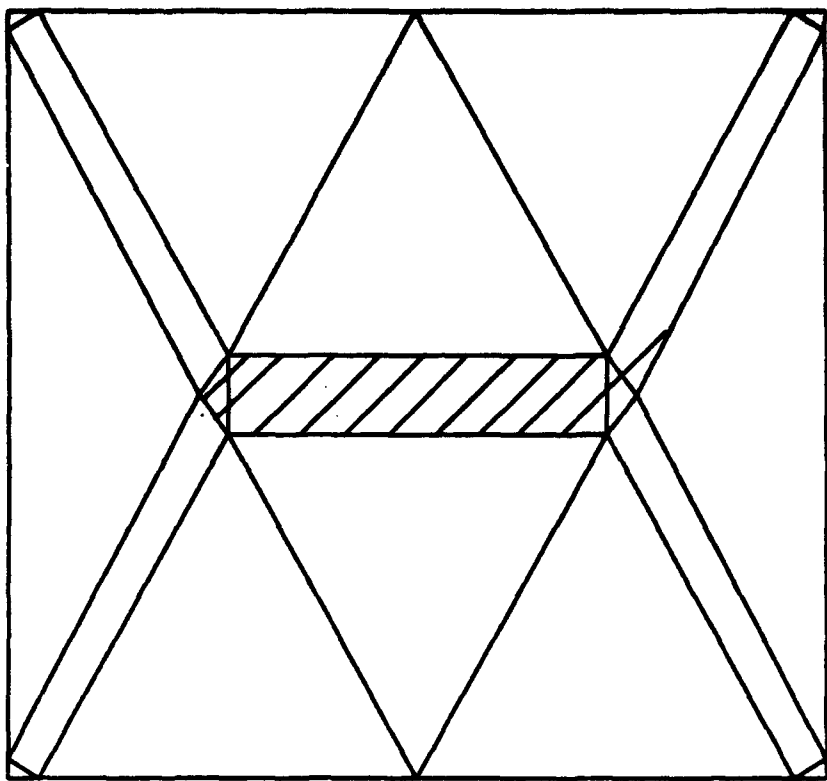


Figure 14 (a) The deformed mesh at the 20th loading step

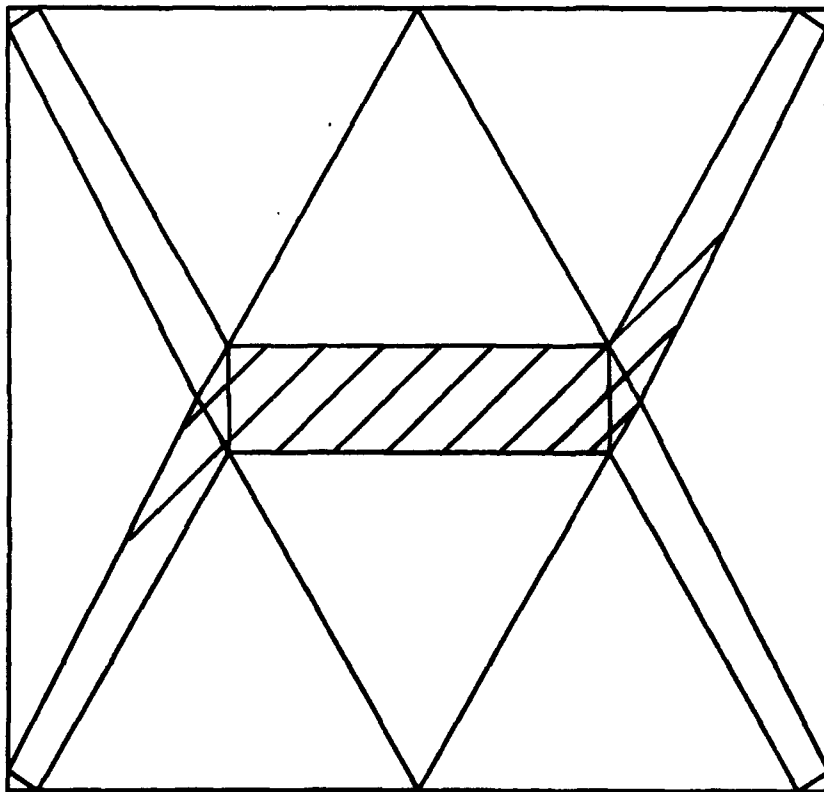
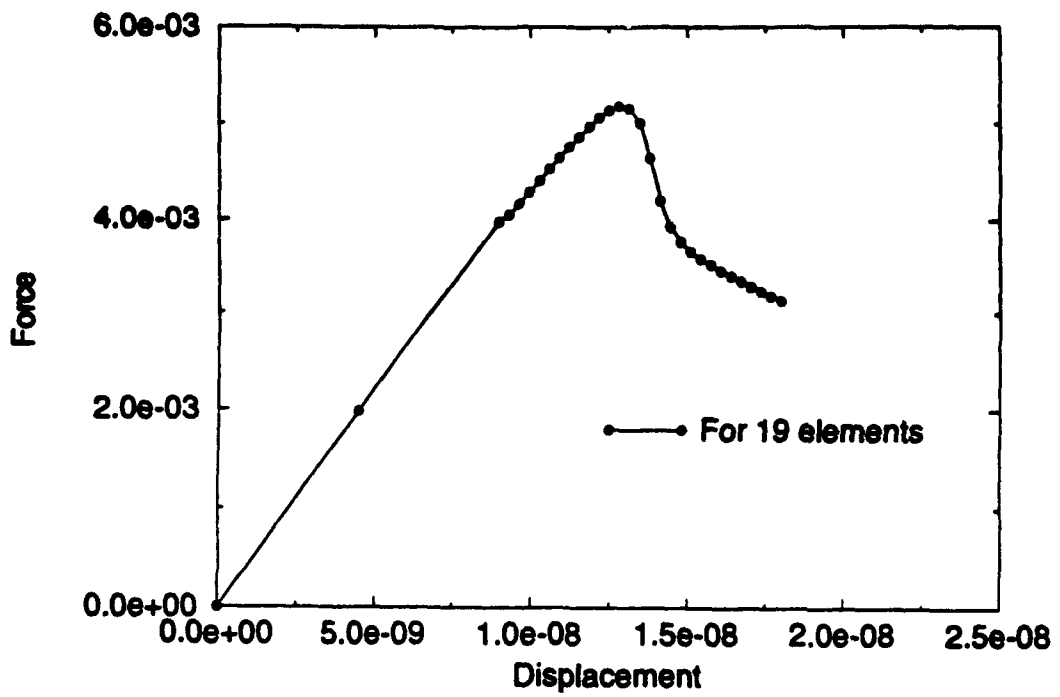


Figure 14 (b) The deformed mesh at the 30th loading step



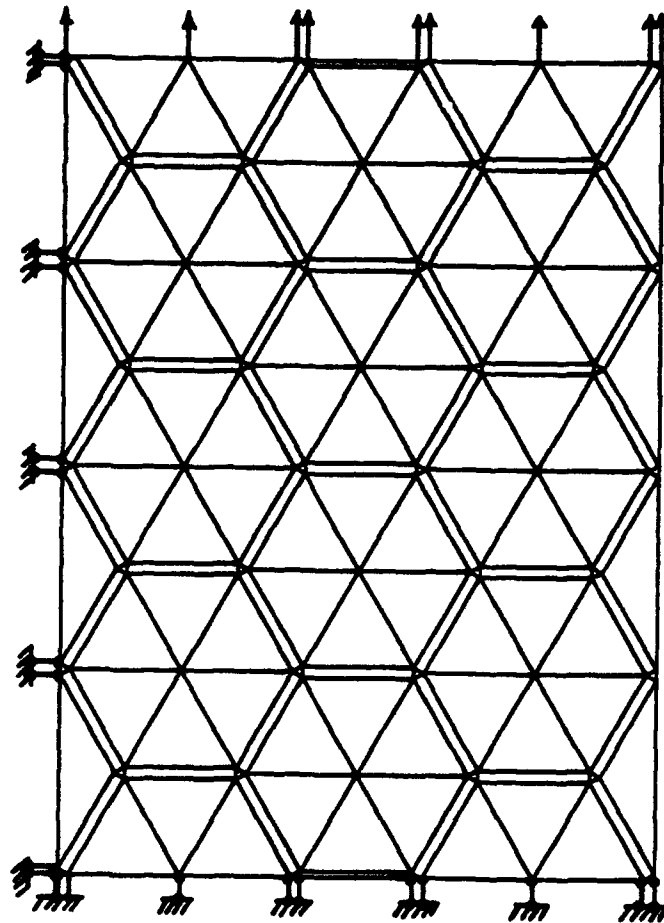


Figure 15 (a) The finite element mesh and boundary conditions

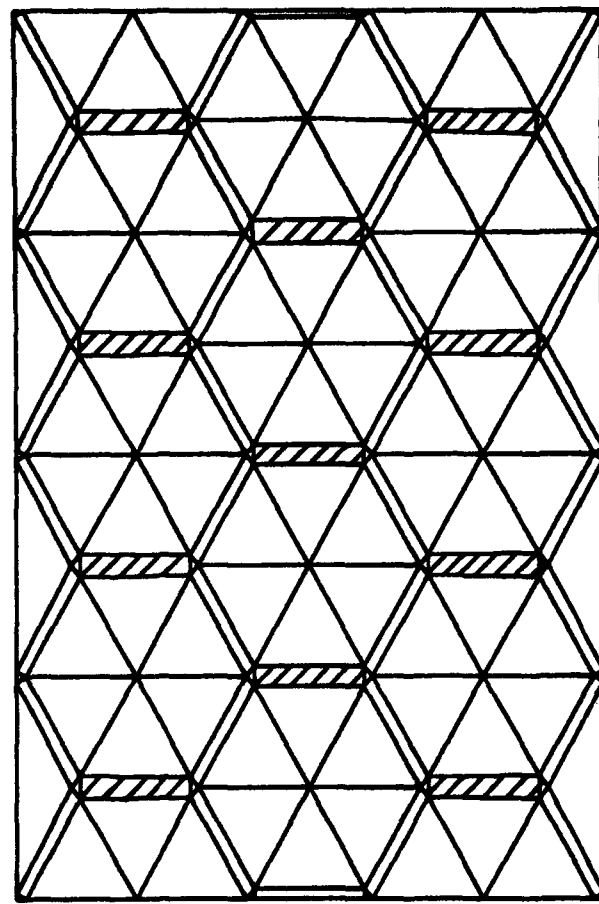


Figure 15 (b) The deformed mesh at the 23rd loading step

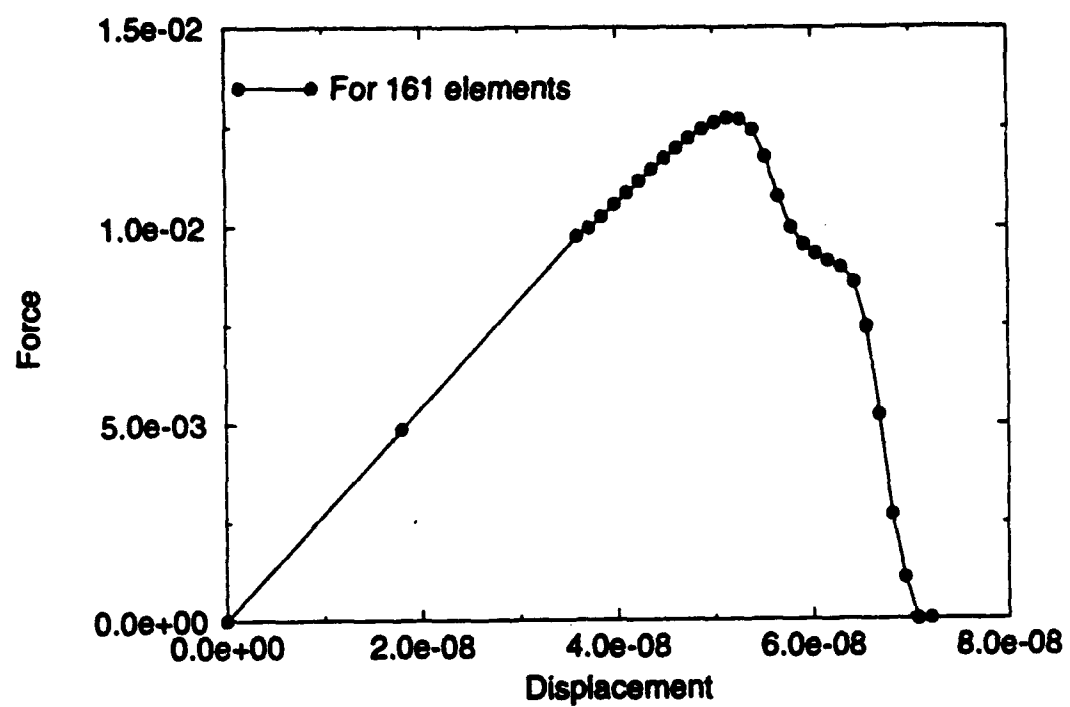
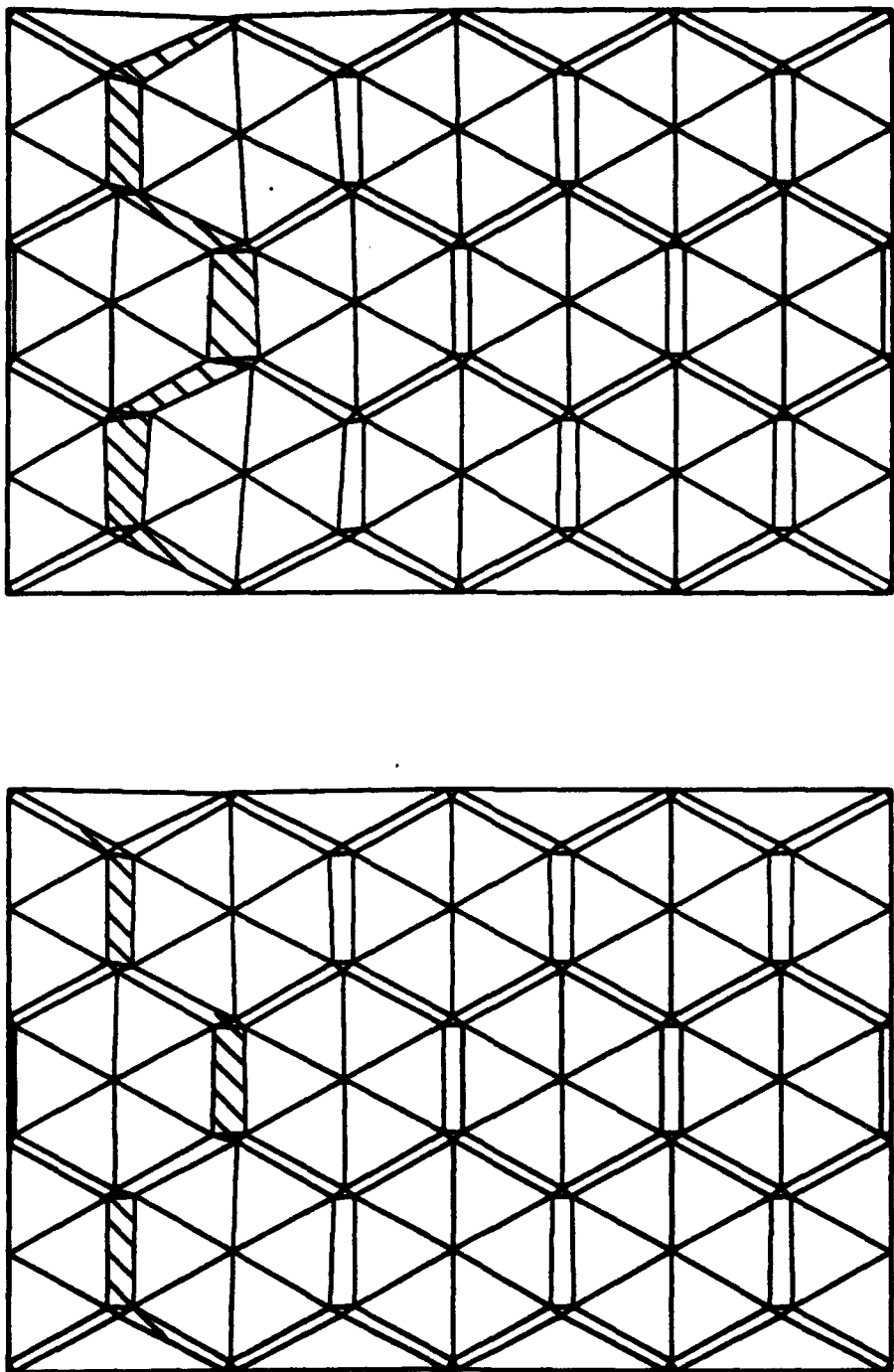


Figure 15 (c) The displacement and the total corresponding nodal force curve

Figure 16 (a) The deformed mesh at the 25th loading step; (b) the deformed mesh at the 26th loading step



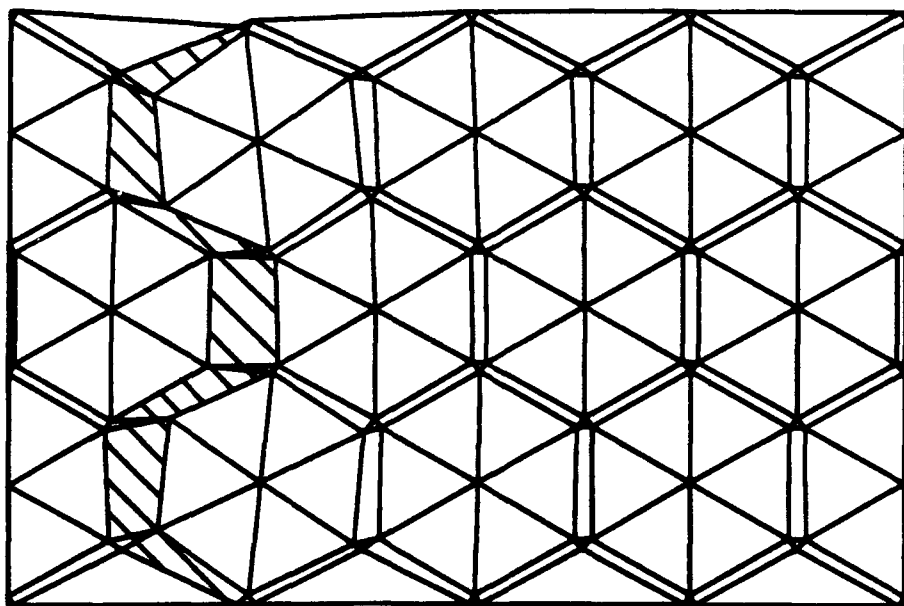
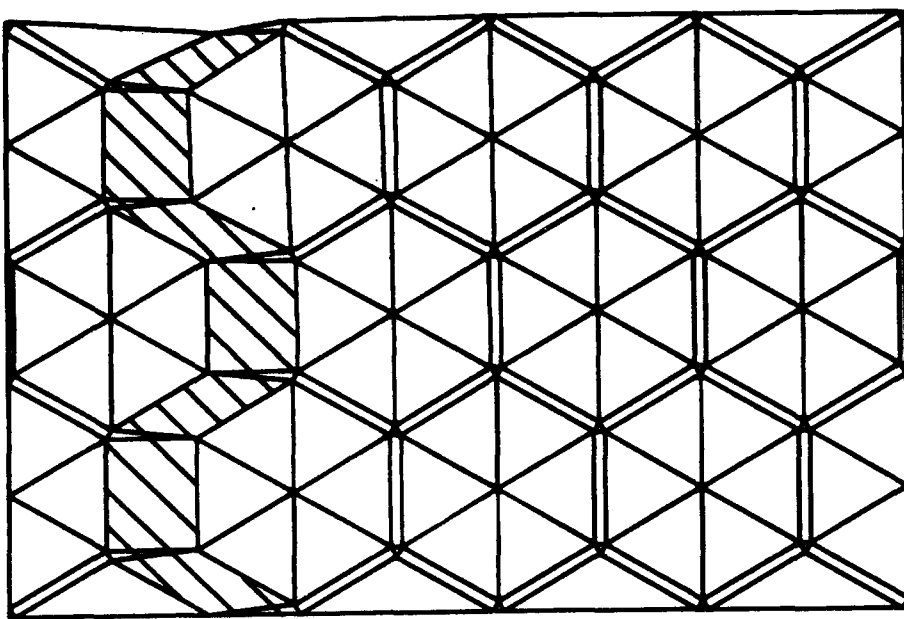


Figure 16 (c) The deformed mesh at the 27th loading step; (d) The deformed mesh at the 29th loading step

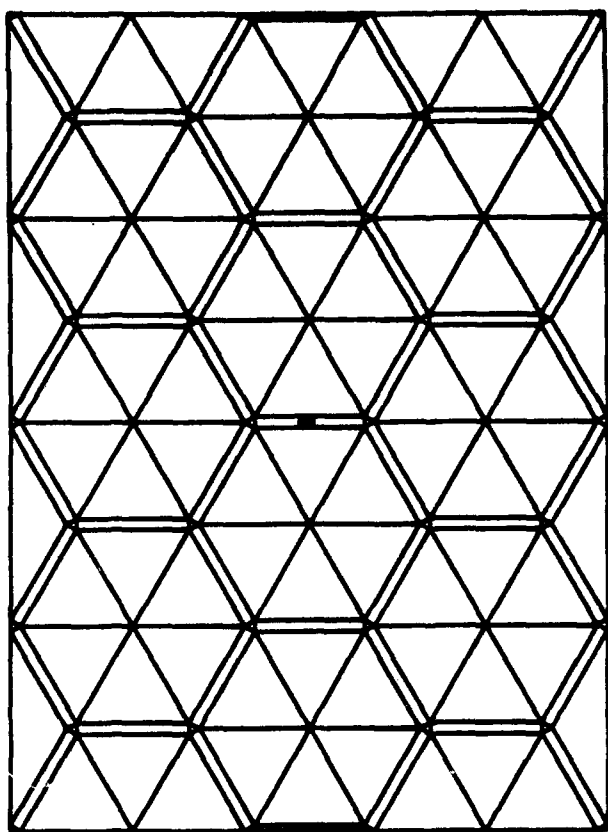


Figure 17 (a) The finite element mesh with the microcrack (marked element)

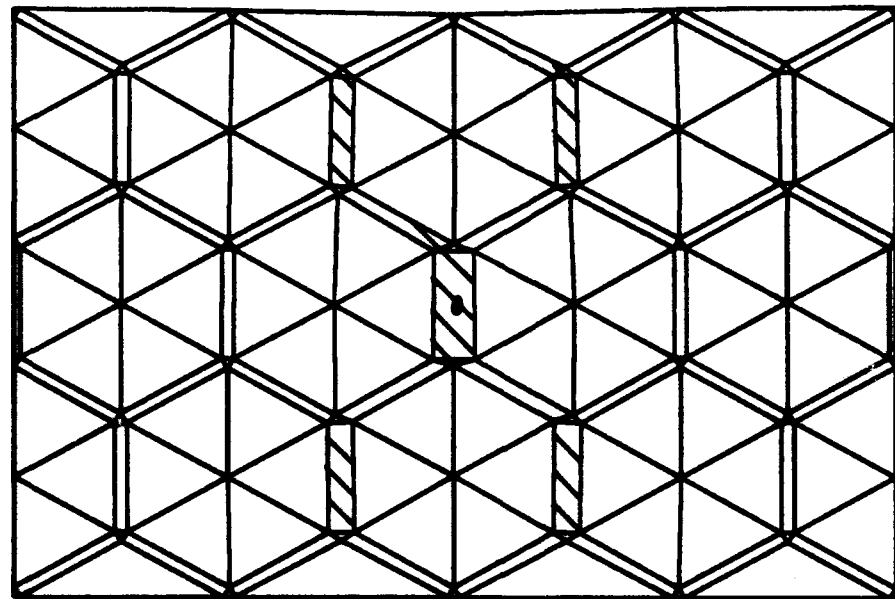
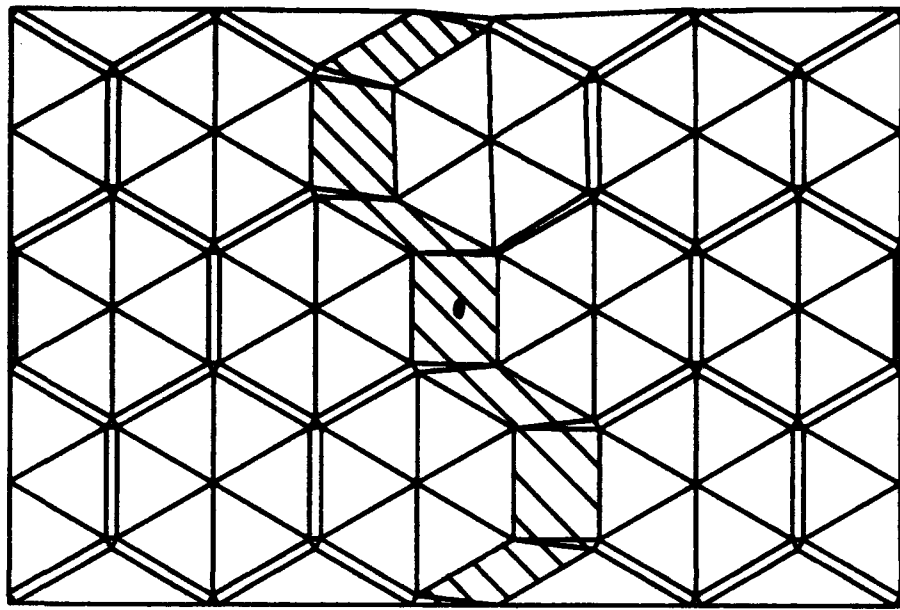


Figure 17 (b) The deformed mesh at the 20th loading step; (c) The deformed mesh at the 29th loading step

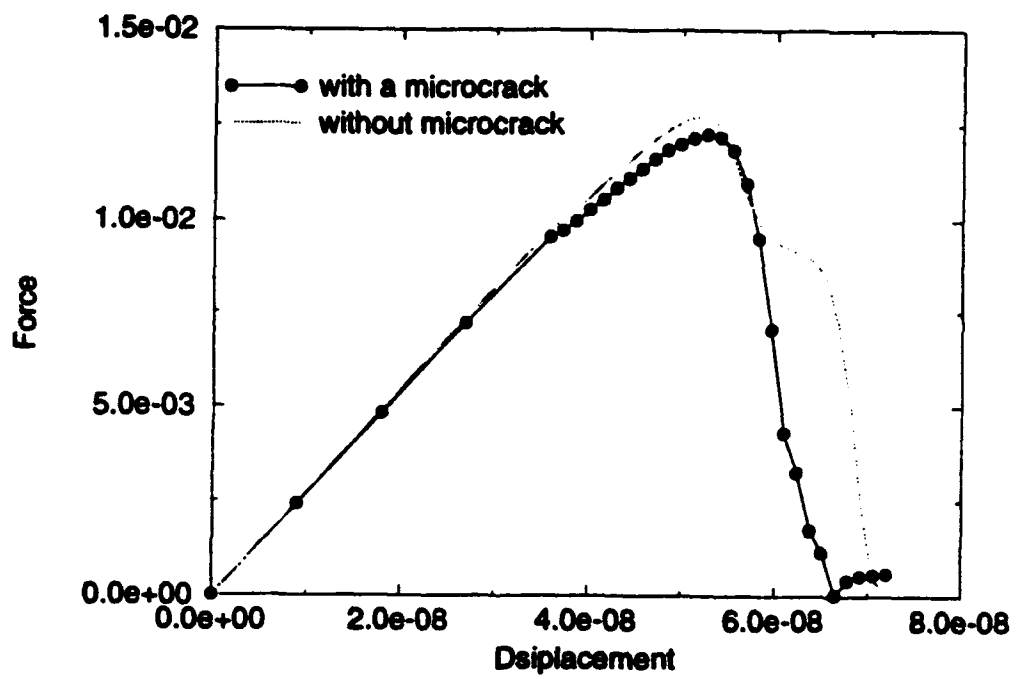


Figure 17 (d) The displacement and the total corresponding nodal force curve

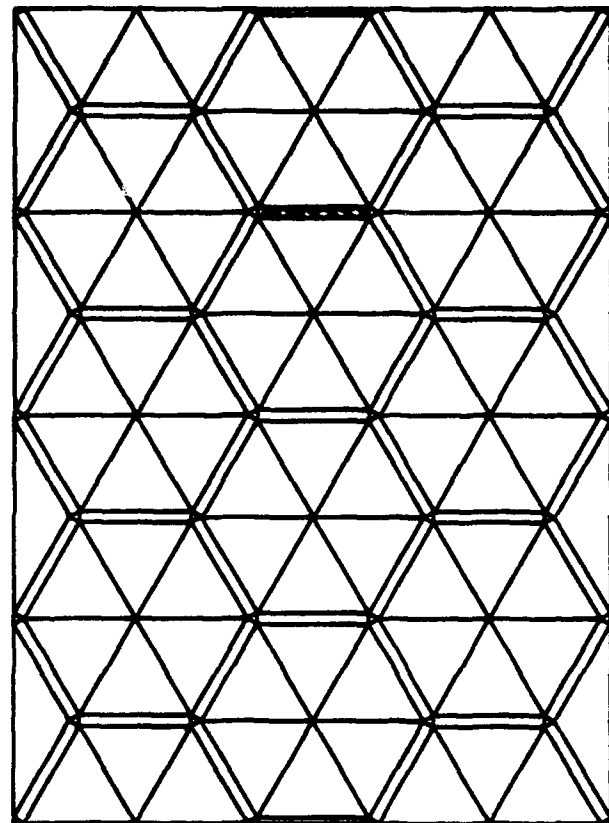


Figure 18 (a) The finite element mesh with the inclusion (marked element)

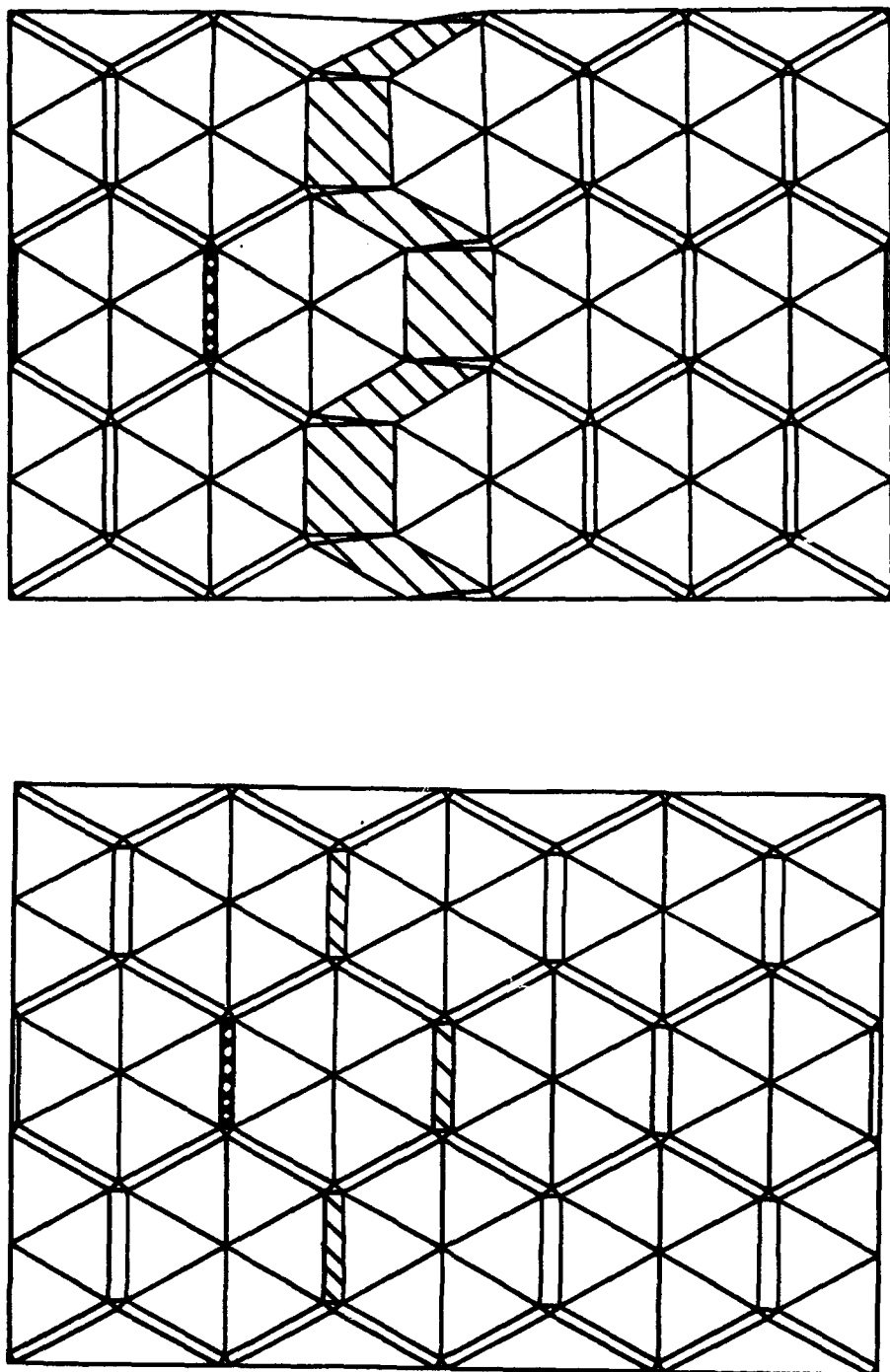


Figure 18 (b) The deformed mesh at the 20th loading step; (c) The deformed mesh at the 29th loading step

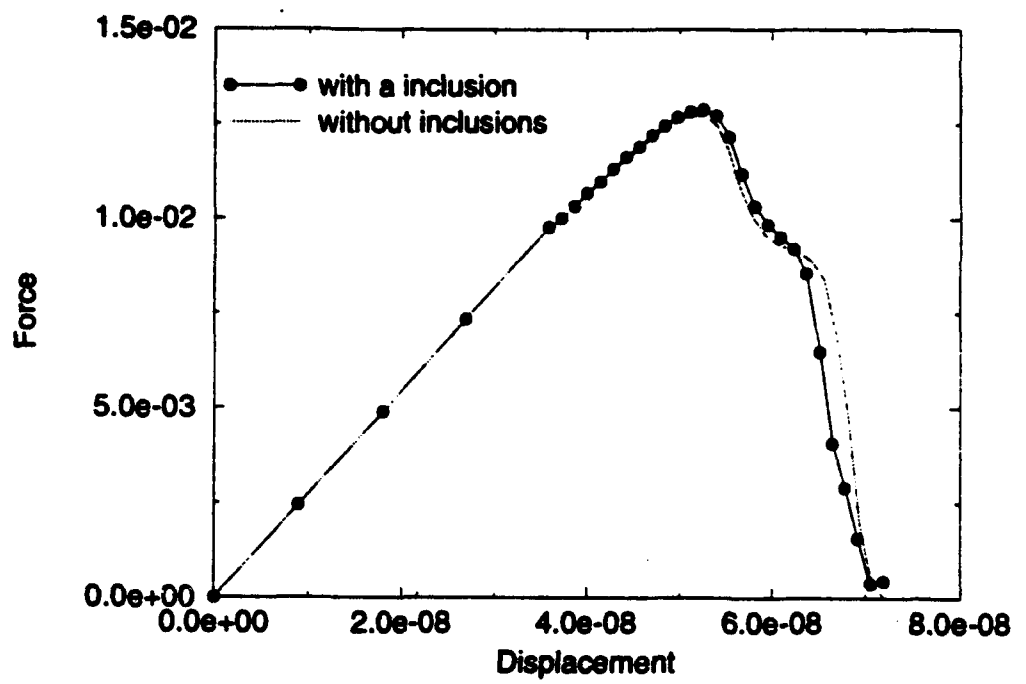


Figure 18 (d) The displacement and the total corresponding nodal force curve

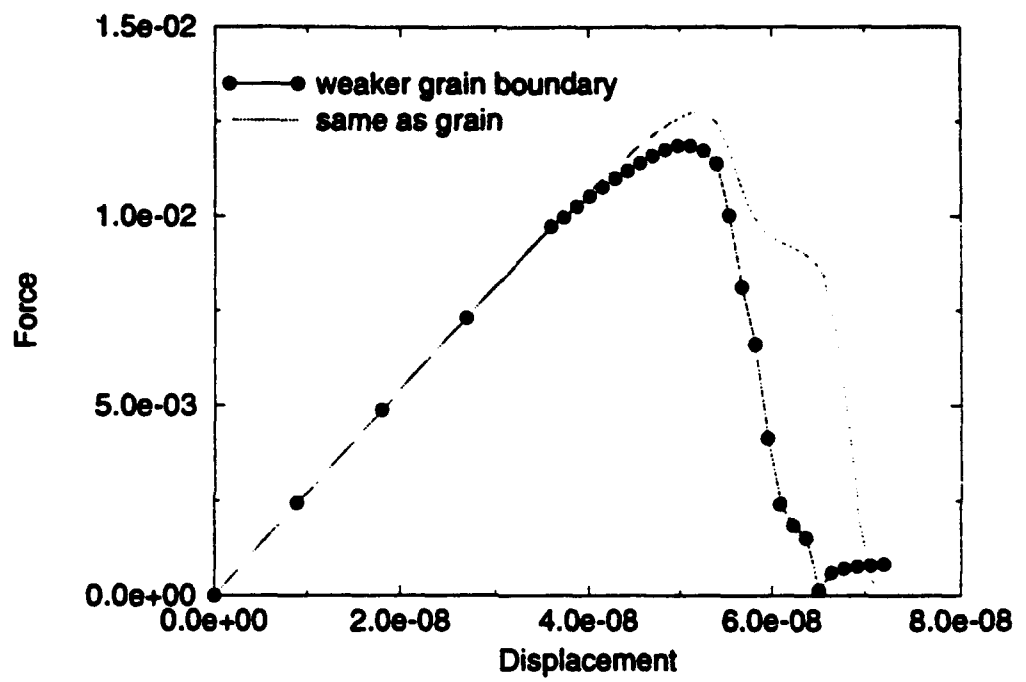


Figure 19 The displacement and the total corresponding nodal force curve

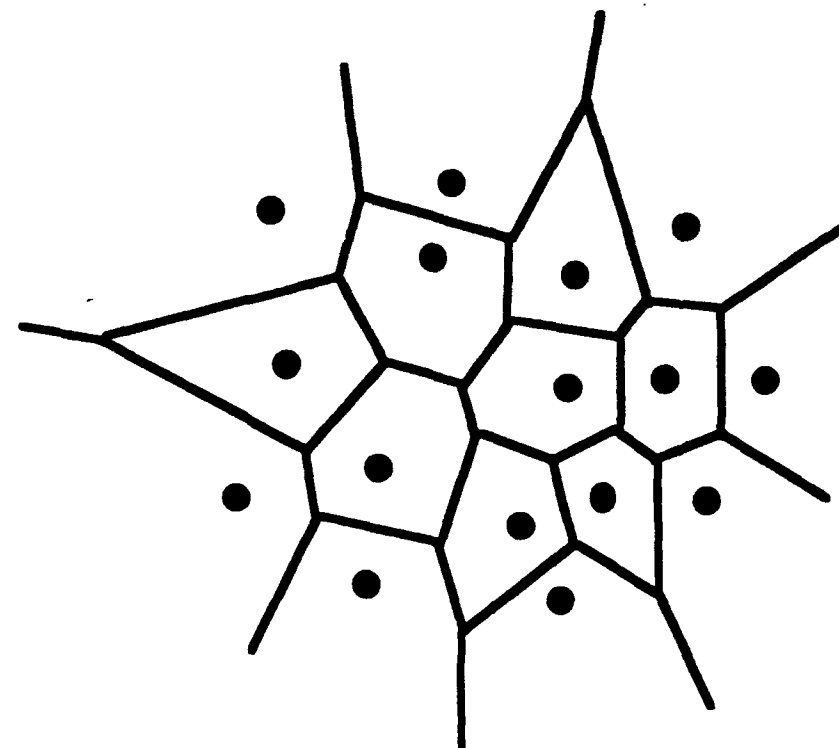


Figure 20 (a) The nearest-neighbor rule in the Voronoi diagram (after Preparata, 1985)

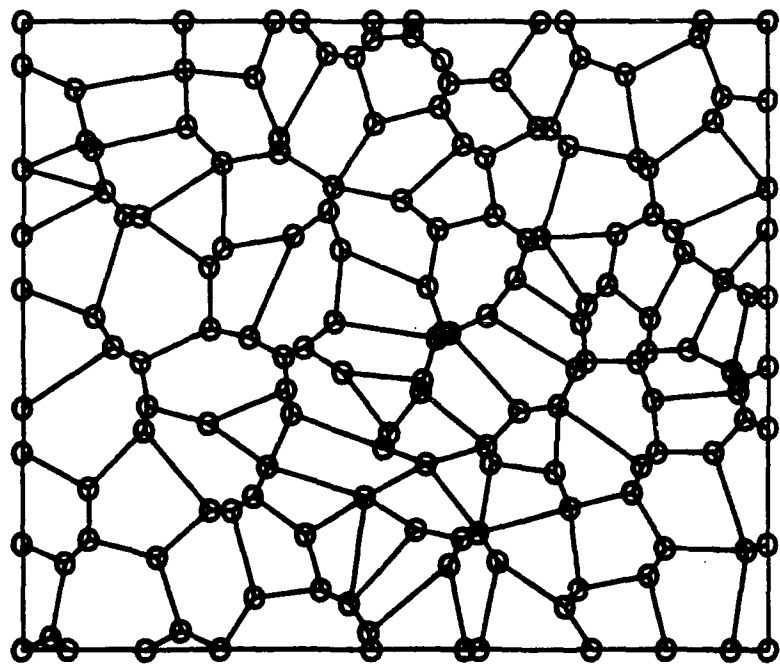


Figure 20 (b) The Voronoi diagram (displayed by COMET)

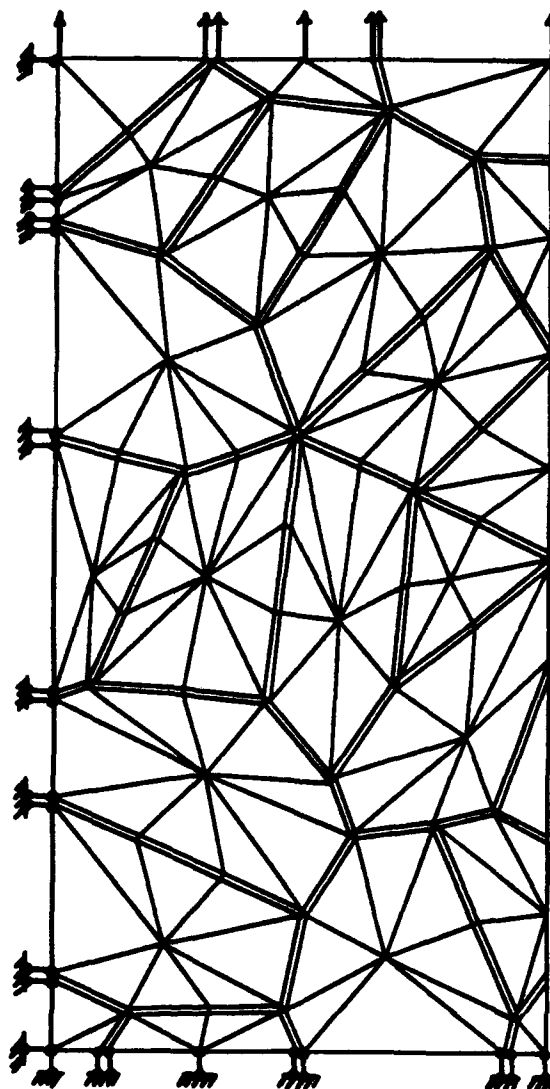


Figure 21 The finite element mesh (based on the Voronoi diagram) and boundary conditions

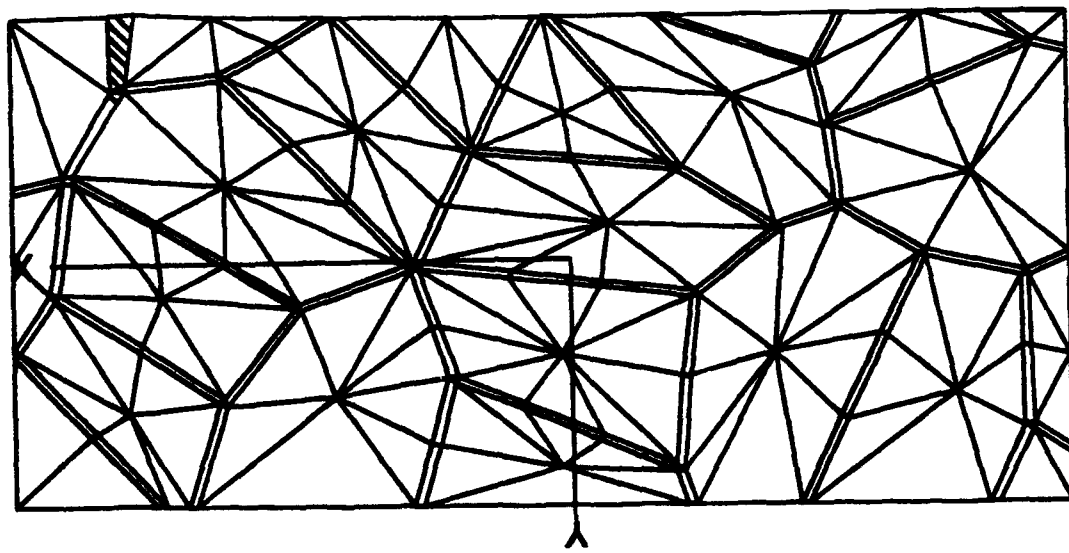
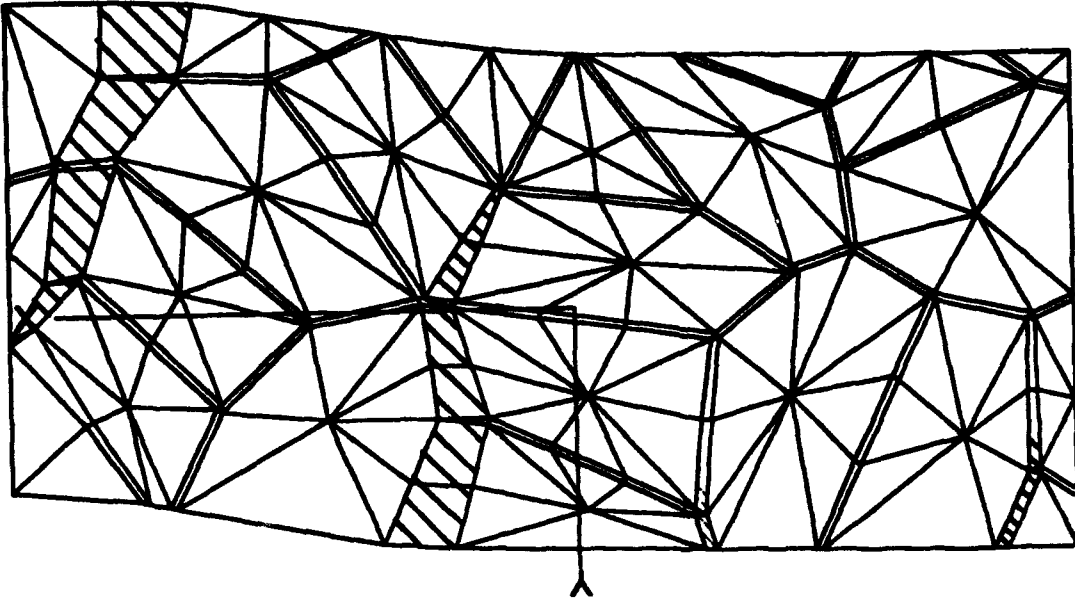


Figure 22 (a) The deformed mesh at the 12th loading step; (b) the deformed mesh at 16th loading step

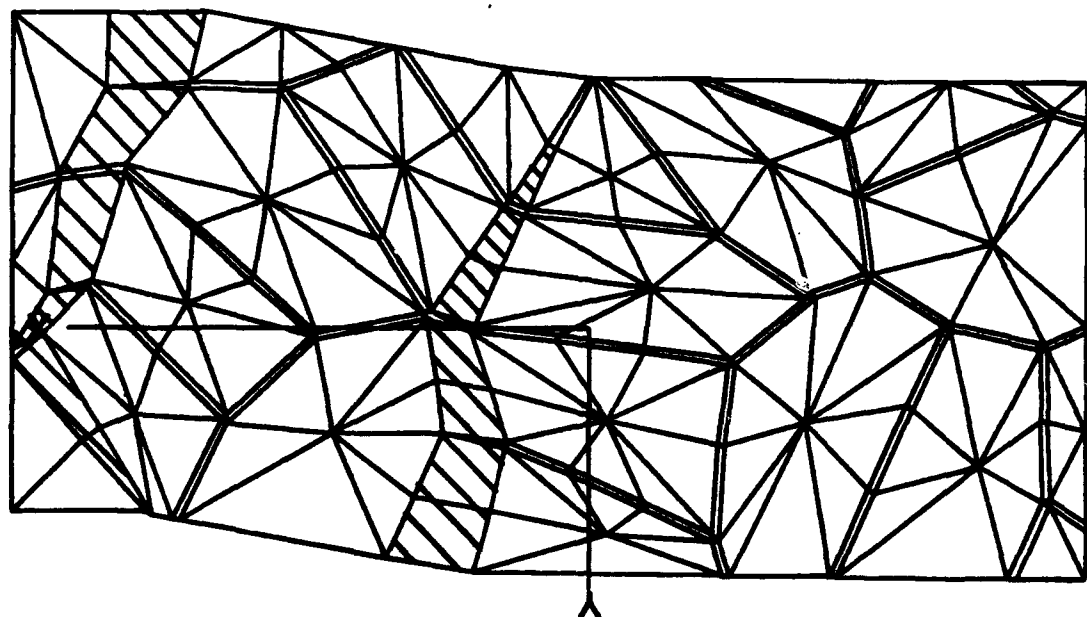
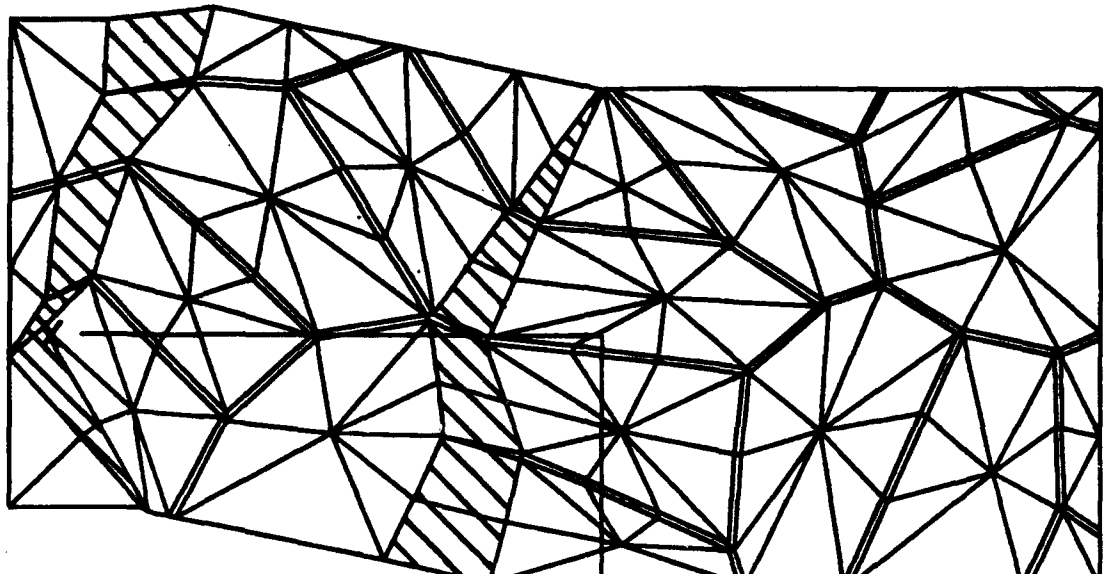


Figure 22 (c) The deformed mesh at the 22nd loading step; (d) the deformed mesh at the 30th loading step

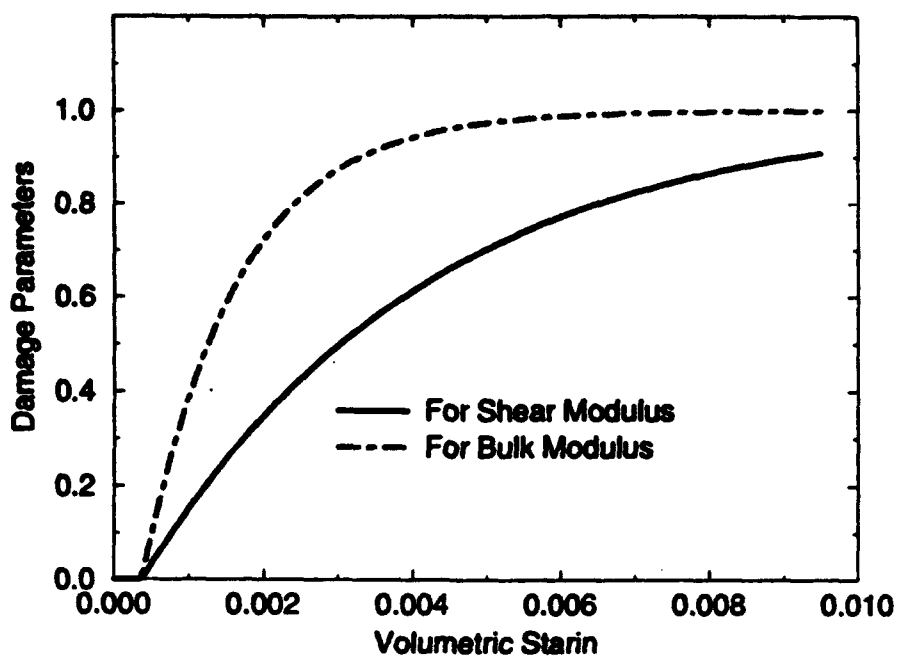


Figure 23 (a) The proposed evolution of damage parameter ω_1 and ω_2 under tension.

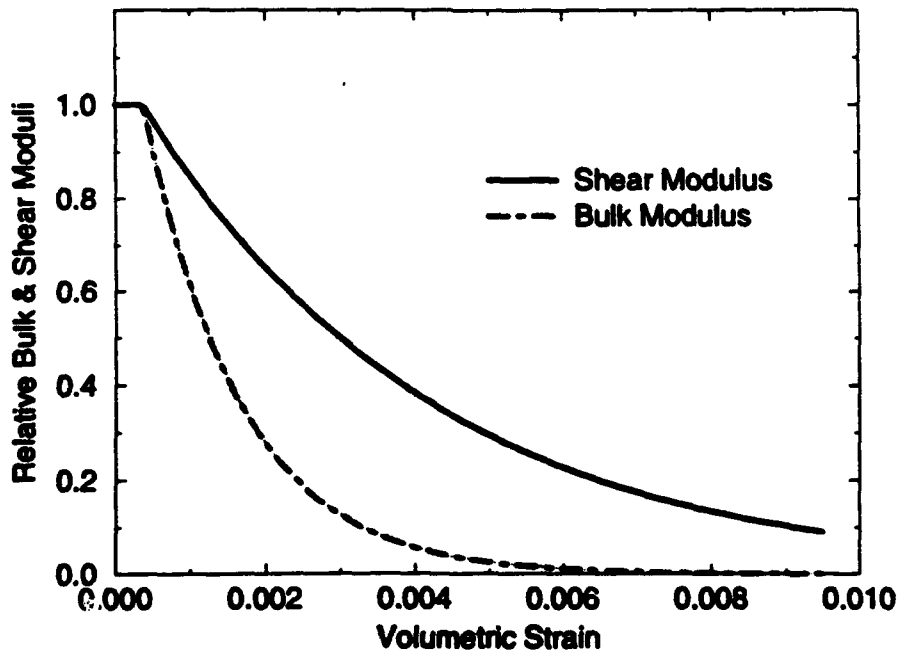


Figure 23 (b) The relative bulk and shear moduli decrease at different rate as volumetric strain increases

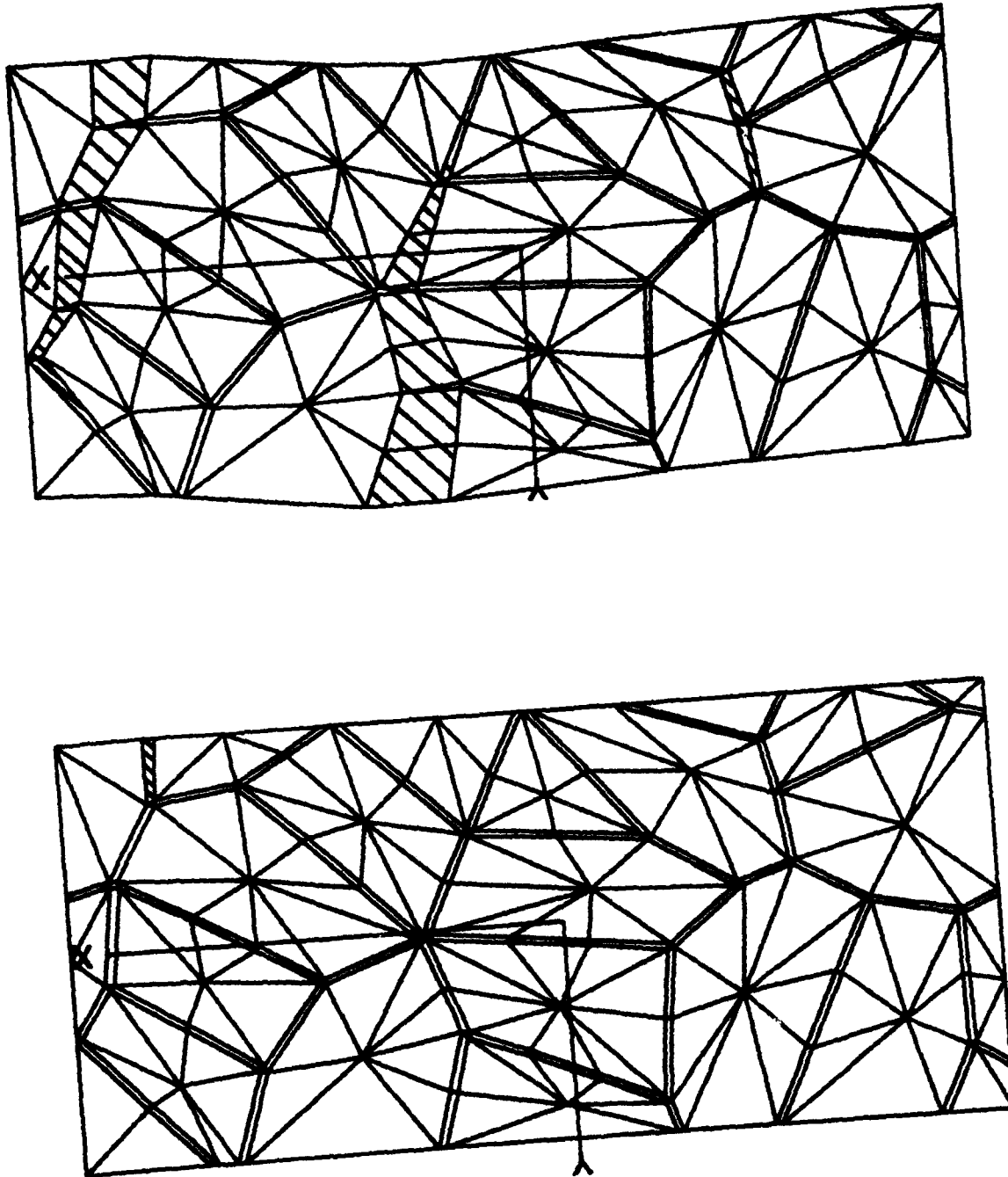


Figure 24 (a) The deformed mesh at the 16th loading step; (b) the deformed mesh at the 20th loading step

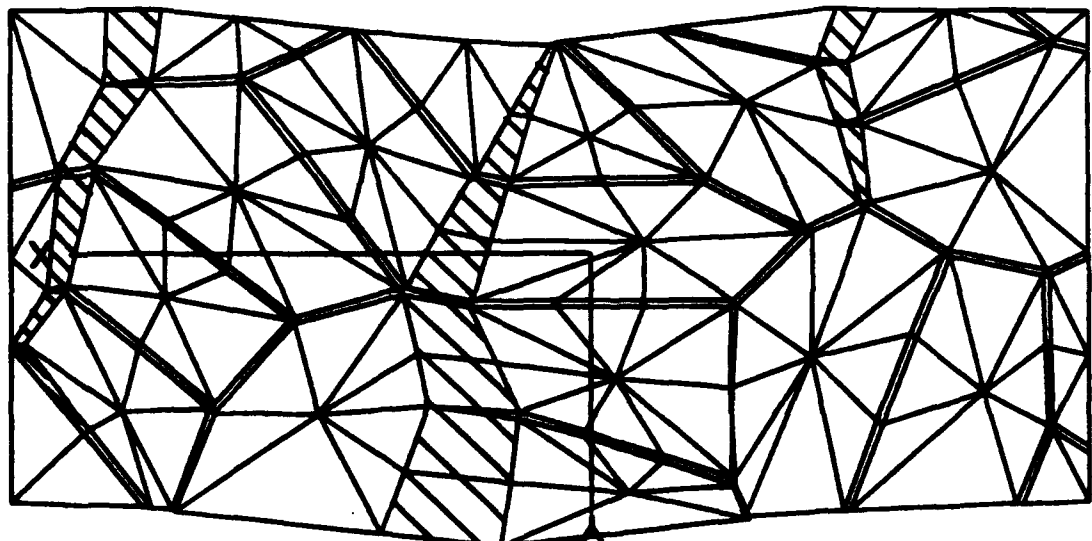
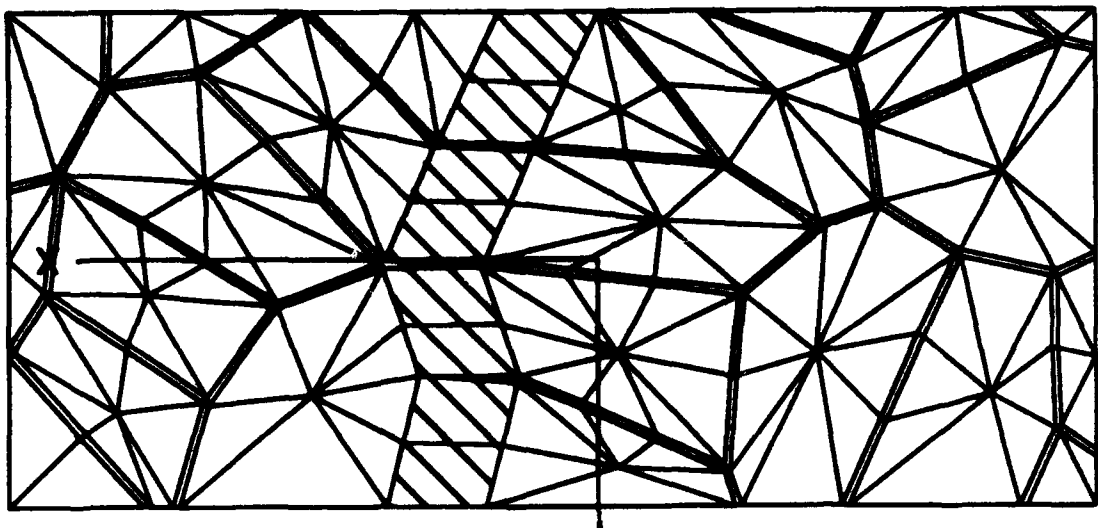


Figure 24 (c) The deformed mesh at the 25th loading step; (d) the deformed mesh at the 30th loading step

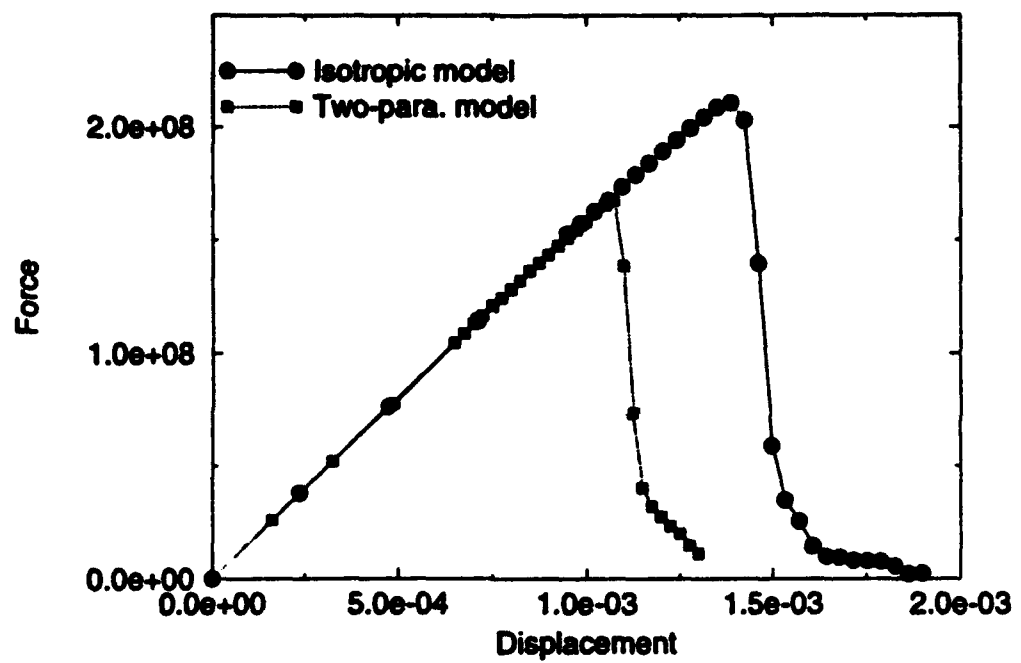


Figure 25 The displacement and the total corresponding nodal force curves

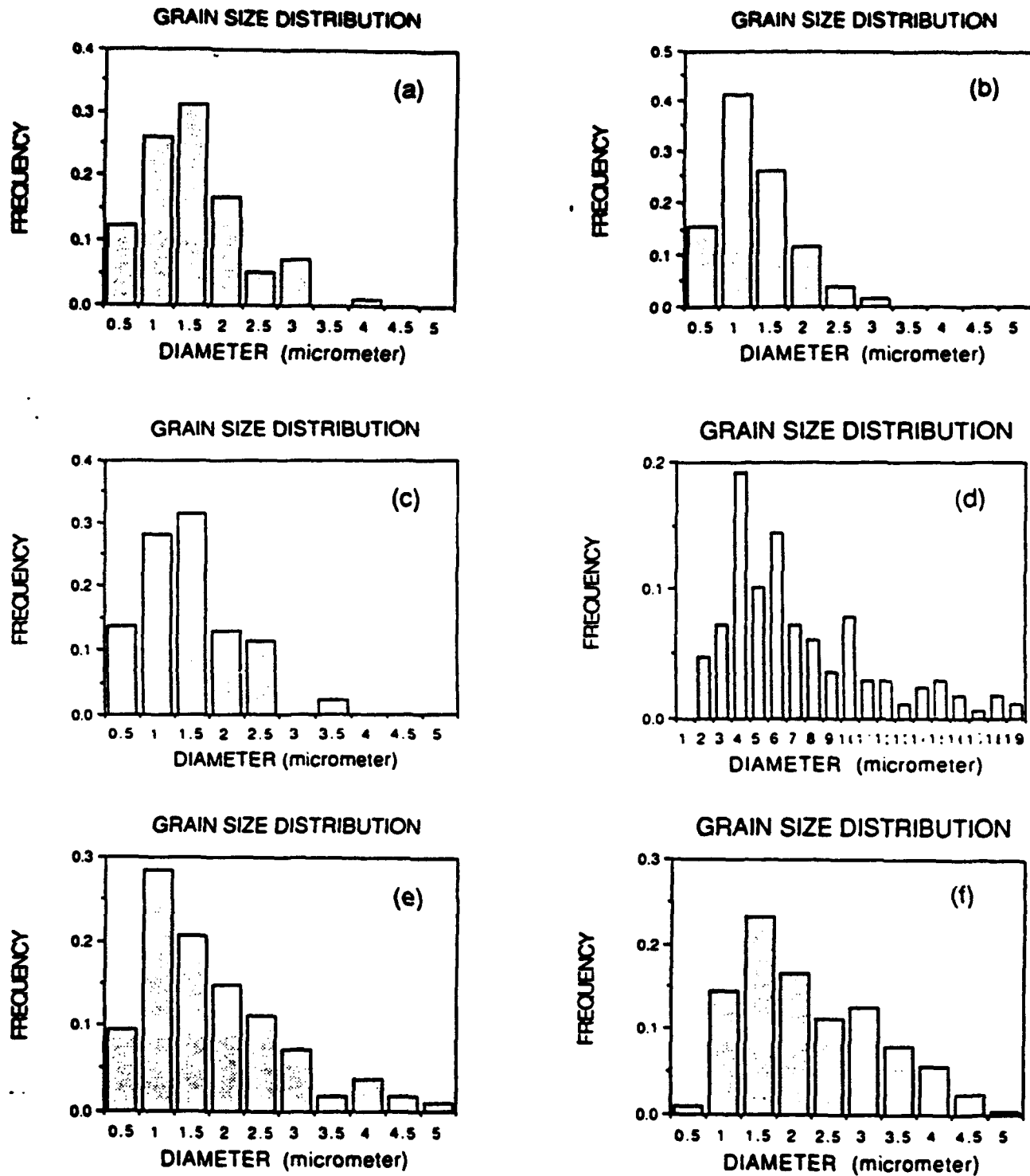
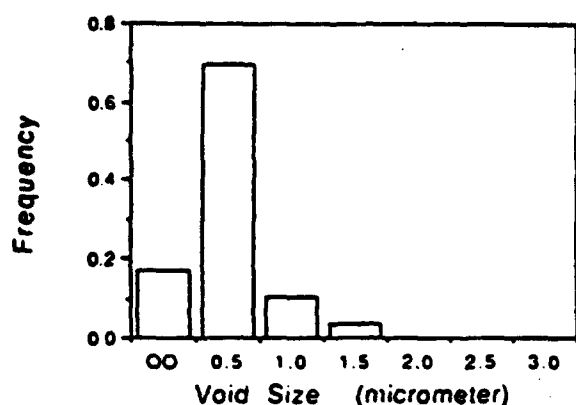
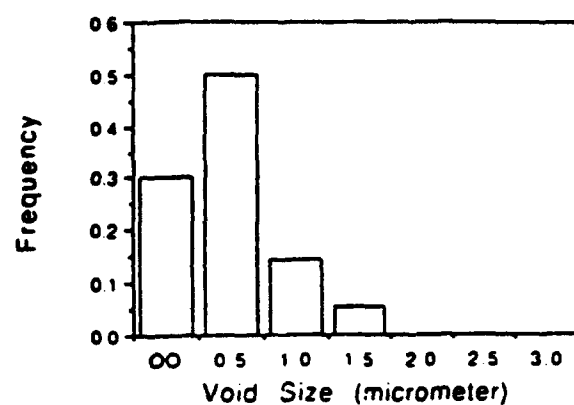


Figure 26 The grain size distribution using different sintering techniques:

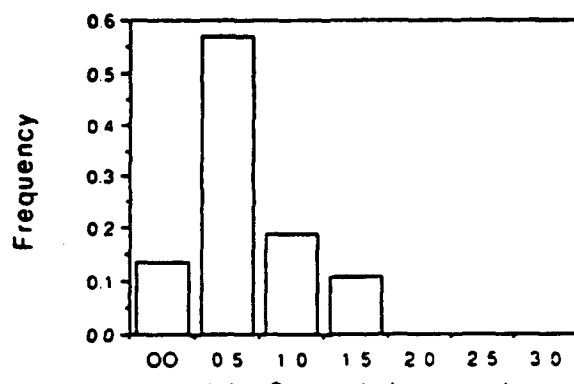
- (a) Normal sintering.
- (b) Fast sintering.
- (c) Long time sintering.
- (d) High temperature sintering.
- (e) Two stage sintering.
- (f) MgO-doped Al₂O₃ sintering.



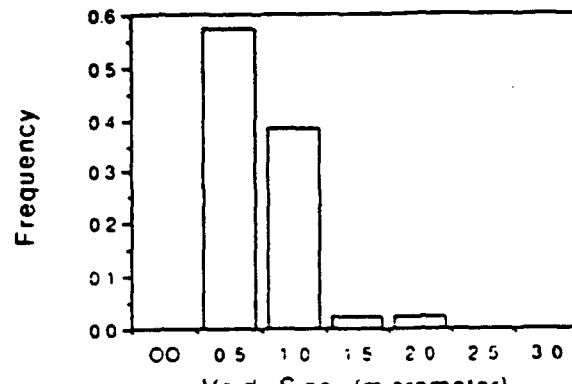
(a)



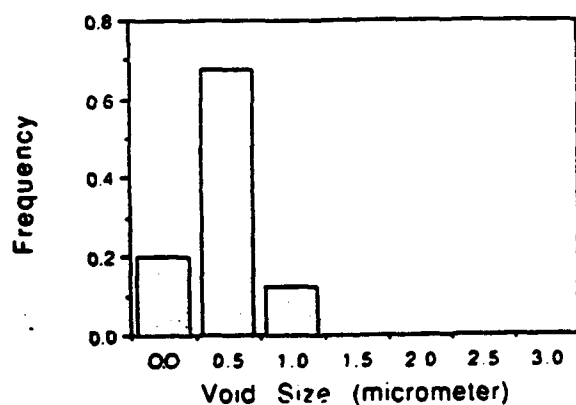
(b)



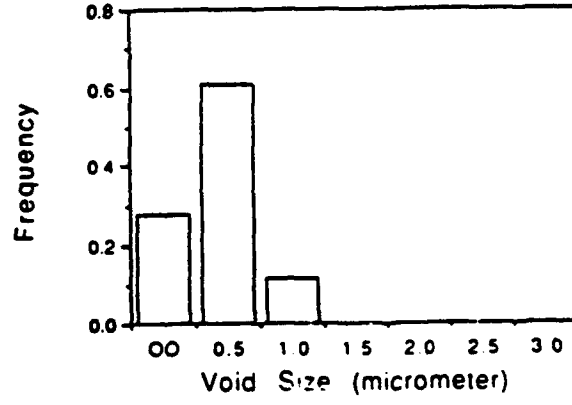
(c)



(d)



(e)



(f)

Figure 27 The void size distribution using different sintering techniques:

(a) Normal sintering,	(b) Fast sintering,
(c) Long time sintering,	(d) High temperature sintering,
(e) Two stage sintering,	(f) MgO-doped Al ₂ O ₃ sintering.

Appendix 1

The processing and properties of alumina

An alumina bar measuring 1.15 in. X 1.15 in. X 1 ft. was purchased from the Coors Technical Ceramics Co. Alumina's relative density is 99.5%.

The aluminum oxide (or alumina) is prepared by hot-pressing fine powder (nominal particle size 0.5 mm), without additives, at 1650°C for 3 hours at 35 MPa under a vacuum. The pressed material is nonporous (> 99.9% density), and the final microstructure of alumina is equiaxed with different grain sizes from 5 to 50mm, which depends on the sintering temperature, time, and pressure. The specimens are ground to the desired thickness and the prospective viewing surface is polished with diamond paste.

The properties of the alumina bar are listed below (provided by Coors Technical Ceramics Co.):

<u>Properties</u>	<u>AD-99.5 (99.5% Al₂O₃)</u>	
Density	3.88	(g/cm ³)
Surface finish	0.9	(mm)
Grain size range	5 - 50	(mm)
Water absorption	0	
Gas perm.	0	
Color	Ivory	
Flexural strength		
(MOR)	20°C	379 MPa
Elastic modulus	20°C	372 GPa
Shear modulus	20°C	152 GPa
Poisson's ratio	20°C	0.22
Compressive strength	20°C	2620 MPa
Hardness		14.1 GPa
Tensile Strength	25°C	262 MPa
Fracture Toughness		4.5 MPa m ^{1/2}

Appendix 2 Dynamic Relaxation

Nonlinear structural analyses include materially nonlinear problems such as nonlinear constitutive equations with small deformations, geometrically nonlinear problems normally associated with buckling or a combination of both types of nonlinearities (Chen, and Schreyer, 1990). The nonlinear analysis in the finite element method can be expressed as

$$[K] \{U\} = \{F\} \quad (1)$$

where $[K]$ is the structure stiffness matrix,
 $\{U\}$ is the vector of nodal degree of freedom,
 $\{F\}$ is the vector of nodal loads.

$[K]$ and $\{F\}$ are regarded as dependent on $\{U\}$. The schemes for nonlinear problems are based on step-by-step load incrementation and an iteration procedure to correct the linearization.

The equation governing the structural behavior is considered to be in the form

$$\{F(U)\}_{int} = \{F\}_{ext} \quad (2)$$

where $\{F(U)\}_{int}$ is the vector of internal nodal force, which depends on $\{U\}$, and $\{F\}_{ext}$ is the vector of the external (applied) nodal force.

Equation (2) is another expression of Equation (1), i.e., $\{F(U)\}_{int} = [K]\{U\}$, and $\{F\}_{ext} = \{F\}$.

Since the DR method is based on structural dynamic response, the governing equation is the appropriate equation for developing the DR method. For the n^{th} time increment the equation is given by

$$[M] (\ddot{U})^n + [C] (\dot{U})^n + [K] \{U\}^n = \{F(t^n)\}_{ext} \quad (3)$$

i.e.,

$$[M] (\ddot{U})^n + [C] (\dot{U})^n + \{F(U^n)\}_{int} = \{F(t^n)\}_{ext} \quad (4)$$

where $[M]$ is the mass matrix, C is the damping matrix, t is time, n indicates the n^{th} time increment, a superimposed dot indicates a temporal derivative, and other terms are as previously defined. To obtain the DR algorithm, the following central difference expressions are used for the temporal derivatives:

$$\begin{aligned} \dot{U}^{n-1/2} &= (-\{U\}^{n-1} + \{U\}^n) / h \\ \dot{U}^n &= (-\dot{U}^{n-1/2} + \dot{U}^{n+1/2}) / h \end{aligned} \quad (5)$$

where h is a fixed time increment. The expression for $(\dot{U})^n$ is obtained by the average value:

$$(\dot{U})^n = 0.5 (\dot{U})^{n-1/2} + (\dot{U})^{n+1/2} \quad (6)$$

Substituting Eq. (5) and (6) into (4) gives the pair of equations used to obtain next time velocity and displacement as

$$\begin{aligned} (\dot{U})^{n+1/2} &= \frac{([M]/h-0.5[C])}{([M]/h+0.5[C])} (\dot{U})^{n-1/2} + \frac{(\{F\}_{ext}^n - \{F\}_{int}^n)}{([M]/h+0.5[C])}, \\ (U)^{n+1} &= (U)^n + h (\dot{U})^{n+1/2} \end{aligned} \quad (7)$$

where $\{F\}_{ext}^n = \{F(t^n)\}_{ext}$ and $\{F\}_{int}^n = \{F(U^n)\}_{int}$.

To preserve the explicit form of Eq. (7), $[M]$ must be diagonal and to obtain the form used for DR, $[C]$ has the form

$$[C] = c [M] \quad (8)$$

Substituting Eq. (8) into (7) gives

$$\begin{aligned} (\dot{U})^{n+1/2} &= \frac{(2-ch)}{(2+ch)} (\dot{U})^{n-1/2} + 2h[M]^{-1} (\{F\}_{ext}^n - \{F\}_{int}^n) / (2+ch), \\ (U)^{n+1} &= (U)^n + h (\dot{U})^{n+1/2} \end{aligned} \quad (9)$$

where $[M]^{-1}$ is the inverse of $[M]$. Since $[M]$ is diagonal, Eq.(9) is algebraic. That is, each solution vector component may be computed individually from

$$\begin{aligned} \dot{U}_i^{n+1/2} &= \frac{(2-ch)}{(2+ch)} \dot{U}_i^{n-1/2} + 2h (\{F_{ext i}^n - F_{int i}^n\}) / [m_{ii} (2+ch)], \\ U_i^{n+1} &= U_i^n + h \dot{U}_i^{n+1/2} \end{aligned} \quad (10)$$

where the subscript i indicates the i^{th} vector component and m_{ii} is the i^{th} diagonal element of $[M]$.

In order to start the integration, the velocity at $t^{-1/2}$, and t^0 must be known. For the DR algorithm, the starting conditions are of the form

$$(U)^0 \neq 0; \quad (\dot{U})^0 = 0 \quad (11)$$

Using Eq. (6) and the second of Eq. (11) gives

$$(\dot{U})^{-1/2} = -(\dot{U})^{1/2} \quad (12)$$

For the first time increment, the first expression of Eq. (9) becomes

$$(\dot{U})^{1/2} = h [M]^{-1} ((F)_{ext}^0 - (F)_{int}^0) / 2 \quad (13)$$

The central difference time integrator is therefore given by

$$\begin{aligned} \text{if } n = 0: \quad & (\dot{U})^{1/2} = h [M]^{-1} ((F)_{ext}^0 - (F)_{int}^0) / 2, \\ \text{if } n \neq 0: \quad & (\dot{U})^{n+1/2} = \frac{(2-ch)}{(2+ch)} (\dot{U})^{n-1/2} + 2h[M]^{-1} ((F)_{ext}^n - (F)_{int}^n) / (2 + ch), \\ \text{for all } n: \quad & (U)^{n+1} = (U)^n + h (\dot{U})^{n+1/2} \end{aligned} \quad (14)$$

To obtain the static solution from the transient response equation, the damping coefficient, c , the time increment, h , and the mass matrix, $[M]$, are selected to obtain the fastest convergence. Note that only $(F)_{ext}$ and $(F)_{int}$ must represent the physical problem, and c and $[M]$ need not represent the physical structure. Also, h is dependent on $[M]$ (Underwood, 1983).

Formally, the DR algorithm may be written as:

- (a) choose v ($v = ch$) and $[M]$; $(U)^0$ given; $(\dot{U})^0 = 0$,
- (b) residual $(r)^n = (F)_{ext}^n - (F)_{int}^n$,
- (c) if $(r)^n = \{0\}$ stop, otherwise continue,
- (d) $n = 0: \quad (\dot{U})^{1/2} = h [M]^{-1} (r)^0 / 2,$
- $n \neq 0: \quad (\dot{U})^{n+1/2} = \frac{(2-v)}{(2+v)} (\dot{U})^{n-1/2} + 2h[M]^{-1} (r)^0 / (2 + v),$
- (e) $(U)^{n+1} = (U)^n + h (\dot{U})^{n+1/2}$
- (f) $n = n + 1$; return to (b).

The difference between the central difference time integrator and the DR method is that v and $[M]$ are fictitious values chosen so that the static solution $(r) = \{0\}$ is obtained in a minimum number of steps. Also h is a pseudo-time increment which must be chosen to ensure stability and accuracy of the iterations.

The internal nodal force $(F(U))_{int}^e$ in an element is:

$$(F(U))_{int}^e = [K]^e (U)^e$$

where $[K]^e = \int_V [B]^T [E] [B] dV$, and the superscript e defines the element.

Matrix $[B]$ relates the strain and nodal displacements:

$$[e] = [B] (U)^e$$

where $[\epsilon]$ is the total strain vector.

$$\begin{aligned}\text{So, } (\mathbf{F}(\mathbf{U}))_{\text{int}}^{\epsilon} &= \int_V [\mathbf{B}]^T [\mathbf{E}] [\mathbf{B}] dV \{ \mathbf{U} \}^{\epsilon} \\ &= \int_V [\mathbf{B}]^T [\mathbf{E}] [\mathbf{B}] \{ \mathbf{U} \}^{\epsilon} dV \\ &= \int_V [\mathbf{B}]^T [\mathbf{E}] [\epsilon] dV \\ &= \int_V [\mathbf{B}]^T [\mathbf{s}] dV\end{aligned}$$

where $[\mathbf{s}]$ is the total stress vector. In the DR method, the stiffness matrix $[\mathbf{K}]$ does not need to be formed and stored.

Appendix 3

Tension-Compression Loading Stage for FSEM

Introduction

For real-time fracture study, a closed-loop control tension-compression loading stage inside a Fast-Scanning Electron Microscope (FSEM) is required. The FSEM is basically a modified SEM with modified tools for rapid scan rates. Thus it is able to observe specimen activity at greater than 1 kHz framing rate, allowing for TV time observations. For the FSEM project, specimens of ceramic were tested in the FSEM chamber. Image scanning was performed with a digital data acquisition system, and the resulting micrographs were later examined in an observable time frame. The major drawbacks of FSEM microscopy include sacrificed depth-of-field and submicron resolution, resulting in a snowier picture than conventional SEM micrographs.

Objectives

The following list outlines the objectives of this project.

1. Assess use of pre-existing equipment and ideas
2. Achieve open-loop control of the loading stage, complete with sensor data acquisition
3. Advance the system to a closed-loop status by using a selected motion control sequence
4. Install the completed in-situ device for use inside the SEM chamber
5. Perform tests with the alumina ceramic specimen to observe effects of the work

General Principle and System Elements

General Principle

The whole experimental system is controlled by the Galil Motion Controller DMC-1010 which plugs into the PC bus. It sends designated commands to the step-motor set, which drives the worm-gear assembly and screw shaft to move the specimen platform. While the specimen is being dragged, a clip-on gage, which is held between knife edges attached to the specimen, moves simultaneously to sense the crack opening displacements. A load cell is also engaged to test the changing tension on the specimen. The data from the clip-on gage and load cell are amplified and filtered and then collected by the motion controller. In a closed-loop control test, the sample data are analyzed by the controller and an error signal is sent out to adjust the system's movement. The Visual Basic system is introduced to establish the testing data file and to paternally control the testing system. The working system is shown in Figure 3-1.

System Elements

The Galil Motion Controller DMC-1010 is designed for maximum system flexibility, and is available for one, two, three, or four axes. It can be interfaced to a variety of motors and drives including full-step, micro-stepping and servo-motor. Its main processing unit is a specialized 32-bit Motorola 68331 Series Microcomputer with 64 K RAM, 64 K EPROM and 256 bytes EEPROM. It provides interface circuitry for 8 outputs, 8 inputs and 7 analog inputs. The analog input is a 12-bit ADC with a range of ± 10 V, which is 0.488 mV/bit.

The step-motor set, which is an American Precision Industries model P261-M232, includes a drive controller and a step motor. It combines an integral power section and the bipolar chopper drive technique. This technique involves over-driving the windings with high voltages to decrease the current by high frequency current chopping. The number of steps per revolution of the motor can be set with dip switches on the controller. The current setting is 50800 step/revolution.

Controlling the motor requires three basic inputs to the controller. The first input is the step input. The motor will step on the trailing edge of each incoming pulse up to a rate of 1 MHz. The pulse width is set in DMC-1010 software to 1920 NS. The second input directs motor rotation. In this test, voltage is taken low corresponding to the counterclockwise (CCW) rotation. The third input to the controller is an OPTP input which requires + 5 VDC to operate the optical isolation feature. These three inputs are controlled and provided by DMC-1010.

The specimen test set includes the worm-gear assembly, the specimen mounting stage, the specimen platforms, the clip-on displacement gages and the load cell. The platforms are moved inward or outward by the worm-gear and the treaded screw. The screw and the platforms are mounted on the stage. The specimen is 30 mm square and 1 to 3 mm thick with two 3-mm diameter holes drilled about 14 mm apart to fit over the loading pins which are screwed into the platforms (see Figures 3-2 and 3-3).

The Clip-On Displacement (COD) Gage is a product of MTS Systems Corporation (MTS model 632.03B-30). It is designed to sense crack opening displacements and is typically used to monitor crack growth in a specimen during fracture mechanics testing. It uses precision resistance-type strain gages bonded to a metallic element to form a whetstone bridge circuit. The calibration of COD is 0.007131 in./mV, or 0.18 mm/mV, on a 4 mm scale. The excitation voltage is 5.99 V.

The Load Cell (LC) is a product of Sensotec, Inc., part no. 11/2335-07 and serial no. 353700. The LC's full-scale capacity is 1000 lbs under tension. The calibration factor is 2.4602 mV/V. Because the excitation is 5.0 V, the calibration is $2.4602 \text{ mV/V} \times 5.0 \text{ V} = 12.3 \text{ V}$ for 1000 lbs, or 81.3 lbs/mV.

The amplifiers are transducer conditioning amplifiers manufactured by the Ectron Corporation. The two Model 563 FN amplifiers are included in the Model E513-20 Enclosure. They are wide band, true differential DC instrumentation amplifiers with built-in transducer signal conditioning

functions. The output of the basic amplifier is ± 10 V at 10 mA. The maximum gain is 1 K. The amplifiers used in this test were for COD and LC signal amplifying and for the supply of excitation power.

The filter is a Krohn-Hite Model 3988 Butterworth/Bessel dual channel filter. It provides a tunable frequency range from 0.03 Hz to 1 MHz in low-pass mode and 0.03 Hz to 300 kHz in high-pass mode. Each channel of the 3988 is an 8-pole, wide range, low-pass/high-pass filter or an amplifier providing gains to 70 dB in 0.1 dB steps. The 3988 will accept input signals of ± 10 V peak at 0 dB gain and has selectable ac or dc coupling. The two channels of the filter are used for COD and LC signals in this test.

System Noise and Noise Solving

Noise is the main problem in this micro-displacement test. The noise in the system is more distinguishable than the useful signals. Three kinds of noise were found to exist using an oscilloscope and FFT equipment to analyze the system noise.

One type of noise was caused by the discrimination of the Galil Controller. The lowest limit for the ADC of DMC-1010 is 0.488 mV; therefore, the sampling signals should be much higher. This problem can be effectively eliminated by amplifying the useful signals before they are sampled by the ADC. Considering the highest limit (± 10 V) of the ADC, the gain for the displacement signals was set to 500 and the gain for load signals to 1000. Thereafter, the useful signals were in the range of voltage and the ADC noise was suppressed.

The second kind of noise was caused by electricity. The sources of this noise-causing electricity included the computer, the step-motor, the motor controller, and the power supply source. By using FFT equipment, two powerful noise signals were found. One signal was around 60 Hz and the other was around 1.5 kHz. They were tested when the step motor was turned off.

When the step motor was on, the third kind of noise appeared. The strongest AC noise signal was 12.5 Hz with a magnitude of 0.076 mV. Another AC noise signal was around 1 Hz, or 0.016 mV. These noise signals were tested without amplifying. They were probably mechanical noise.

An attempt was made to eliminate the noise by shielding the step-motor controller bar and covering the motor set and line with tin foil. The best results were obtained after using a low-pass filter. The filter was set for a low-pass filter of 0.5 Hz and for DC signals. Although a lower frequency noise signal exists with a maximum of 0.02 mV, 0.5 Hz is still an ideal cutoff frequency because any lower filter cutoff frequency causes the system response to delay severely in open-loop and closed-loop control tests.

Open-Loop Control

In the open-loop control test, specimens were made using both glass-plastic materials and aluminum ceramic material. Because the glass-plastic specimens are easier to make, they were used in the first period of test. In the test, the step motor was set to rotate at 3500 counts per second. At that rotation rate, the specimen was dragged by a speed of 0.002 mm/sec, which is 0.0112 mV/s to the COD correspondingly. The sampling period was decided by the characteristics of glass-plastic and the limitation of the DMC-1010.

The glass-plastic had a relatively large strain. The size of the specimen was $30 \times 30 \times 2.5$ mm. It was made in the same way as the ceramic specimen was made. It would not break until the total strain was above 0.25 mm. The DMC-1010 supplied an array for a total of 1600 elements. Therefore, if the COD signals and LC signals were sampled simultaneously, a maximum of 800 data samples could be collected for each. To record the data of all the periods of a test, 1 second was chosen as the sampling period. The load-displacement graph is shown in Figure 3-4. The alumina ceramic material was more brittle than the glass-plastic material. When the specimens measured 30×30 mm with a thickness of 0.9~1.96, they sustained a strain amount of about 0.04~0.06 mm in a range of 0.2208~0.3324 mV of COD.

Several step motor speeds were chosen for the tests. One speed was designated to be 500 counts/second. Thus the specimens were loaded at a constant load-point displacement of $0.43 \mu\text{m}$ per second, corresponding to 0.0024 mV/s of COD. Another speed was set at 1000 counts/sec, or 0.0048 mV/s. The load-displacement graphs are shown in Figures 3-5 and 3-6. From the load-displacement curve, it can be observed that the higher the step motor speed, the more linear the curve. This feature occurred because the stiffness of the test system was not hard enough, especially the two pins which held the specimens. Since the speed of the test is still relatively high, it is difficult to obtain an ideal characteristic curve of load-displacement for alumina ceramic material.

Closed-Loop Control

The principle of closed-loop control is shown in Figure 3-1. The output signals were obtained from the COD and LC, and then the error signals were fed back into the system. Because the rotating speed of the step-motor was constant in the test, the distance between two sample points was chosen for reference. On this basis, the average velocity between every two sample points was assumed to be the same. If there was any difference, the error was fed back into the step-motor to increase or decrease the rotation speed of the motor. For the glass-plastic specimens, when the motor rotated at a speed of 3500 c/s, the change of COD was 0.0112 mV/s as mentioned before. Because the noise was about 0.02 mV, the sample period was set to be 2.5 seconds. Thus the displacement changes were 0.028 mV for COD in each sampling interval. Then the range to be

controlled was from $0.028 - 0.01$ mV to $0.028 + 0.01$ mV. Figure 3-7 shows the load-displacement curve used in this control range. Compared with the results from the open-loop test, the maximum tension and maximum strain displacement are almost the same; however, the curve from the closed-loop control system is much more linear.

Difficulties arise when using the existing test equipment to perform closed-loop control tests on ceramic samples. As analyzed previously, the maximum strain of ceramic is about $0.04\text{--}0.06$ mm, or $0.2208\text{--}0.3324$ of COD, but the noise signal is 0.02 mV. Therefore, the noise signal overwhelms the useful signal in micro-displacement movement.

Conclusion

The system is suitable to perform open-loop tests for the micro-displacement test. The noise in the system is still a significant problem. It may be caused by the mechanical equipment. The test system has difficulty performing more precise testing, especially closed-loop control tests.

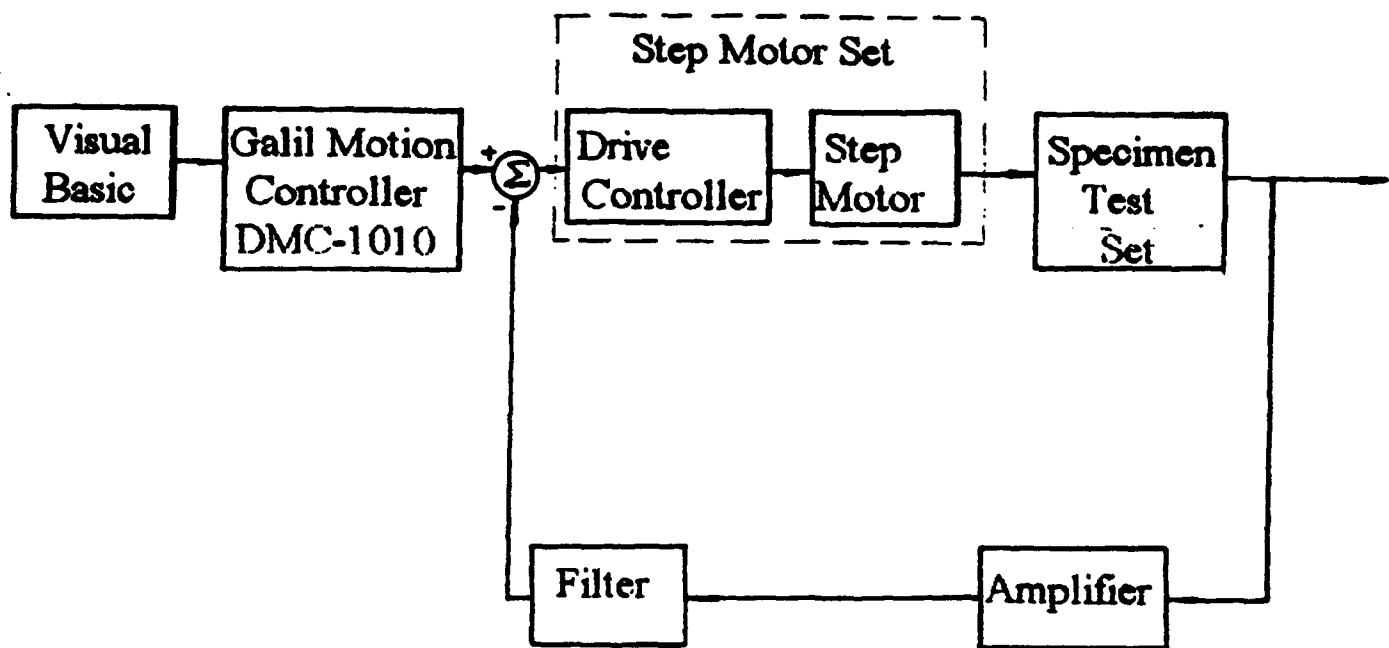
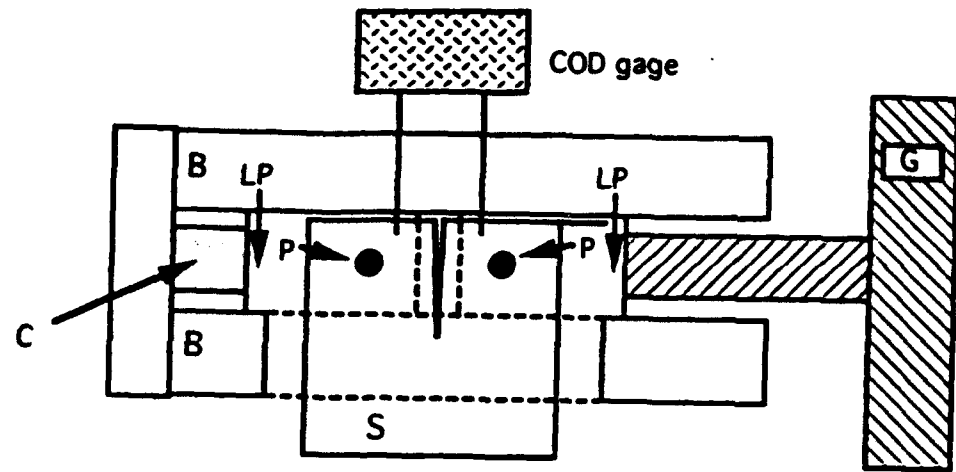


Figure 3-1. System Block Diagram



S - Specimen
 G - Worm Gear
 P - Loading pins
 C - Load cell
 LP - Loading platforms
 B - Base of loading stage

Figure 3-2. Specimen Test Set

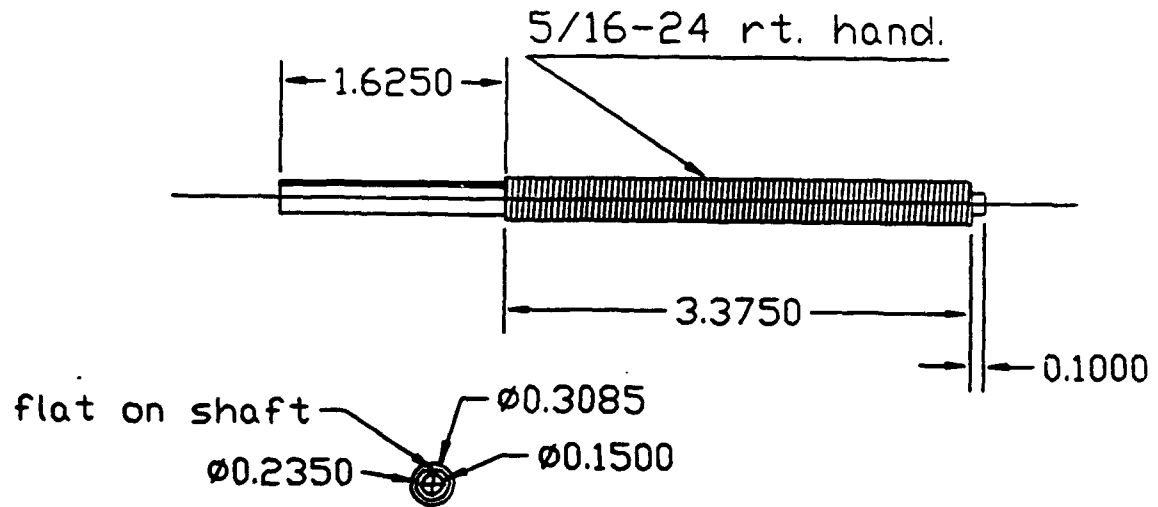


Figure 3-3. Thread Screw Bar

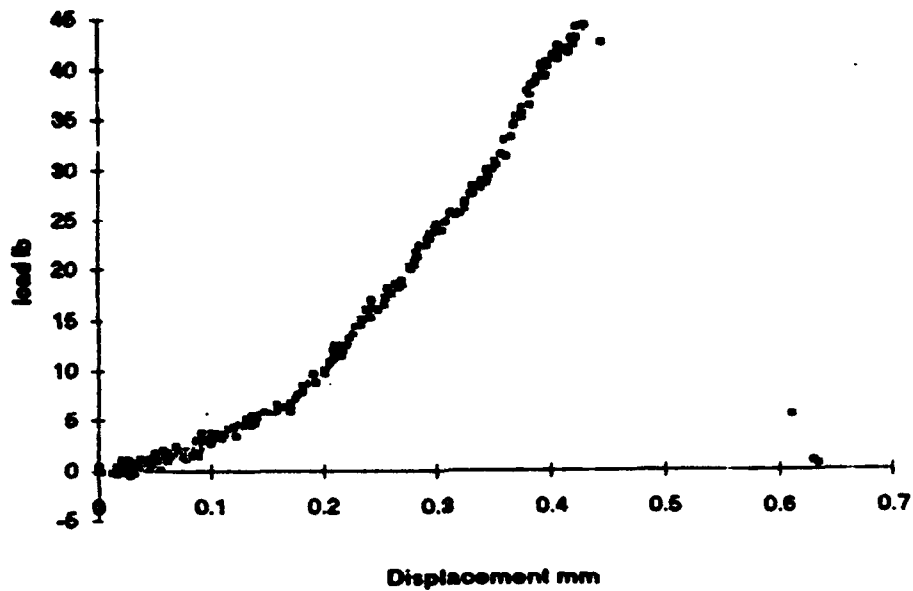


Figure 3-4. Open-Loop Control
Load-Displacement Graph for Glass-Plastic Specimen
Motor rotation speed 3500 counts/second
Sampling period 1 second, LPF 0.5 Hz

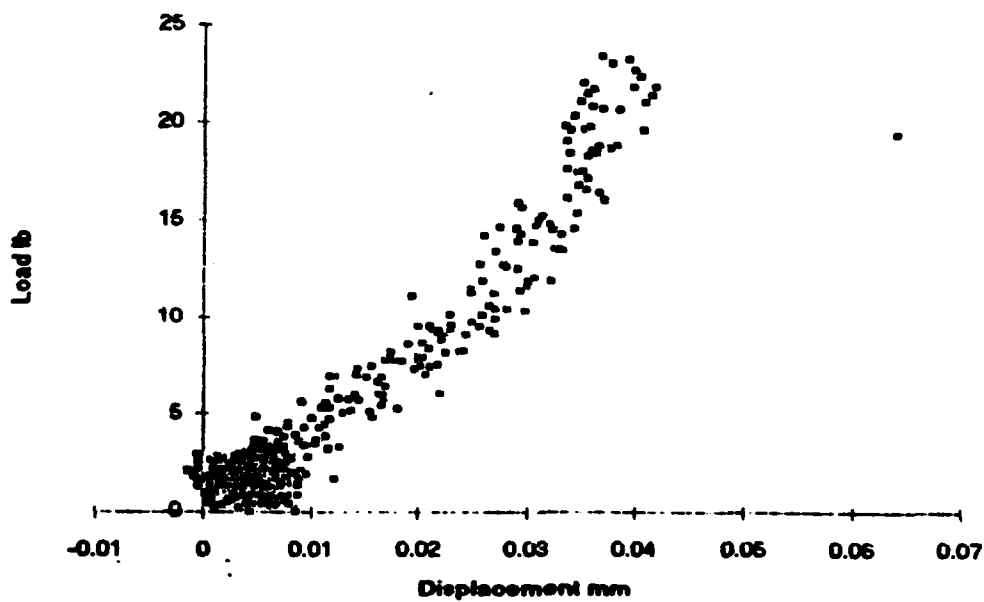


Figure 3-5. Open-Loop Control
Load-Displacement for Alumina Ceramic Specimen
Motor rotation speed 500 counts/second

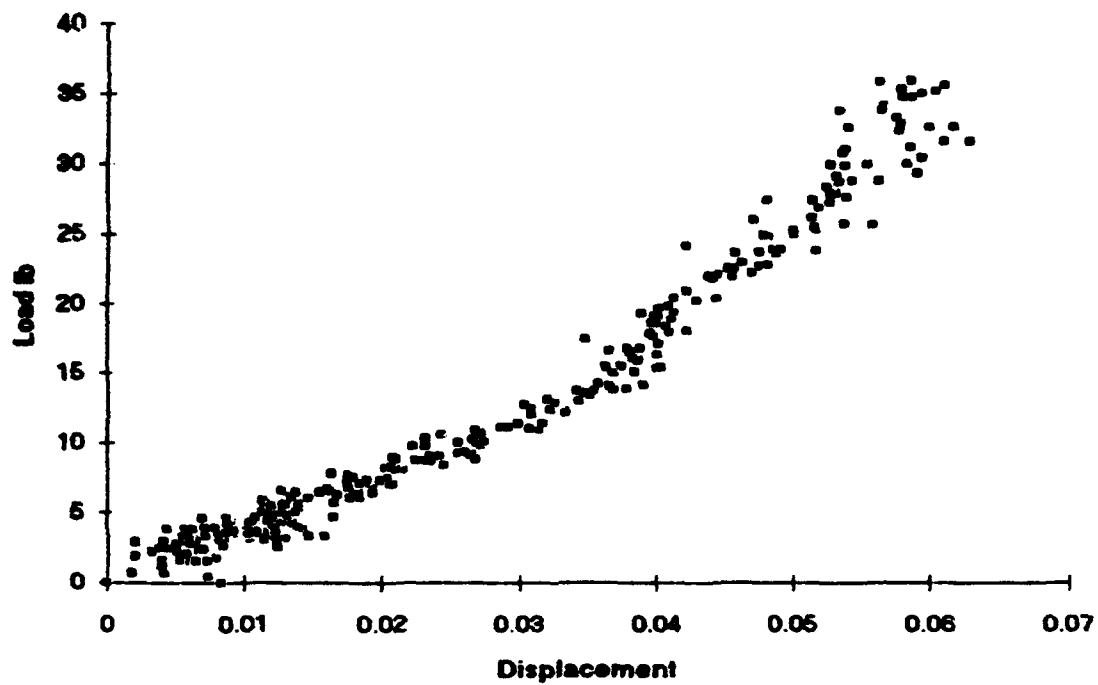


Figure 3-6. Open-Loop Control
Load-Displacement for Alumina Ceramic Specimen
Motor rotation speed 1000 counts/second
Sampling period 1 seconds, LPF 0.5 Hz
Sample thickness 1.98 mm

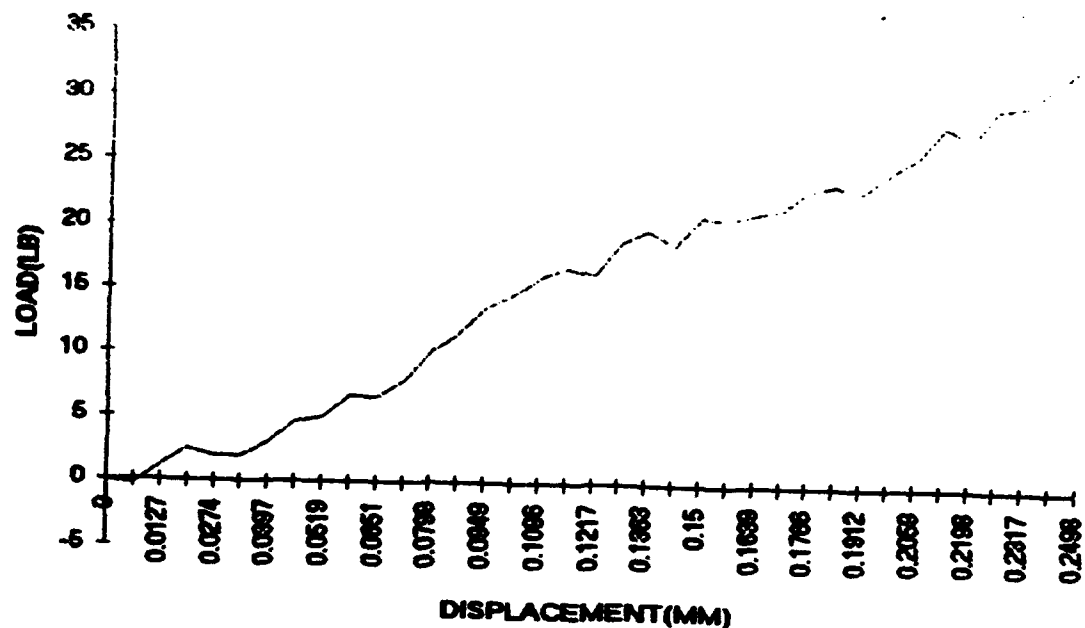


Figure 3-7. Close-Loop Control
Load-Displacement Graph for Glass-Plastic Specimen

Product Specification

Timothy J. Ross and Ming L. Wang, University of New Mexico

"FSEM: FAST SCANNING ELECTRON MICROSCOPY"

U.S. Pat. No. 5,254,857 Oct. 1993

Why High-Speed SEM?

Transmission, reflection and scanning electron microscopes offer spatial resolution superior to that of light microscopes. Transmission and reflection electron microscopes also provide temporal resolution of ~20 ns/frame, rivaling the temporal resolution of light microscopes. SEM, however, is the only type of electron microscope which offers both high spatial resolution and large depth of focus surface imaging, even for rough surfaces, of particular value for surface studies of material responses to dynamic loads at high magnifications, for example. Based on experiments with the high-imaging speed (FSEM: Fast SEM) now under development at the University of New Mexico (UNM) under a collaboration with industry, we expect that state-of-the-art components will soon permit SEM dynamic microscopy at 0.1 μm spatial resolution and 2 $\mu\text{s}/\text{frame}$ at 64 pixels X 64 pixels per frame, with acceptable signal-to-noise ratios in final images.

Problems of High-Imaging Speed SEM

To obtain high-imaging speed operation in the SEM, four task areas must be addressed: illumination, detection, deflection and recording. The specimen must be illuminated with an electron beam of sufficient intensity to provide a detectable signal of sufficient quality to provide a good image of the specimen. And, such an image must be obtained at framing speeds of interest with scan beam deflection providing suitable speed and proper deflection waveform, without degrading scan beam quality. The fourth task is to record the imaging signal synchronously with the scan for later playback in a "movie" format. To address these four problems and to illustrate the FSEM technology, we modified an SX-40A SEM manufactured by International Scientific Instruments, Inc. The unmodified SEM had a tungsten hairpin cathode electron gun, two stages of condenser optics, two-stage magnetic deflection and an objective lens.

Illumination and Detection

Illumination and detection are intimately related. If the detector detects all imaging radiation produced by the scan beam without introducing noise or frequency errors, further image quality improvements can only be had by increasing illumination. Though our detector is not this perfect, we believe its deficiencies have far less impact on image quality than those of the illumination system we have at present. In any case, illumination ultimately determines obtainable image quality. In the case of secondary electron imaging, for example, and typical scan beam (primary electron) energies, one secondary electron is produced for every 1-10 primary electrons. Clearly, improving primary beam current can dramatically improve image quality.

Deflection

The other major problem area we have encountered in obtaining high-imaging speed SEM operation is in deflection of the scan beam at high rates with minimal distortion of the desired deflection waveform (non-linearity) or degradation of scan beam quality (deflection aberrations). Several improvements to scan generator/scan coil driver electronics were performed. Problems due to the quiescent state of the scan generator producing a constant DC input to the scan coil drivers between scans, resulting in image shift and unnecessary power dissipation in the scan coil drivers and scan coil termination resistors have been resolved. Lower magnification was required to properly center specimens in the microscope field of view for dynamic imaging, but the lower magnification requires higher deflection currents causing significant heating in the scan coil termination resistors. These problems were also resolved. Another modification which makes the microscope easier to use is a switch box permitting simple switching between analog data acquisition and digital data acquisition. The specimen is first positioned in the microscope field of view in analog mode, then switched to digital mode to take a digital movie.

Recording

The imaging signal output is input to a digital data acquisition system, which consists of a fast digitizer, a digitizer controller (via GPIB bus), fast memory modules and a chassis containing appropriate power supplies. The digitizer we are using at present is the LeCroy 8828D, capable of a 200 MHz digitizing rate, 8-bit measurement and 1 Mbyte of fast memory storage (expandable to 2 Mbyte). At 256 pixels X 256 pixels per frame this allows for storage of 16 frames of data. At 128 X 128 pixels per frame, 64 frames of data may be stored. The digitizer also provides a clock pulse used to generate scan deflection signals so that data-taking and scanning are synchronized.

Project Status

In the last year we have obtained images at a 25 MHz pixel rate, which translates, for 256 pixels X 128 pixels per frame, to 381 frames per second. This is ~10 times TV-rate (nominally 30-50 Hz), the maximum framing rate available in any commercial SEM. Further, to our knowledge, 25 MHz pixel rate is ~2-3 times faster than anyone else has obtained for secondary electron or any other sort of SEM imaging. We have developed a design which will allow us to obtain images at the 200 MHz pixel rate specification of our digital data acquisition system and at higher rates using a faster digital data acquisition system. A 200 MHz pixel rate translates to a 12.2 kHz framing rate at 128 pixels X 128 pixels per frame. A 2 GHz pixel rate (state-of-the-art in 8-bit, long record length digitizers) results in a 488-kHz framing rate at 64 pixels X 64 pixels. Our images have acceptable signal-to-noise ratios, i.e. $S/N > 6$.

We have obtained images at a 381 Hz framing rate, a beam voltage of 10 kV and magnification of $> 1,000X$. We believe, however, that we are at the limit of the image quality that can be obtained with the electron source we have at present, and at the stated operating parameters. Some brightness improvement is possible by choosing different operating parameters. However, by using high brightness cathodes, which may be 2-3 orders of magnitude brighter than the source we have at present, we believe that image quality may be greatly improved. We have also obtained time-integrated photographs taken at various horizontal line times to examine high-speed linearity and aberrations of the deflection coils, as well as the time resolution of the high-speed secondary electron detector. If we assume 128 pixels per horizontal line, a horizontal line time of 7.5 μ s represents a time resolution of 60 ns. Also assuming 128 vertical pixels per frame, the corresponding framing rate would then be ~ 1 kHz. Table 1 shows the relationship of effective framing rates for various horizontal line times.

Table 1

Effective Framing Rates for Various Horizontal Line Times

<u>horizontal line width</u>	<u>hor. lines/frame</u>	<u>time/frame</u>	<u>framing rate</u>
10 μ s	256	2.56 ms	391 Hz
	128	1.28 ms	781 Hz
5 μ s	256	1.28 ms	781 Hz
	128	640 μ s	1.56 kHz
2 μ s	256	512 μ s	1.95 kHz
	128	256 μ s	3.91 kHz
1 μ s	256	256 μ s	3.91 kHz
	128	128 μ s	7.8 kHz
0.5 μ s	256	128 μ s	7.8 kHz
	128	64 μ s	15.6 kHz

Dynamic Specimen Loading for FSEM

With the FSEM capabilities discussed above, a variety of dynamic microscopic studies become possible. Chief among these is microstructural response of structural materials to transient loads, such as mechanical, thermal and magnetic loads. We have developed a magnetically-induced stress wave (MISW) device for producing mechanical loads in specimens. This device has fractured DSP concrete cement in dynamic tension loading. The pressure pulse-width of this device is $\sim 1 \mu$ s, with pressure pulse peaks of $\geq 10,000$ psi. This magnetically-induced stress wave concept using ~ 1 mm radius rod specimens allows for various combinations of dynamic loading--single- or double-ended, compression or tension--and does permit fracture to be localized within the SEM field of view and to time fracture with scanning. However, these advantages can only be realized for specimen materials which are homogeneous (on the scale of the pressure pulse length) and (i) can transmit a $\sim 1 \mu$ s wide pressure pulse without dissipation, (ii) are weak enough to break at pressure peaks in the 3,000-30,000 psi range (the present limits of our device extrapolated to the 35 kV maximum capacitor charge voltage) and (iii) exhibit crack nucleation and growth and macroscopic fracture within $\sim 1 \mu$ s. The FSEM imaging is synchronized with the initiation of fracture in the specimen.

Summary of Progress

During the research effort, the concept of using a high-speed scanning electron microscope (SEM) to observe real-time microstructural response of dynamically loaded structural materials was verified experimentally at a maximum framing rate of 381 Hz (256 horizontal pixels X 128 vertical pixels), about an order of magnitude higher than previously possible with conventional SEM's. This experimental accomplishment proved the soundness of several key concepts:

- That a tungsten hairpin cathode is bright enough to obtain useful digital images at the framing rate listed above,
- That a secondary electron detector can be built and operated at high enough count rates to obtain such images,
- That the scan coil assembly standard on an ISI SX-40A SEM can be replaced to allow imaging at such rates with spatial resolution approaching 100 nm,
- That signal acquisition and scan generation can be synchronized to obtain a succession of well-defined frames in a "movie" format at pixel rates far in excess of conventional TV-rate SEM video bandwidths (Table 2 lists the events for which we have made movies), and
- That a magnetically-induced stress wave device can be used to obtain dynamic fracture within the SEM chamber and field of view, with scanning timed to coincide with fracture.

Based on the progress made during this research effort and the promise that the FSEM device has for the new area of dynamic microscopy a patent has been filed on the technology.

Table 2

Dynamic Events Imaged

- Glass beads excited by piezoelectric transducer
- Thorne fiber excited by piezoelectric transducer
- Fuse rupture under excess current pulse
- Rosin fracture under shock loading
- Concrete fracture under tensile load
- Watch gear moving periodically

Potential Applications of the FSEM

Table 3 shows the technology areas that we have reviewed over the last 2 years that could benefit from the utility of our FSEM device. Certain modifications, such as thermal stages or a gaseous environment, to the stages would be necessary, but the FSEM technology could be readily adapted to these situations.

Table 3

Potential Applications of FSEM

- monolayer studies (Langmuir-Blodgett)--may require ESEM
- recrystallization of silicon films and semiconductors
- real-time dynamic fracture
- *In situ* SEM- or microprobe-observed fracture
- TEM video microscopy (TV-rate)
- solid phase transitions (see high T_c superconductor listings below)
- atomic motion within crystals
- Pulsed electron microscopy--non-scanned (~25 ns/frame)
- TEM studies of laser-pulse-induced processes
- reflection electron microscope surface studies
- High T_c superconductor studies
- phase transitions during fabrication--SEM
- flux creep, magnetic contrast imaging--SEM
- flux creep, decoration imaging--SEM
- Domain growth/transition of polymers
- Integrated circuit inspection and metrology
- E-beam testing of integrated circuits (strobed voltage contrast in SEM)
- E-beam specimen damage reduction

**DIRECT APPLICATION OF CONSTRAINTS
TO SYMMETRIC ALGEBRAIC SYSTEMS**

H. L. Schreyer¹ and D. A. Parsons²

December, 1993

ABSTRACT

Constraints arise naturally in the context of rigid inclusions, incompressibility, inextensible fibers and deformed finite elements. Typical methods for handling constraints in the governing matrix equation include Lagrange multipliers, penalty weights, and elimination of variables. Each has a particular undesirable feature. Proposed here is a procedure in which each constraint is handled directly and sequentially through a modification of the rows and columns of the governing matrix and force vector. Positive definiteness, symmetry and the dimensions of the matrix remain unchanged. Elementary examples involving both the static and dynamic response of a bar are given to illustrate the procedure.

Key Words: constraints, rigid inclusions, incompressibility, dynamic response

^{1,2}Professor and Graduate Student, respectively, Department of Mechanical Engineering, The University of New Mexico, Albuquerque, NM 87131.

INTRODUCTION

There are numerous engineering situations in which constraints are a natural part of the system. Examples are rigid inclusions, incompressibility, inextensible fibers, floors in plane frames, boundary conditions, and mesh distortion. The usual methods for handling constraints require either a modification to the dimension of the algebraic problem, or good numerical intuition. On the other hand, the implementation of a one-point constraint is often done directly by merely adjusting rows and columns so that the original dimension and symmetry of the matrix remain unchanged. A corresponding procedure for a multipoint constraint of arbitrary dimension is not generally available, at least in most textbooks on the finite element method. Here, such an algorithm is given with simple examples for static and dynamic problems.

If multipoint constraints are given explicitly, conventional methods for handling the constraints are the Lagrange multiplier technique, the penalty method, and partitioning of variables with the subsequent need for adjustments to the governing matrix (Barlow, 1982; Cook et al., 1989). The Lagrange-multiplier method requires the development of an augmented matrix which means the problem must be redimensioned. The penalty method involves an adroit choice of a parameter to provide a balance between ill conditioning and loss of accuracy. Partitioning of variables requires a considerable amount of manipulation and the inverse of a submatrix which can be of a significant size if there are a large number of constraints.

Sometimes governing systems become ill-conditioned as a parameter describing a material property, the dimension of a body, or element distortion approaches a critical value. Various techniques involving under integration with hourglass control, other modifications to the element stiffness matrix, and remeshing are often used to prevent the ill conditioning. For many cases, these techniques can be interpreted as approximate methods for applying a constraint which should be applied based on fundamental mathematical arguments.

Webb (1990) uses a projection operator to elegantly derive a rather general algorithm for handling constraints without modifying the structure or the symmetry of the governing matrix. However, nothing is said about how the projection is generated. Hueck and Schreyer (1993) provide an explicit method for constructing the projection matrices. The result is a general method for exactly handling multipoint constraints without altering the number of algebraic equations. As an example, the incompressibility constraint is invoked for the quadrilateral element with plane-strain elasticity. With this approach, the problem normally associated with the usual method of letting Poisson's ratio approach 0.5 is avoided. Also, severe mesh distortion is not a significant factor. Although the application to a beam problem provides good results, the projection method suffers from the fact that a matrix as large as the original one and the inverse of a smaller matrix have to be obtained. Therefore, the potential usefulness of the approach for large-scale problems is limited.

To maintain the advantage of the direct application of multipoint constraints, an algorithm is proposed that is closely related to one given by Abel and Shephard (1979), a contribution which has not received the attention it deserves. The attractive features of the method presented here include the fact that the symmetry and the dimension of the governing matrix is maintained, there is no reordering of variables, and with some care, any number of constraints can be applied sequentially with the one algorithm. A complete description of the procedure is given together with static and dynamic examples.

BASIC EQUATIONS

Suppose the objective is to solve for x the algebraic equation

$$Ax = b \quad (1)$$

in which the symmetric matrix A is $n \times n$ and b is given. The system is restricted by the constraint

$$c^T x = d \quad (2)$$

An alternative way of viewing the problem is to define the residual

$$r = Ax - b \quad (3)$$

Consider a weighting vector w . Frequently the governing equation (1) is obtained from the requirement that

$$w^T r = 0 \quad (4)$$

for arbitrary w . Whenever a component of x is prescribed, the corresponding component of w must be zero. Similarly, if the constraint (2) exists, then w is not arbitrary but must satisfy the corresponding constraint

$$c^T w = 0 \quad (5)$$

The formulation given by (4) and (5) is the one that provides insight into how the matrix A should be modified so as to maintain symmetry. If A is not initially symmetric, then the modified matrix is also not symmetric.

For convenience, let $\{A_i\}$ and $\langle A_i \rangle$ denote the i 'th column and row of A , respectively. Then an alternative form of (4) is

$$\sum_{i=1}^n w_i r_i = 0 \quad r_i = \langle A_i \rangle \{x\} - b_i \quad i = 1, \dots, n \quad (6)$$

The next section illustrates the algorithm for a three-point constraint to show that the approach is simply a generalization of a common algorithm used to handle the one-point constraint normally associated with boundary conditions. Then the general algorithm is given.

THREE-POINT CONSTRAINT

For ease of presentation, the constraint is applied to the first three components of x but the algorithm can be applied equally well to any other combination of components.

Suppose the constraint is

$$c_1 x_1 + c_2 x_2 + c_3 x_3 = d \quad (7)$$

The constraint on w is

$$c_1 w_1 + c_2 w_2 + c_3 w_3 = 0 \quad (8)$$

which implies that w_1 , w_2 and w_3 are not arbitrary. Set $w_3 = -c_1 w_1/c_3 - c_2 w_2/c_3$. The result is that each of the first two equations is really a linear combination of the original equation and the third equation. Since w_3 has been eliminated, the constraint equation is used for the third equation. At this stage, the governing set of algebraic equations is:

$$A^* x = b^* \quad (9)$$

in which

$$A^* = \begin{bmatrix} a_{11} - \frac{c_1}{c_3} a_{31} & a_{12} - \frac{c_1}{c_3} a_{32} & a_{13} - \frac{c_1}{c_3} a_{33} & a_{14} - \frac{c_1}{c_3} a_{34} & \dots \\ a_{21} - \frac{c_2}{c_3} a_{31} & a_{22} - \frac{c_2}{c_3} a_{32} & a_{23} - \frac{c_2}{c_3} a_{33} & a_{24} - \frac{c_2}{c_3} a_{34} & \dots \\ c_1 & c_2 & c_3 & 0 & \dots \\ a_{41} & a_{42} & a_{43} & a_{44} & \dots \\ \dots & \dots & \dots & \dots & \dots \end{bmatrix} \quad (10)$$

$$b^* = \begin{bmatrix} b_1 - \frac{c_1}{c_3} b_3 \\ b_2 - \frac{c_2}{c_3} b_3 \\ d \\ b_4 \\ \dots \end{bmatrix} \quad (11)$$

Now suppose the constraint is used to replace x_3 in every equation but the third. Then the governing matrix and force vector become:

$$A^{**} = \begin{bmatrix} a_{11}^* - \frac{c_1}{c_3} a_{13}^* & a_{12}^* - \frac{c_1}{c_3} a_{13}^* & 0 & a_{14} - \frac{c_1}{c_3} a_{34} & \dots \\ a_{21}^* - \frac{c_2}{c_3} a_{23}^* & a_{22}^* - \frac{c_2}{c_3} a_{23}^* & 0 & a_{24} - \frac{c_2}{c_3} a_{34} & \dots \\ c_1 & c_2 & c_3 & 0 & \dots \\ a_{41} - \frac{c_1}{c_3} a_{43} & a_{42} - \frac{c_2}{c_3} a_{43} & 0 & a_{44} & \dots \\ \dots & \dots & \dots & \dots & \dots \end{bmatrix} \quad (12)$$

$$b^{**} = \begin{bmatrix} b_1^* - \frac{d}{c_3} a_{13}^* \\ b_2^* - \frac{d}{c_3} a_{23}^* \\ d \\ b_4 - \frac{d}{c_3} a_{43} \\ \dots \end{bmatrix} \quad (13)$$

in which a_{ij}^* and b_i^* denote the components of A^* and b^* , respectively. The only components not symmetric involve the indices (1, 2), (1, 3) and (2, 3). Suppose the third equation is multiplied by c_1/c_3 and the result added to the first equation. Then the third component in the first row of A^{**} is c_1 . Similarly, multiply the

third equation by c_2/c_3 and add the result to the second equation to obtain c_2 as the third component in the second row of A^{**} . Now the governing matrices are

$$A^{**} = \begin{bmatrix} a_{11} - \frac{c_1}{c_3} a_{13} + \frac{(c_1)^2}{c_3} & a_{12} - \frac{c_2}{c_3} a_{13} + \frac{c_1 c_2}{c_3} & c_1 & a_{14} - \frac{c_1}{c_3} a_{34} & \dots \\ a_{21} - \frac{c_1}{c_3} a_{23} + \frac{c_1 c_2}{c_3} & a_{22} - \frac{c_2}{c_3} a_{23} + \frac{(c_2)^2}{c_3} & c_2 & a_{24} - \frac{c_2}{c_3} a_{34} & \dots \\ c_1 & c_2 & c_3 & 0 & \dots \\ a_{41} - \frac{c_1}{c_3} a_{43} & a_{42} - \frac{c_2}{c_3} a_{43} & 0 & a_{44} & \dots \\ \dots & \dots & \dots & \dots & \dots \end{bmatrix} \quad (14)$$

$$b^{**} = \begin{bmatrix} b_1 - \frac{d}{c_3} a_{13} + \frac{c_1 d}{c_3} \\ b_2 - \frac{d}{c_3} a_{23} + \frac{c_2 d}{c_3} \\ d \\ b_4 - \frac{d}{c_3} a_{43} \\ \dots \end{bmatrix} \quad (15)$$

It can be shown by direct substitution that the (1, 2) and (2, 1) components of the modified matrix are equal so the resulting system is symmetric. The solution to

$$A^{**}x = b^{**} \quad (16)$$

automatically satisfies the three-point constraint equation.

GENERAL ALGORITHM FOR MULTIPONT CONSTRAINTS

The results for the special case given above suggests the following approach to handle a general multipoint constraint. The format is chosen to suggest the form that a subroutine might take for invoking a given constraint. Let S_c be the set of indices associated with the constraint. Then the constraint is given by

$$\sum_{i \in S_c} c_i x_i = d \quad (17)$$

in which the summation is taken over all indices in the constrained set. Each c_i is nonzero. Choose arbitrarily a particular element of S_c , $i = I$ say, with x_I labelled the constraint variable (or master variable). One might wish to choose I so that c_I is the one with the maximum absolute value of all c_i 's in the set. Let S_c^* be the set S_c with element I excluded, i.e., S_c^* is the set of indices associated with the slave variables.

For ease of interpretation in the three-point constraint case, different symbols were used at each step for the modified matrices and vectors (e.g., A^* , b^* , etc.). However, there is no need to actually define new matrices and vectors so in the following algorithm only one matrix and vector pair are used.

The data required for a subroutine based on this algorithm are c_i , d , S_c . The first task is to select I and S_c^* . Then the steps given in the following box are performed.

For each i contained in S^* perform operations 1 through 5:

1. Replace the row $\{A_i\}$ in A with $\{A_i\} - \frac{c_i}{c_l} \{A_l\}$.
2. Similarly replace b_i with $b_i - \frac{c_i}{c_l} (b_l - d)$.
3. In the existing vector, b , replace $\{b\}$ with $\{b\} - \frac{d}{c_l} \{A_l\}$.
4. In the existing matrix, A , replace the column $\{A_i\}$ with $\{A_i\} - \frac{c_i}{c_l} \{A_l\}$.
5. Set $A_{il} = c_i$, $A_{li} = c_i$, $A_{ll} = c_l$ and $b_l = d$. Place zeros in the remaining entries of column l and row l of A .

For each i and j contained in S^* perform the following operation:

6. Replace the component A_{ij} with $A_{ij} + \frac{c_i c_j}{c_l}$.

The result is a symmetric system whose solution automatically satisfies the multipoint constraint.

MULTIPLE CONSTRAINTS

If several constraints exist but the constraints contain variables that are not common, then the constraints can be applied sequentially with no modifications to the proposed algorithm.

Frequently it is necessary to apply multiple constraints with one or more variables common to more than one constraint. With the proposed approach it is possible to erase a previous constraint if special precautions are not taken. One method to circumvent the problem is to scan all constraints to see if, for each constraint, a variable can be defined which does not appear in subsequent constraints. Then the procedure can be applied sequentially with no modifications.

If it proves to be impossible to identify a unique constraint variable for a given constraint, then an alternative approach must be used. When this situation arises, the constraint variables must be eliminated sequentially using previous constraint equations until a variable appears that has not been previously designated a constraint variable. Then the algorithm can be applied as given.

SIMPLE EXAMPLE

Consider a governing matrix and a force vector that typically result from the use of two-node elements in one dimension:

$$[A] = \begin{bmatrix} 1 & -1 & 0 & 0 & 0 & 0 \\ -1 & 2 & -1 & 0 & 0 & 0 \\ 0 & -1 & 2 & -1 & 0 & 0 \\ 0 & 0 & -1 & 2 & -1 & 0 \\ 0 & 0 & 0 & -1 & 2 & -1 \\ 0 & 0 & 0 & 0 & -1 & 1 \end{bmatrix} \quad \{b\} = \begin{bmatrix} 1 \\ 0 \\ 0 \\ 0 \\ 0 \\ 1 \end{bmatrix} \quad (18)$$

Suppose the following two constraints are applied:

$$x_1 = 0 \quad x_6 - x_5 + x_4 - x_3 = 1 \quad (19)$$

The resulting matrix, force vector and solution vector are:

$$[A] = \begin{bmatrix} 1 & 0 & 0 & 0 & 0 & 0 \\ 0 & 2 & -1 & 0 & 0 & 0 \\ 0 & -1 & 4 & -3 & 1 & -1 \\ 0 & 0 & -3 & 4 & -2 & 1 \\ 0 & 0 & -1 & -2 & 2 & -1 \\ 0 & 0 & -1 & 1 & -1 & 1 \end{bmatrix} \quad \{b\} = \begin{bmatrix} 0 \\ 0 \\ -1 \\ 1 \\ 0 \\ 1 \end{bmatrix} \quad \{x\} = \begin{bmatrix} 0 \\ 1 \\ 2 \\ 2.5 \\ 3.5 \\ 4 \end{bmatrix} \quad (20)$$

Note that the governing matrix remains symmetric, although the band width is larger, and the solution vector satisfies the constraints.

ONE-DIMENSIONAL WAVE PROPAGATION

Formulation

The dynamic equation of motion for a bar of unit cross-sectional area is

$$\rho a + f^* = Eu_{xx} \quad a = u_{tt} \quad (21)$$

in which x and t are the spatial and temporal independent variables, respectively, the dependent variable u denotes the displacement, E is Young's modulus, which is assumed to be constant, and ρ the mass density. The wave speed is $c = \sqrt{E/\rho}$. The force per unit length is f^* . For an element of length h , the element stiffness and mass matrices for a two-node element are:

$$[K] = \frac{E}{h} \begin{bmatrix} 1 & -1 \\ -1 & 1 \end{bmatrix} \quad [M] = \frac{\rho h}{6} \begin{bmatrix} 2 & 1 \\ 1 & 2 \end{bmatrix} \quad (22)$$

The global mass and stiffness matrices are assembled in the usual manner to obtain the spatially discretized version of (21) as follows:

$$Ma + Ku = f \quad (23)$$

in which M and K denote the system mass and stiffness matrices, respectively, and f the system force vector. Suppose (23) is discretized in time:

$$Ma^n + Ku^n = f^n \quad (24)$$

in which u^n and a^n denote approximations to u and a , respectively, at the time $t^n = ns$, $n = 0, 1, 2, \dots$ for a time step of s . Consider a general trapezoidal rule:

$$v^{n+1} = v^n + s[\alpha_1 a^{n+1} + (1-\alpha_1) a^n] \quad (25a)$$

$$u^{n+1} = u^n + s[\alpha_2 v^{n+1} + (1-\alpha_2) v^n] \quad (25b)$$

in which α_1 and α_2 are two free parameters chosen to obtain specific integrators. When (24) and (25) are combined, the resulting system integrator for updating the velocity vector is

$$Av^{n+1} = r^n \quad (26)$$

in which

$$A = M + \alpha_1 \alpha_2 s^2 K \quad (27a)$$

$$r^n = Bv^n - sKu^n + \alpha_1 s f^{n+1} + (1-\alpha_1) s f^n \quad (27b)$$

$$B = M - \alpha_1 (1-\alpha_2) s^2 K \quad (27c)$$

The updated displacement is obtained with the use of (25b). The algorithm is implicit. It is unconditionally stable if the integration parameters satisfy the constraints $\alpha_1 = \alpha_2 \geq 0.5$. There is no numerical dissipation if $\alpha_1 + \alpha_2 = 1$. An explicit integrator is obtained by summing rows of $[A]$ to obtain a diagonal matrix.

Suppose constraints on u are converted to constraints on v . Then the multipoint constraint algorithm need only be applied to the matrix $[A]$ prior to an LU decomposition, and the implicit integrator is applied in the usual manner.

Static Problem

Consider a bar of length $L = 1.28$ fixed at the left end, $x = 0$. At the right end, suppose a force of magnitude one is applied. Also suppose that the third quarter of the bar, $0.5 \leq x \leq 0.75$, is rigid. If the bar is discretized with 64 uniform elements, then the rigid zone requires 16 constraint equations, namely, the displacements of the nodes of each element in the rigid zone are equal. For $E = 1$, the solution for displacement and stress in the bar with and without the inclusion is shown in Figs. 1a and 1b, respectively. As expected, the strain and consequently the stress in the rigid inclusion is predicted to be zero although the stress cannot be zero if equilibrium is to be satisfied.

Dynamic Problem

Now consider the bar to be free at the left end and the unit force at the right end is applied instantaneously at $t = 0$. The solution is a step wave which propagates from the right end to the left at the wave velocity of $c = 1$ for $\rho = 1$

and $E = 1$. Solutions are shown in Fig. 2 for $\alpha_1 = \alpha_2 = 0.5$ for various configurations and $s = 0.5h/c$ where h denotes the length of the element.

Figure 2a gives the numerical solution at a time of $L/2c$ for the displacement and velocity for 128 elements with no rigid inclusion. Displayed are typical dispersive features such as overshoot and oscillations which are characteristic of the numerical algorithm and are nonphysical. A simple way to handle an inclusion is to use an artificially high stiffness. Figure 2b shows the solution for the same mesh and wave speed but with a Young's modulus of $E^* = 1024$ used to simulate a rigid inclusion identical to that used for the static problem. Figure 2c shows the solution to the same rigid inclusion problem but with a time step of $s = 0.5h/c^*$ where c^* is the wave speed based on E^* . This small time step is more typical of those required with an explicit integrator and represents a severe limitation of the use of an artificial stiffness.

Corresponding solutions obtained with the use of the constraint algorithm are given in Figs. 3a, 3b, and 3c for 64, 128 and 512 elements, respectively. When the wave transits one-quarter of the bar and impinges on the rigid segment, motion is immediately realized at the other end of the inclusion. Therefore, at a time of $L/2c$ the wave has actually travelled three-quarters of the bar rather than one-half the length which is the distance travelled for a bar with no inclusion. For all cases, the velocity and displacement constraint over the inclusion is shown. Some of the oscillations are reduced with refinement of the mesh and time step.

A small amount of dissipation can be used to remove spurious oscillations. Results are given in Fig. 4 for $\alpha_1 = \alpha_2 = 0.52$, 128 elements and $s = 0.5h/c$. Note that the wave shapes are considerably cleaner for both the homogeneous bar (Fig. 4a) and the bar with a rigid inclusion (Fig. 4b).

EFFECT ON CONDITION NUMBER

For a constraint equation, if the largest coefficient in absolute value is set equal to one, then the constraint vector has been scaled so that the infinity norm is one. For large problems it may be desirable to scale the constraint vectors to minimize the condition number as defined by the ratio of maximum to minimum eigenvalues. For model static problems such as that whose solution is shown in Fig. 1, all constraints were scaled by a factor η . The condition number was then determined for various values of η for a wide range in the number of elements and in the size of a rigid inclusion. Generally speaking, a scale factor of $0.5/h$ for a uniform mesh provided nearly optimal condition numbers for a large number of cases. However, it is not obvious what the scale factors should be for a set of arbitrary constraints without actually performing numerical investigations.

CONCLUSIONS

A simple algorithm for handling one or more multipoint constraints has been presented. The dimension of the governing matrix is retained as is symmetry and positive definiteness when these properties are present. The change in band width is dictated only by the span of degrees of freedom in each constraint equation. The application to both static and dynamic problems is straightforward and should prove to be a useful computational technique for the numerous engineering problems in which constraints are important.

ACKNOWLEDGMENT

Partial support for this research from the Air Force Office of Scientific Research under Grant AFOSR-91-0419 to the University of New Mexico is gratefully acknowledged.

APPENDIX. REFERENCES

Abel, J., and Shephard, M.S. (1979). "An algorithm for multipoint constraints in finite element analysis," *Int. J. Num. Meth. Engrg.*, Vol. 14, No. 3, 464-467.

Barlow, J. (1982). "Constraint relationships in linear and nonlinear finite element analysis," *Int. J. for Num. Methods in Engineering*, Vol. 18, 521-533.

Cook, R.D., Malkus, D.S., and Plesha, M.E. (1989). *Concepts and Applications of Finite Element Analysis*, J. Wiley and Sons, New York, Third edition.

Hueck, U., and Schreyer, H.L. (1992). "The use of orthogonal projections to handle constraints with applications to incompressible four-node quadrilateral elements," *Int. J. for Num. Methods in Eng.*, Vol. 35, 1633-1661.

Webb, J.P. (1990). "Imposing linear constraints in finite-element analysis," *Commun. Appl. Num. Methods*, Vol. 6, 471-475.

LIST OF FIGURES

1. Static solution for displacement and stress in a bar:
 - (a) without a rigid inclusion,
 - (b) with a rigid inclusion.
2. Plots of displacement and velocity as a function of x at time $t = 0.5L/c$:
 - (a) no inclusion ($s = 0.5h/c$),
 - (b) the simulation of the inclusion using an artificially large E and a "large" time step of $s = 0.5h/c$,
 - (c) the simulation of the inclusion using an artificially large E and a "small" time step of $s = 0.5h/c^*$.
3. Plots of displacement and velocity as a function of x at time $t = 0.5L/c$ obtained with the constraint algorithm ($s = 0.5h/c$):
 - (a) 32 elements,
 - (b) 128 elements,
 - (c) 256 elements.
4. Plots of displacement and velocity as a function of x at time $t = 0.5L/c$ obtained with a small amount of numerical damping (128 elements and $s = 0.5h/c$):
 - (a) no inclusion,
 - (b) constraint algorithm with a rigid inclusion.

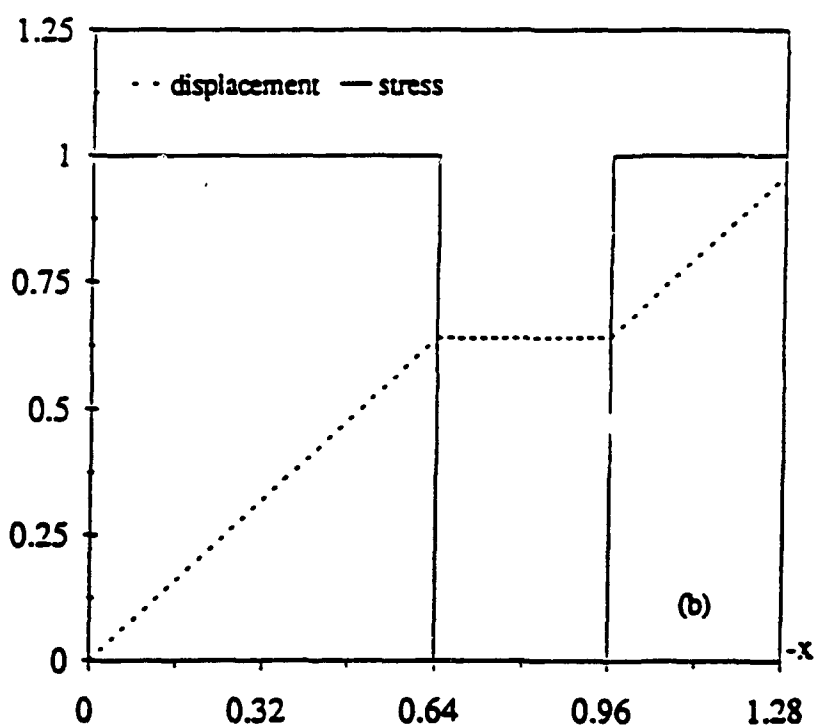
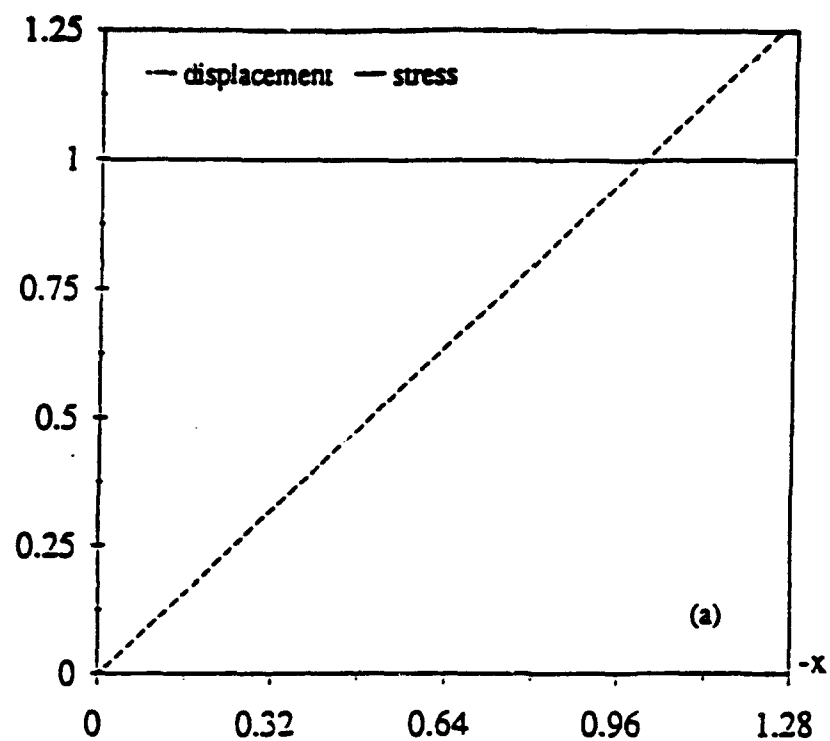


Figure 1a 1b

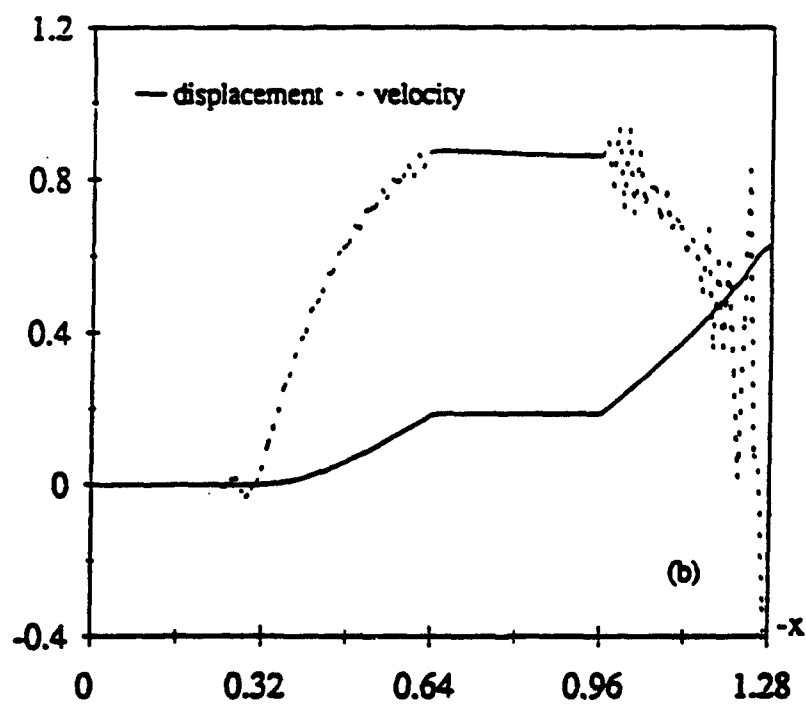
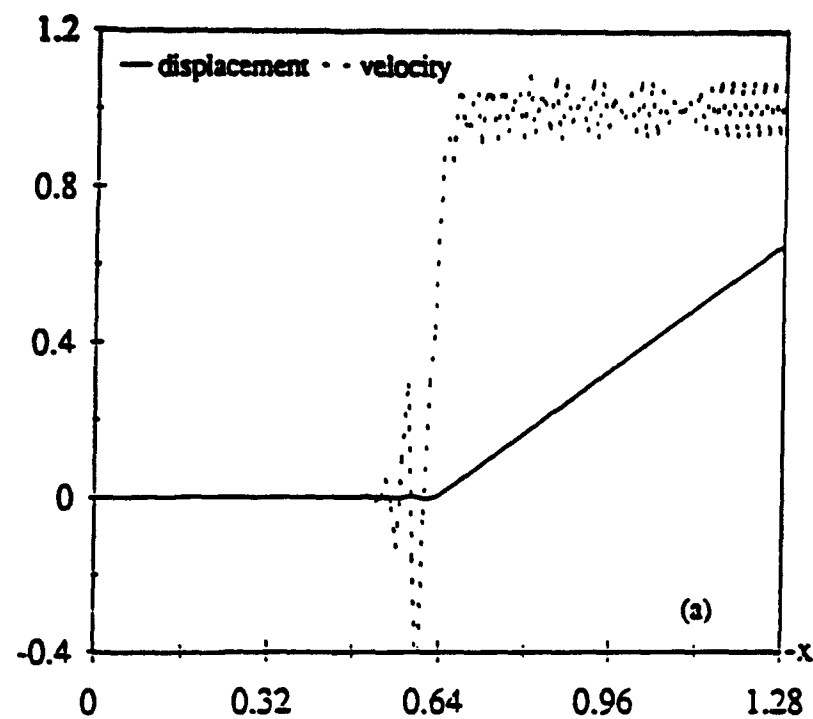


Figure 2a 2b

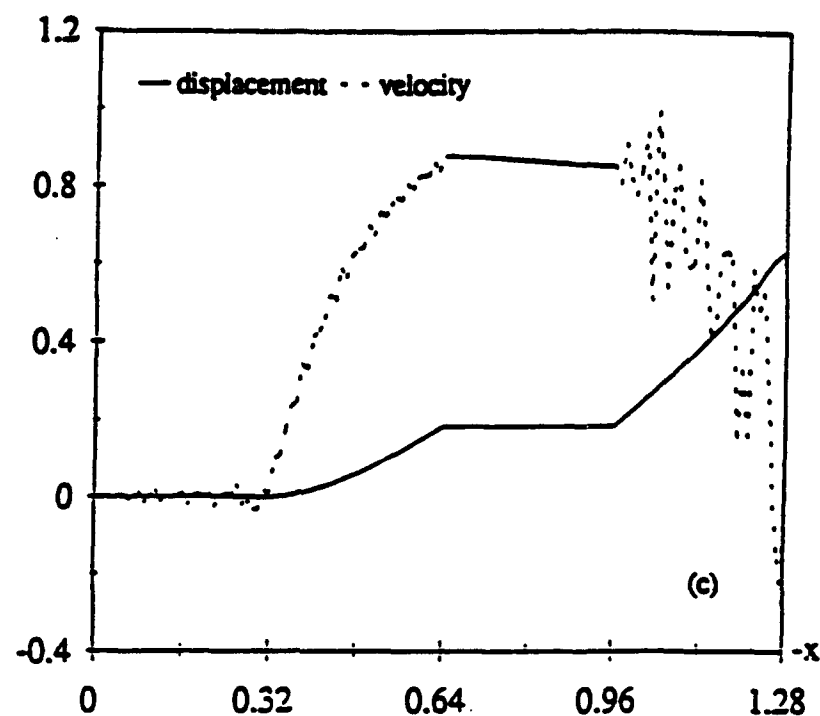
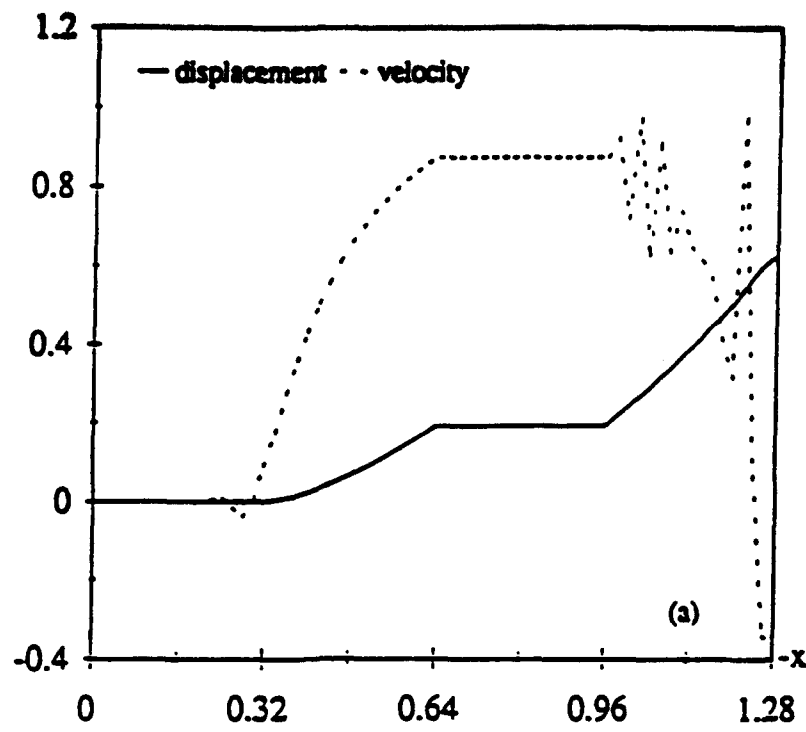
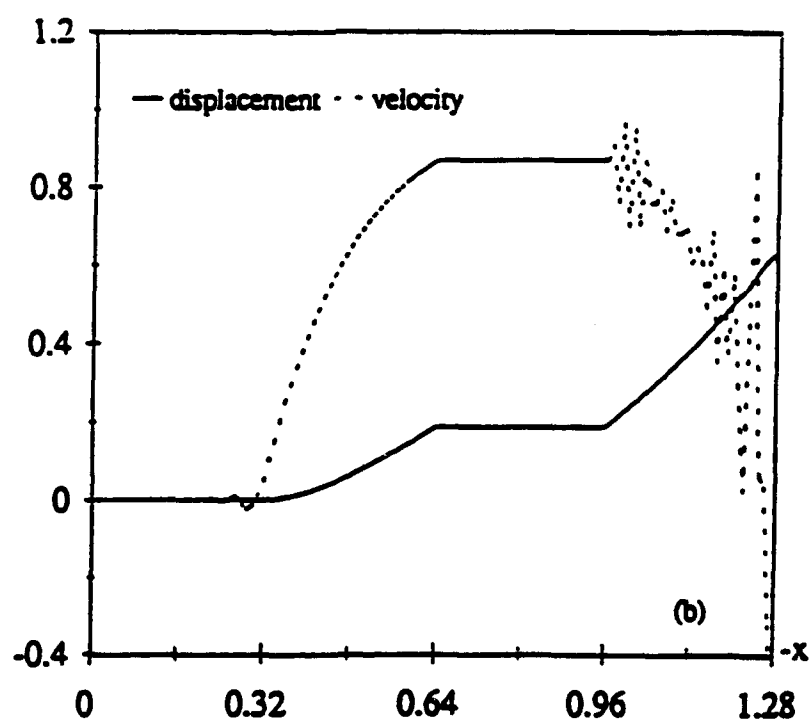


Figure 2c



(a)



(b)

Figure 3a 3b

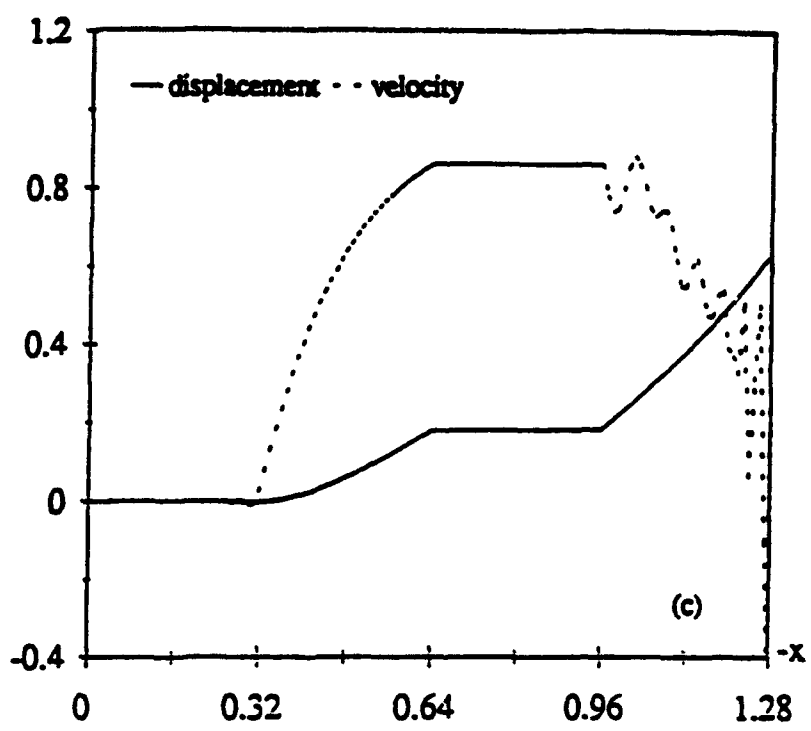


Figure 3c

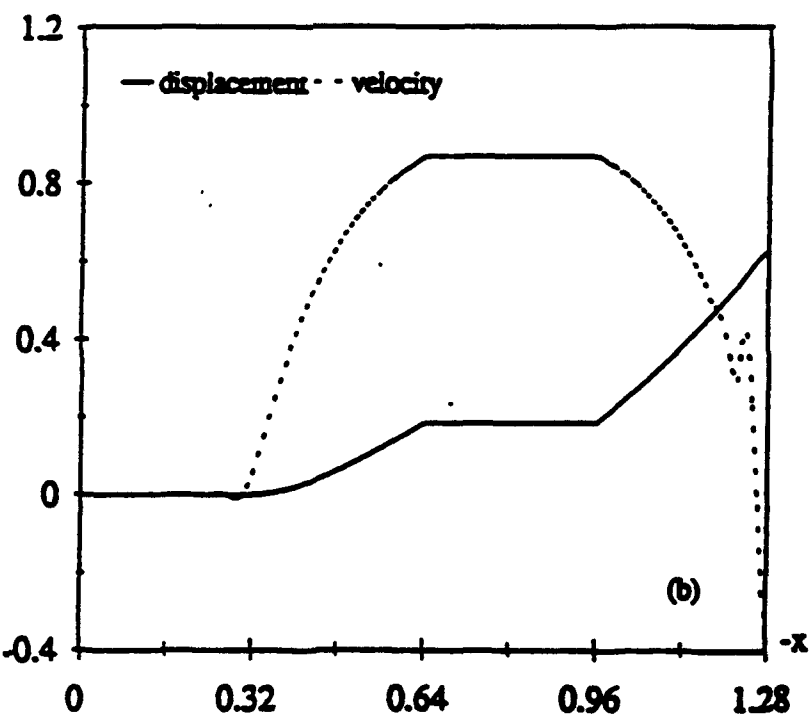
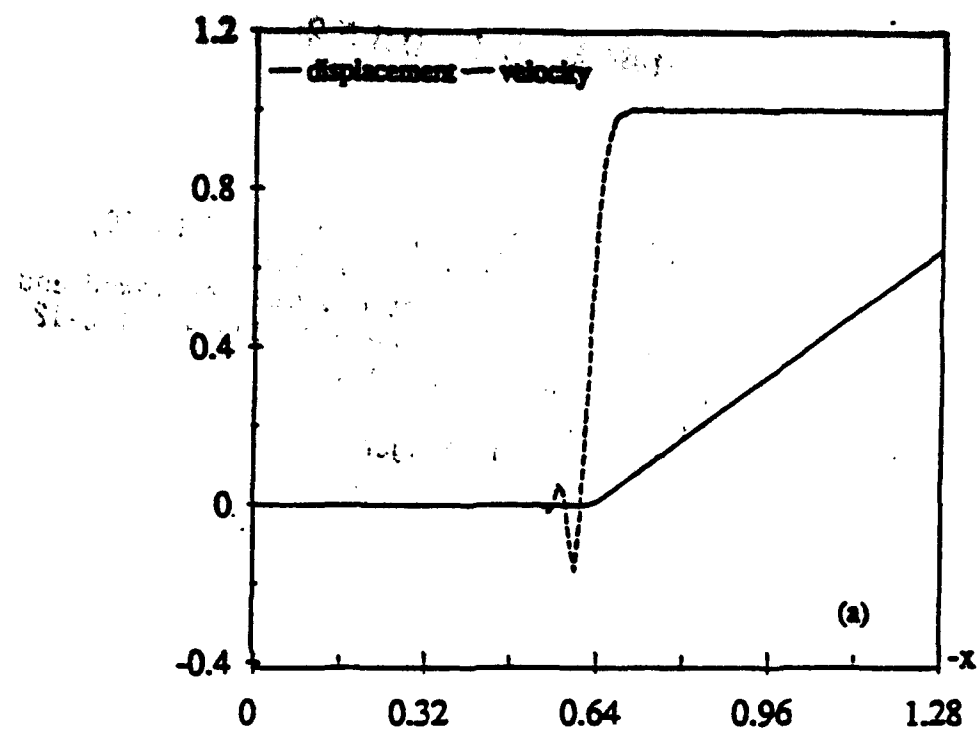


Figure 4a 4b